UNIVERSIDAD DE GRANADA

Tesis doctoral

Marzo 2011

CHEF polar basis for astronomical data analysis

[PhD THESIS]

Yolanda Jiménez Teja

Instituto de Astrofísica de Andalucía (CSIC)

Memoria de Tesis

presentada en la Universidad de Granada

para optar al grado de Doctora en Física

Director de tesis:

Narciso Benítez Lozano

A todos los que estuvieron a mi lado.

- Hay muchas maneras de dividir a los seres humanos - le dijo.
Yo los divido entre los que se arrugan para arriba y los que se arrugan para abajo,
y quiero pertenecer a los primeros.

- en *Mujeres de ojos grandes*, Ángeles Mastretta -

Agradecimientos

Dicen que lo más complicado de escribir en una tesis es la introducción, quizás las conclusiones. En mi caso, no lo más difícil, sino lo más laborioso, serán sin duda los agradecimientos. Y es que a lo largo de estos años han sido tantos los que me han ayudado de una forma u otra, que resulta harto complicado expresar en apenas unos párrafos todo lo que les debo.

Por supuesto debo comenzar hablando de mi familia, mis padres y mi hermano, que en todo momento me animaron a apostar por una tesis que supieron entender como mi meta más anhelada. Tanto en mis comienzos en Cádiz como en mi posterior traslado a Granada, siempre comprendieron cuánto necesitaba conseguirlo y jamás me cuestionaron. Estas primeras palabras de agradecimiento también quiero compartirlas, cómo no, con Txitxo, mi director, que me dio una oportunidad cuando nadie más lo hizo. Gracias por confiar en mí y gracias por haberme concedido toda esa libertad que necesitaba para hacer esta tesis, jamás anteponiendo sus ideas a las mías.

A lo largo de esta andadura he tenido la grandísima suerte de toparme con otros maravillosos profesionales que me dedicaron no sólo su preciado tiempo, sino también sus conocimientos. Es el caso por ejemplo de Renato Álvarez, Sarah Bridle, Holland Ford, Marc Postman o Joel Bergé, aunque a buen seguro me dejo a muchos más en el tintero.

En el terreno de lo personal la lista es prácticamente interminable. Comenzando por aquellos compañeros de "este nuestro garito" que siempre estuvieron a mi lado, Eva y Alberto. Eva me enseñó no sólo a dar mis primeros pasitos en esto de la investigación sino que me mostró lo que es una verdadera amiga, comprometida y valiente a pesar de tener mucho que perder, más que nadie. Y Alberto, esa fuente inagotable de buen talante, que siempre me arrancó carcajadas hasta en los momentos más tensos y que siempre me apoyó en la "lucha", incluso en mis incursiones más arriesgadas. Y de mi grupo de Cádiz cómo no mencionar a Maria José, esa excelentísima mujer, no sólo como matemática sino también como persona. Tú has sido de las que más me ha enseñado y me has hecho ver las cosas más claras; mi próximo objetivo en la vida es ser la mitad de lo que eres tú.

En mi camino en Granada sois tantas las personas excepcionales que me he cruzado que, si bien Cádiz siempre será mi tierra, habéis conseguido que sienta ésta como mi casa. Comenzaré por el principio, con mis niñas, que me integraron aquí y me ayudaron con la Astrofísica. Mi Crisiña, con esa risa contagiosa y esa dulzura, que tanto cariño y buenos consejos me dio. Mi Bego, la felicidad y el optimismo hechos persona, con la que tantísimos ratos compartí dentro y fuera del IAA. Jamás olvidaré cómo la mitad de tus frases empezaban por "¡tengo una teoría!" y la otra mitad terminaban con "infinito". Ni, por supuesto, cómo por muy malo que fuese el bache, siempre acabábamos arreglando el mundo con una copa de vino en la mano y un millón de risas. Y mi Susi, con su forma despreocupada

y risueña de ver las cosas, con las que tantas confidencias compartí camino de flamenco. Y eso me lleva a recordar a mi Chúa, por supuesto, que siempre con su taconeo, su energía y su fuerza me hacía desconectar del mundo y darme cuenta de lo feliz que se puede ser bailando... ¡y de lo paciente que puede ser alguien como para conseguir que yo fuese capaz de taconear así!

En este momento creo que toca dar un gracias inmenso a la persona más importante de todo mi camino en Granada, Toño, que siempre me ha animado en lo bueno y en lo malo, me ha hecho a crecer como persona, me ha enseñado probablemente más que nadie en la vida, me ha hecho reir, me ha dado un cariño inmenso y, sobre todo, me ha dado ganas de superarme cada día.

Quiero recordar también a todos aquellos con los que he compartido muchos buenos momentos, como el entrañable Miguelito al que siempre deberé muchas risas en el café y un sinfín de canciones; mi queridísimo 547, con esa Gabi serena, juiciosa y razonable que tanto me ha soportado (y aportado) sobre todo al final de este trabajo, esa Tere y ese Darío haciéndonos reir con sus ocurrencias, ese Vicent que siempre me trató mejor que a una reina (y me ayudó hasta el último día en la entrega de la tesis) y esa Domi, tan dulce y siempre dispuesta a ayudar. Y, por supuesto, también quiero mencionar a mi querido equipo de voley, mi verdadera via de escape a la tensión sin la que no hubiese sobrevivido.

Es obligado dedicar un párrafo especial también a mis Maris, que me han acompañado día tras día en esta recta final, y me han sufrido con una paciencia infinita. A Julia le debo una infinidad de consejos, una comprensión y una paz que me ha transmitido como nadie. A Clarita, que me haya dado fuerzas inagotables, razones para sonreir en todo momento y que me sienta tan orgullosa de mí misma como lo estoy hoy. Y a Alicia, la capacidad de hacerme desconectar de todo e incluso conseguir que me hagan gracia sus chistes malos. Pero, sobre todo, niñas, gracias por ese cariño y esa lealtad infinita que me habéis demostrado. Muy pocos pueden presumir de amigas como vosotras.

Y finalmente quería agradecer a todos aquellos que en el último momento de este final de infarto que ha tenido la tesis me han ayudado de forma práctica, transmitiéndome ánimo, trayéndome regalitos, ech‡ndome una mano con la escritura (¡ese Charly!), ayudándome con el papeleo (debo hacer mención especial aquí a Vicent, Fran, Domi, Darío y Gabi, que todos pusieron su granito de arena ese último día), haciéndome de comer o incluso dándome masajes. No olvidaré esos detalles jamás, chicos.

A todos os pertenece un trocito de este preciosísimo trabajo que he realizado. Sin vosotros, no existiría.

Resumen

Los éxitos de la Cosmología Observacional en los últimos años han sido espectaculares: tras décadas de esfuerzos infructuosos por fin disponemos de medidas razonablemente precisas y fiables de los parámetros cosmológicos clásicos, como la constante de Hubble, la densidad total de materia y la densidad total del Universo. Como es usual en estos casos, estos descubrimientos han conducido a nuevos enigmas, como la necesidad de incluir los conceptos de materia y energía oscura para poder explicar estos nuevos datos.

Son numerosos los nuevos cartografiados que se están planeando para un futuro próximo con el único propósito de recoger más datos y de mejor calidad. Este es el caso de los surveys propuestos para los próximos años, como por ejemplo, Pan-STARRS, DES, J-PAS o LSST, entre otros. La cantidad de datos que estos cartografiados proporcionarán es enorme: millones de imágenes de todo tipo de objetos astronómicos serán recogidas. Además, la calidad de estos datos se incrementa día a día gracias a los espectaculares avances tecnológicos que se producen actualmente en instrumentación: se construyen telescopios cada vez más grandes, así como cámaras e instrumentos ópticos cada vez más precisos.

Uno de los problemas clásicos es el modelado de la distribución de luz de las galaxias y otros objetos astronómicos. Esto es necesario para poder medir el flujo total, sus parámetros morfológicos y, en resumen, para poder cuantificar y clasificar la enorme variedad de estas "concentraciones de estrellas". Vemos las galaxias con cada vez mayor resolución en las observaciones y cada vez mayores áreas del cielo son cartografiadas. Este desarrollo debe estar acompañado de una correspondiente mejora en las técnicas de análisis, que deben ser adaptadas a las nuevas características de los datos. En este sentido, los métodos clásicos de modelado de galaxias solían emplear varias componentes formadas por perfiles analíticos para descomponer las imágenes, mientras que los algoritmos más modernos se han centrado en el uso de bases ortogonales, capaces de modelar los rasgos irregulares y detalles que las técnicas clásicas no podían procesar.

Cuando se inició esta tesis no existían herramientas analíticas para modelar galaxias suficientemente robustas, precisas y versátiles, y nuestro objetivo principal fue desarrollar una técnica con esas características. En este trabajo, un nuevo método ha sido desarrollado, la llamada base polar CHEF (de Chebyshev y Fourier, como veremos), que pertenece al segundo grupo de técnicas de modelado de galaxias. Es un método no-paramétrico, es decir, esta basado en funciones ortogonales, que han sido construidas de forma separable usando funciones racionales de Chebyshev para representar la coordenada radial y series de Fourier para expandir la componente angular. Las funciones racionales de Chebyshev se han mostrado altamente eficaces a la hora de procesar perfiles con fuertes pendientes, y la ortogonalidad de las bases las hace extraordinariamente flexibles, de tal forma que la precisión de los resultados obtenidos es excelente, como será mostrado. Tanto la base matemática teórica donde se

apoyan estas bases como la implementación práctica llevada a cabo, incluyendo los obstáculos y las dificultades que nos hemos encontrado por el camino y hemos tenido que solventar, son descritas de forma detallada en este trabajo. Además, se han llevado a cabo varios tests para demostrar la superioridad de las bases CHEF con respecto a otros algoritmos como GALFIT o las shapelets, así como estimaciones cuantitativas de este mejor comportamiento.

Esta herramienta ha demostrado su extraordinaria versatilidad en la práctica. En particular, se ha implementado la deconvolución de la PSF en el dominio de las CHEFs y se han calculado dos técnicas totalmente distintas para el cálculo de parámetros morfológicos usando sólo los coeficientes CHEF. Se ha aplicado de forma práctica toda esta teoría a datos reales del proyecto ALHAMBRA o del UDF, mostrando la velocidad y capacidad del algoritmo para trabajar de forma automática, y se ha probado a procesar con éxito cúmulos de galaxias substrayendo los objetos de la zona central para permitir el análisis y la medición de los arcos de lentes gravitacionales ocultos tras ellos. Finalmente, también se ha implentado una forma de estimar el shear del efecto lente gravitacional débil simplemente usando los coeficientes CHEF, así como un intento de medir la fotometría de los arcos previamente mencionados.

Aún quedan muchas posibilidades y nuevas aplicaciones de las CHEFs que explorar, tales como una esquema de caracterización morfológica de las galaxias aplicando un análisis de componentes principales a los coeficientes CHEF, la aplicación real de las bases a grandes cartografiados para elaborar catálogos fotométricos precisos o el desarrollo y mejora del algoritmo introduciendo funciones optimizadas, como precalcular una descomposición en valores singulares de las bases o la búsqueda de una relación analítica entre el radio de las galaxias y el parámetro de escala de las CHEFs.

Summary

Successes in Observational Cosmology during the last years have been spectacular: after decades of fruitless effort, rather precise and faithful measurements of the classic cosmological parameters are available, such as the Hubble constant, the total matter density or the Universe total density. As usual in these cases, these discoveries have led to new interrogations, as the necessity of including both the dark energy and the matter to explain these data.

Numerous surveys have been planned for the near future with the only purpose of collecting more data with a higher accuracy. This is the case of large surveys proposed for the next years, like Pan-STARRS, DES, J-PAS or LSST, among others. The amount of data these surveys will provide is huge: millions of images of all kind of astronomical objects will be stored. In addition, the quality of these data is increasing everyday due to the spectacular improvements in advanced instrumentation that we are currently seeing: larger and larger telescopes are being built, and more and more precise cameras and optical instruments are being designed.

One of the classical problems in this field is the modeling of the light distribution of galaxies and other astronomical objects. This is necessary to measure their total flux, their morphological parameters, and to put succinctly, to quantify and sort the enormous variety of these "concentrations of stars". Galaxies appear more and more resolved in observations, and larger areas in the sky are mapped. This development must be accompanied by a similar improvement in theoretical analysis techniques, adapted to the characteristics of new data. In this sense, the classical methods of galaxy modeling used to employ several components of analytical profiles to decompose data -which ensured the straightforward physical comprehension of the fitting parameters-, while the most modern ones are based on orthogonal bases, able to model the irregular and fine features which the classical techniques cannot deal with.

When this thesis was started, there were no analytical tools which were robust, accurate and versatile enough, and our main goal was developing one with such characteristics. In this work, a new method has been developed, the so called CHEF polar bases, which belong to second group of techniques for galaxy modeling. It is a non-parametric method, that is, based on orthogonal functions, separately built using Chebyshev rational functions to represent the radial coordinate and Fourier series to expand the angular component. Chebyshev rational functions are proved to be highly efficient in modeling decaying profiles, and the orthogonality of the bases makes them extraordinarily flexible, so the accuracy of the obtained models is excellent, as it will be shown. Both the theoretical mathematical background where these bases rely on and the practical implementation carried out, including the hurdles we have found in the way, are described in detail in this work. In addition, several tests have been also performed, in order to check the superiority of these bases against other algorithms as GALFIT or the shapelets, and quantitative estimations of this better behaviour are stated.

This tool has shown its versatility in practice. In particular, the deconvolution of the PSF in the images has been performed in the CHEF domain, and the calculation of morphological parameters just using the CHEF coefficients has been implemented with two radically different approaches. The application of all this theory on real data coming from large surveys as ALHAMBRA and the UDF has been also carried out, showing the speed and reliability of the algorithm working automatically, and the processing of cluster of galaxies subtracting the central objects to allow the analysis and measurement of strong lensing arcs has been successfully tried too. Finally, the shear estimation for weak lensing studies was also implemented just using the CHEF coefficients, as well as an attempt to measure the photometry of the arcs in strong lensing.

There are still plenty of possibilities and new applications of CHEFs to be explored, such as the morphological characterization of the galaxies by means of a principal component analysis of the CHEF coefficients, the real application of the bases to large surveys to create accurate photometric catalogues or the improvement of the pipeline introducing optimized mathematical algorithms, as a pre-calculated singular value decomposition of the basis functions or the search for an analytical relation between the half light radius of the galaxies and the scale parameter of the CHEFs.

Index

1

Introduction

Major advances in many science fields over the past century have arisen from the spectacular and dramatic instrumental development reached. This is particularly remarkable in the case of Astronomy, where more and more accurate and sophisticated telescopes have provided researchers with information from further objects in the deep sky and data displaying a level of resolution ever imagined. However, this advanced instrumentation -not only in imaging but also spectroscopic and polarimetric- has involved a more complexity in the data to analyze, making the usual techniques and algorithms inaccurate (fine features observed are not properly modeled) or even not practical (they cannot be efficiently applied to the huge amount of data coming, due to its own non-automated implementation). Because of that, instrumental development must be accompanied by improvement in algorithms, implemented in new techniques which are fast, precise and well-adapted to the new generation of datasets arriving.

1.1. Large astronomical surveys

The three-dimensional topology and distribution of the matter is one of the most powerful ways of testing cosmological theories, since the study of the layout of the galaxies and their clustering in the sky will report us information about the gravitational forces that led to the formation of these galaxies in the early Universe. This desire to map the universe in three dimensions has provided the main stimulus for the growth of one of the most successful industries in the history of modern astronomy: the surveying of galaxies, in particular, the redshift surveys. Aided by the rapid progress in information technology, current sky surveys are changing the way we view and study the Universe. Specially, large surveys are playing an increasingly central role.

The Sloan Digital Sky Survey (SDSS) (Margon, 1998) pioneered this trend, consisting on both a photometric and a spectroscopic survey. It is estimated it will finish obtaining multi-color images covering more than a quarter of the sky, with a final dataset of 230M celestial objects in an area of 8,400 square degrees, as well as spectra of 930,000 galaxies, 120,000 quasars, and 225,000 stars, over eight years of operations. Using a 2.5-meter telescope at Apache Point Observatory, New Mexico, a

new survey phase was released on 2008, and will continue through 2014.

The new generation of surveys is even more ambitious, and will generate astonishing data volumes. For example, the Panoramic Survey Telescope & Rapid Response System (Pan-STARRS) in Hawaii (Kaiser et al., 2002), composed by four individual optical systems of 1.8 meter diameter each, will be able to survey 6,000 deg^2 per night with a resolution of 0.3 arcsecond per pixel. Although the main concern of this survey is the detection of potentially hazardous objects in the solar system and the search for asteroids and variable objects, its exceptional ability to map large areas of the sky to great sensitivity makes it highly suitable to perform cosmology studies, such as galaxy clustering, gravitational lensing, formation of elliptical galaxies, studies of dwarf and low-surface-brightness galaxies and identification of far-infrared sources. With these purposes, it will catalog 99 % of the stars in the northern hemisphere and make an ultradeep survey of 1200 square degrees to $g = 27$.

The Dark Energy Survey (DES) (Abbott et al., 2005) will study the acceleration of the expanding universe by analyzing over 2,000 supernovae at redshift $0.3< z <0.8$, Baryon Acoustic Oscillations (BAOs), clusters at $0.1< z <1.3$, the shifting if the galaxy spatial angular power spectra with redshift, and the weak lensing effect to $z \sim 1$. The first two targets will provide a purely geometric constrain of the expansion of the Universe, whereas the latter will help us to measure both the expansion of the Universe and the growth of large-scale structures. So the final goal is measuring w with and accuracy of 5 %-15 % and w' with a precision of 30 %. Observations will be carried out by the Dark Energy Camera (DECam), which will be installed on the 4-meter telescope at the Cerro Tololo Inter-American Observatory in Chile by 2011. More than 300 million galaxies are expected to be detected covering an area of 5,000 deg^2 of the southern hemisphere in five bands.

Measuring Baryon Acoustic Oscillations with photometric redshifts is the main goal of Javalambre-PAU Astrophysical Survey (J-PAS) project (Benítez et al., 2009). For that, it is necessary to estimate the photometric redshifts with a precision of $\sigma_z \sim 0{,}003(1+z)$, what it is possible by means of the 40 filters especially design with this aim. Starting in 2013, this survey is expected to map 8,000 deg^2 in the sky, measuring photometric redshifts with $dz/(1+z) \sim 0{,}003$ and $dz/(1+z) \sim 0{,}01$ for respectively, 100M and 300M galaxies. With these numbers, it will be possible to determine w in the equation of state with an accuracy of 5 %.

The Large Synoptic Survey Telescope (LSST) (Ivezic et al., 2008) is the most ambitious survey ever planned in the visible band. Its main concerns can be summarized in four tasks: probing both the dark energy and matter, taking an inventory of the Solar System, exploring the transient optical sky, and mapping the Milky Way. Using a 6.5-meter telescope at Cerro Pachón in Chile, this project will be in charge of mapping 10,000 deg^2 in two bands plus 30,000 deg^2 more, which will be imaged multiple times with six optical filters. Being scheduled to start in 2015, the survey is expected to last 10 years, with a final dataset of about 10 billion galaxies, a number of objects which dwarfs all other projects.

To analyze and exploit such huge datasets, it is therefore necessary to develop techniques which are automated, objective and efficient. The techniques developed throughout the years have proved inadequate, either requiring too much interactivity from the user, what makes them impractical for large surveys processing, or inaccurate and unstable when working on automated mode. This will be more detailedly explained in the following section, what will show the necessity of developing a new method of image analysis.

1.2. Overview of existing methods of galaxy modeling

Many different techniques have been developed for image analysis in a wide variety of science fields, as Astronomy, Biology, Physics, Medicine, etc. In the particular case of Astrophysics, modeling shapes of astronomical objects is a task of fundamental importance with a large number of applications, as denoising, filtering, PSF deconvolution, extraction of significant features, detection of sources, object shape measurement, gravitational lensing, stellar formation, photometry, morphological classification or image simulations.

Throughout the history of image analysis in Observational Astronomy, methods to model sources have been always divided in two groups: techniques using analytical profiles, named parametric fitting, and techniques using orthonormal bases, called non-parametric fitting. Many works claim that parametric fitting by analytical functions is more suitable and useful since profiles are quite similar to the shape of the objects being modeled and, therefore, parameters of the decompositions provide a better insight about their meaning (Peng et al. (2002)) (they are usually the size, the axis ratio, the position, etc). Due to the search for orthogonality, the functions composing orthonormal bases do not look like the objects they are modeling, what is supposed to be a disadvantage because the coefficients interpretation becomes much more difficult. Nevertheless, although they are not so straightforward, this interpretation is still possible in many cases, as we will see in the case of the CHEF coefficients.

On the other hand, defenders of orthonormal methods state that their flexibility and reliability is much higher that of parametric fittings. Certainly, in the limit of infinite expansions, orthonormal bases are capable of fitting any source whereas analytical functions are not, what is interpreted by proponents of parametric methods as a double-edged sword because everything in an image can be modeled, down to the noise. But, as it will be seen later, this possibility can be easily avoided with really simple techniques as the introduction of a chi square test.

Parametric fitting methods are based on well-known analytical profiles with shapes similar to the standard galaxies, and they can be divided in two groups: 1D and 2D techniques. At first sight, 1D methods can seem archaic and obsolete compared to 2D ones, but they still have their followers. The main arguments supporting them are the fact that they are straightforward to implement and that elliptical models are not suitable to be used for galaxies with irregular features or isophotal twists (Peng et al. (2010)). However, many other arguments against 1D analysis can be also stated. Ambi-

guity in the way to extract 1D profiles is the principal one: several choices have been used, as the major or the minor axis or the profiles along spiral arms or isophotal twists. None of them has been proved to be optimal, and in extremely complex cases as overlapping sources or galaxies with double nuclei, it is difficult to even define one of those. Another highly important disadvantage of 1D methods is that convolution in single dimension is not mathematically equivalent to the bidimensional one, so the PSF deconvolution of the images is not feasible.

The first parametric fitting work is due to de Vaucouleurs (1948), who discovered that many galaxies had profiles which could be adjusted by means of an exponential of the form $\exp(r^{1/4})$. Several years later, Sérsic (1963) generalized this function with the so named Sérsic profile:

$$f(r) = \Sigma_e e^{-k\left[(r/r_e)^{1/n}-1\right]} \tag{1.1}$$

where r_e is the effective radius of the galaxy, Σ_e is the surface brigthness at r_e, n is the power-law index, and k is coupled to n such that half of the total flux is always within r_e. Freeman (1970) showed that most spirals and S0 galaxies have two main components: an spheroidal bulge with a de Vaucouleurs profile and an exponential disk component. This work was continued by Kormendy (1977), who confirmed this result but added that the contribution of the spheroid to the exponential parameters was large and the transition between the components was so sharp that one of them must have a cutoff. This disk/bulge decomposition technique developed by Kormendy was later applied by Burstein (1979) and new estimations of the parameters for S0 galaxies were found, as well as a detailed comparison with elliptical and spiral ones. But progress on this procedure would not come until 1981, when Boroson (1981) studied a new sample of spiral galaxies using this disk/bulge technique with a great improvement in the fitting algorithm which made use of all the large-scale spatial information on the plates. The innovation consisted on fitting each one of the two components in regions where their light dominates and subtracting them before the other component is solved for. This process was iterated until convergence was achieved. The two methods were applied to an exhaustive sample of 105 morphological types in Kent (1985), what allowed to a deep statistical study of the parameters values and the correlation among them and the Hubble type of the galaxies. PSF convolution is also introduced in this work by means of the convolution of the theoretical profiles with a Gaussian, avoiding in this way the trick of excluding of the central points of the profile, a usual technique at that time.

A different approach to the 1D analysis would be introduced by Andredakis & Sanders (1994) who, analyzing a sample of late-type spirals, discovered that these ones were better described using an exponential disk plus an exponential bulge. A few years later, MacArthur et al. (2003) expanded the usual approach modeling the bulge as a generalized Sérsic profile and applying 1D and 2D non-linear minimization routines. The result found that a large multiwavelength data set of Type-I late-type spiral galaxies had a Sérsic index ranging from 0.1 to 2 on average. An alternative way that was also considered was the introduction of a thick disk (van der Kruit & Searle (1981)). In the case of Bahcall & Kylafis (1985), a comparison between a thin disk model and a thin disk plus a thicker one was performed using a set of Sb and later type galaxies, and concluding that both models described the

observations properly.

When it comes to 2D parametric fitting, one of the first works we found in the literature was presented by Shaw & Gilmore (1989), where two edge-on spiral galaxies were analyzed. They found that one of them was well described using a two component model, whereas the other one needed a third component. Amazingly the authors discovered that none of the best-fit model combinations contained the de Vaucouleur profile. Although the analysis of the two-dimensional projection of the light distribution of the galaxies supposed a great advance, new problems arose, like how the inclination of the objects could affect the result and, concretely, the estimation of the parameters (Byun & Freeman (1995)). They finally solved the problem by adjusting two-dimensional projections of both a de Vaucouleurs bulge component and an exponential disk one.

A new method arose with the works by de Jong (1996) to get a better fit of those deviations of the usual profiles observed in bulges of edge-on spirals, like bars, arms or dust lanes. Its 2D fitting technique consisted on a three components model: an spherically symmetrical exponential bulge, an exponential disk and a Freeman bar, being the first one convolved with a Gaussian to account for the seeing effects. In addition, a weight exponential function was introduced in the χ^2 minimization process to decrease relative errors in the linear scale. It is also worth mentioning the work by Moriondo et al. (1998), who analyzed a new sample of early-type spirals by means of a two-dimensional generalized exponential bulge plus an exponential thin disk, providing the general analytic expressions for both of them:

$$\begin{aligned} I_b(x,y) &= I_e \exp\left\{-\alpha_n\left[\left(\frac{1}{r_e}\sqrt{x^2+\frac{y^2}{(1-\epsilon_b)^2}}\right)^{1/n}-1\right]\right\} \\ I_d(x,y) &= I_d(0)\exp\left[-\frac{1}{r_d}\sqrt{x^2+\frac{y^2}{\cos^2 i}}\right], \end{aligned} \tag{1.2}$$

where I_e and r_e are effective (half-light) values, ϵ_b is the apparent bulge ellipticity, and α_n is a constant relating the effective brightness and radius to the exponential values.

Due to the arrival of new, more accurate data from HST and WFPC2, some authors like Ratnatunga et al. (1999), stated the necessity of finding the optimal choice of number and kind of parameters to fit an extended image, decision that had been arbitrarily taken in the previous works. They discovered that using too few parameters in the decomposition could bias them, whereas fitting too many of them could cause the algorithm to converge to a false local minimum. To solve it, they developed a two-dimensional maximum likelihood image analysis software which optimized both the model and the number of parameters simultaneously, being able to create both disk and bulge decompositions and circularly symmetric sources. As an extension of Byun & Freeman (1995) works, Wadadekar et al. (1999) displayed three components fittings but taking into account the effects of the convolution with the PSF and the photon noise from sky background and the galaxy, as well as trying to quantify effects of other features like foreground stars on parameter extraction.

However, the revolution in two-dimensional parametric fitting arrived with GIM2D (Simard (1998)), an IRAF package which implemented the whole pipeline for a complete and automated morphology analysis based on the bulge and disk decomposition and the Metropolis Algorithm to find the best parameter values. The module performed several tasks such as the cosmic ray rejection, the data quality mask creation, the source detection as well as its deblending and extraction, and, finally, the bulge+disk surface brightness profile decomposition. This powerful tool was later used to automatically process the largest sample of data for morphological classification at that date (Simard et al. (2002)): 7450 galaxies in the Groth Strip, observed by HST.

After GIM2D opened the way to automated morphology analysis, the most important software in the area arrived thanks to Peng et al. (2002). GALFIT, a two dimensional fitting algorithm specialized on nearby galaxies observed with very high spatial resolution, improved all the previous techniques by being able to simultaneously fit a galaxy with an arbitrary number of components in a very short computation time. In addition, they introduced new profiles in the analysis in addition to the well known Sérsic and exponential functions, as the Nuker law or the Moffat/Lorentzian profile. GALFIT is widely used, so a deeper description of is carried out in section 2.1. By way of comparison, Häusler et al. (2007), tested these two automated softwares for fitting single-component Sérsic models to both simulated and real galaxy data. Conclusions were clear: for medium depth data, GALFIT behaved much better than GIM2D, not only because results were more reliable on average, but also because the former had lower scatter and less sensitivity to contamination by neighbours than the latter one. However, some worried about degeneracies in GALFIT, since in several cases a single component in a galaxy could be fitted by various different functions. That is the case of de Souza et al. (2004), who later implemented BUDDA, a bulge/disk decomposition software where no other components were included apart from a generalized Sérsic profile for the bulge and an exponential for the disk. In the following years, the code underwent several improvements, including the posibility of also fitting bars and a central source of light, advantage that was taken by Gadotti (2008) to study the impact of these components using a sample of 17 nearby galaxies hosting bars and AGNs. A two-dimensional bar-bulge-disk decomposition was also applied by Laurikainen et al. (2004) to 180 spiral galaxies in the Ohio State University Bright Galaxy Survey to study the bar-induced perturbation strengths.

In contrast to this traditional analytical profile fitting, the non-parametric approach does not involve deciding a priori which functional form to use or how many components to include, as it is the case of one of the most popular methods, the decomposition by means of orthonormal bases, which can be multiscaled or within one single scale. The former have bases built by dilating and contracting one or two original patterns; therefore, each element of the basis is characterized by a different scale, what leads to a multiresolution analysis (Starck (2001)). In this way, although coefficients of this decomposition are meaningless from the physical point of view, they can be interpreted as the splitting of the original galaxy into smoothed versions of it (large scale basis functions or low frequencies) and its detailed features (small scales or high frequencies). Examples of this kind of orthonormal bases techniques are the wavelet transforms and their by-products, such as the ridgelet or the curvelet transforms. On the other hand, in single scale methods a set of basis functions with different shapes

is developed for a fixed scale. The aim is not to carry out a multiresolution analysis, but a complete decomposition of the images once a certain scale is chosen, although a complete basis is available for each value of the scale parameter. Techniques like the shapelets or the CHEFs are included in this group.

Wavelet methods are based on the existence of two standard functions ϕ and ψ, named respectively the scaling and the wavelet functions, and their scaled versions. The first one is related to the low frequencies present in the objects to analyze in such a way that it represents coarser versions of the data, while the second one deals with the high frequencies, so it is mainly interested in small features and details (Mallat (1998); Starck & Murtagh (2002)). The most used wavelet transform is the decimated bi-orthogonal (OWT) one which decomposes objects in several layers of smoothed images plus detailed ones, and using dyadic scales. Each level of the decomposition needs half the number of coefficients than the previous one so, due to its compactness, this representation has been widely used for image compression tasks. However, the undecimated version of this algorithm (UWT) has been also extensively considered in spite of being an overfitting technique, since it is highly suitable for data filtering (Starck (2001)). Another well-known wavelet method is the à trous algorithm, which decomposes sources into a single coarse version and several layers with the details of each scale size. This is the most popular wavelet technique in astronomical image processing, since it is extremely well adapted to the detection of isotropic features (Starck & Murtagh (2002)).

Ridgelet transform arises when applying a one-dimensional wavelet transform to ridge functions (Candès & Donoho (1999)). In fact, it can be proved that ridgelet transform is exactly the application of a one-dimensional wavelet to the slices of the Radon transform where the angular variable θ is constant and t is varying. This makes this decomposition greatly adapted to detect line segments in images, with a size depending on the chosen partition of the image. If this partition is not homogeneously performed, but into dyadic blocks, and the ridgelet transform is applied to each one of them, the result is the so called curvelet transform (Starck et al (2003)). This kind of multiscale ridgelet pyramid is therefore optimal to find curved structures in the sources being analyzed.

Once it is understood that every type of transform brings out a different kind of feature, the decision of which one to apply is not trivial, specially when it comes to astronomical images, where many complex structures can be found simultaneously. Because of that, Starck (2001) developed a combined method to mix them and get an optimal representation. It just consisted on composing a new transform from the linear combination of the simple ones and minimizing the norm of the residual between the original source and the so built combined model, just adding a penalty term. The coefficients of the optimized linear combination indicated which transforms had to be applied and how much they had to be weighted.

When it comes to single-scaled algorithms by orthonormal bases, the most popular one in astronomical imaging is, by far, the shapelet transform. In this technique, basis functions are perturbations around a two-dimensional Gaussian, using Hermite polynomials (Refregier (2003); Massey & Refregier

(2005)). The crucial point of this ensemble of functions is that they are scaled by a factor β according to the size of the galaxy which is desired to be analyzed. In these way, a complete and compact orthonormal basis is constructed for each value of β. A extensive description of shapelets will be found in section 2.2.

1.3. The CHEF basis

As it has been mentioned above, several large surveys with greater and more complex ensembles of data are being developed and the trend for future projects is to have more of this. Dramatic advances in instrumentation must be accompanied by similar developments in analysis techniques, not only for computational improvements but also for the implementation of new algorithms and mathematical tools. In the previous section, parametric fitting techniques have proved to be unable to deal with the new generation of datasets, while the non-parametric, more recently developed algorithms are not totally complete, requiring either a high amount of interactivity from the user or displaying different levels of accuracy depending of the data being analyzed.

For all these reasons, a new non-parametric method, the CHEF orthonormal bases, has been developed. Based on a polar composition of Chebyshev rational functions and Fourier series, this combination has been chosen due to the periodicity of Fourier modes and the remarkable properties of efficiency of Chebyshev polynomials when fitting functions in the [-1,1] interval, as their minimax property states (Mason & Handscomb (2002)). The result is a complete and orthonormal set of basis functions very well suited to fit astronomical objects able to fully model the whole flux of a galaxy to very large radii using a small number of coefficients. In addition, these bases have revealed to be enormously efficient when implementing many other practical applications apart from the simple morphological modeling, as for instance, shear estimation, morphological and photometric parameters calculation, PSF deconvolution or clusters processing.

In chapter 2, we present the mathematical definition of the CHEF basis, demonstrate the fast decay rate of the coefficients, what ensures the compactness of the basis, and derive the main galaxy parameters from the decomposition coefficients. A description of the two most currently used techniques in astronomical image processing, GALFIT and the shapelets, is also included. Chapter 3 focuses on the practical implementation of the algorithm, describing how to discretize the basis and choose the free parameters of the fit, namely the scale size, the center and the decomposition order, and describes our functioning pipeline, which is being used to process data from different surveys. Chapter 4 shows the application of the method to different datasets, both real and simulated, and discusses its performance compared with that of shapelets. In chapter 5 the first applications designed for Astrophysics are described, as well as the corresponding tests to check their accuracy, whereas chapter 6 states the main conclusions of the thesis.

Bibliography

Abbott, T. et al. (2005). The Dark Energy Survey, arXiv:astro-ph/0510346.

Andredakis, Y.C; Sanders, R.H. (1994). Exponential bulges in late-type spirals: an improved description of the light distribution. MNRAS, 267, 283-296. ApJ, 288, 252-258.

Bahcall, J.N; Kylafis, D. (1985). On the spatial distribution of population II stars in Sb and later type galaxies. ApJ, 288, 252-258.

Benítez, N. et al. (2009). Measuring Baryon Acoustic Oscillations Along the Line of Sight with Photometric Redshifts: The PAU Survey. ApJ, 691, 241-260.

Boroson, T. (1981). The distribution of luminosity in spiral galaxies. The Astrophysical Journal Supplement series, 46, 177-209.

Burstein, D. (1979). Structure and origin of S0 galaxies. II. Disk-to-bulge ratios. The Astrophysical Journal, 234, 435-447.

Byun, Y.I; Freeman, K.C. (1995). Two-dimensional decomposition of bulge and disk. ApJ, 448, 563-574.

Candès, E; Donoho, D. (1999). Ridgelets: the key to high dimensional intermittency?. Phil. Trans. R. Soc. Lond., 357, 2495-2509.

de Jong, R.S. (1996) Near-infrared and optical broadband surface photometry of 86 face-on disk dominated galaxies. II. A two-dimensional method to determine bulge and disk. Astronomy and Astrophysics Supplement Series, 118, 557-573.

de Souza, R.E; Gadotti, D.A; dos Anjos, S. (2004). BUDDA: a new two-dimensional bulge/disk decomposition code for detailed structural analysis of galaxies. The Astrophysical Supplement Series, 153, 411-427.

de Vaucouleurs, G. (1948). Sur la technique de lánalyse microphotemétrique des nebuléuses brillantes. Annales dÁstrophysique,11, 247.

Donoho, D.L; Huo, X. (2002). Beamlets and multiscale image analyisis. In Multiscale and Multiresolution methods. Springer Lectures in Computational Science and Engineering, 20, 149-196.

Freeman, K.C. (1970). On the disks of spiral an S0 galaxies. ApJ, 160, 811.

Gadotti, D.A. (2008). Image decomposition of barred galaxies and AGN hosts. MNRAS, 384, 420-439.

Häussler, B; McIntosh, D.H; Barden, M; Bell, E.F; Rix, H.W; Borch, A; Beckwith, S.V.W; Caldwell, J.A.R; Heymans, C; Jahnke, K; Jogee, S; Koposov, S.E; Meisenheimer, K; Sánches, S.F; Somerville, R.S; Wisotzki, L; Wolf, C. (2007). GEMS: Galaxy fitting catalogs and testing parametric galaxy fitting codes: GALFIT and GIM2D. The Astrophysical Journal Supplement Series, 172, 615-633.

Ivezic, Z. et al. (2008). LSST: from science drivers to reference design and anticipated data products, arXiv:0805.2366.

Kaiser, N. et al. (2002). Pan-STARRS – A large synoptic survey telescope array, in Proceedings of the SPIE, 4836, 154.

Kent, S.M. (1985). CCD surface photometry of field galaxies. II. Bulge/disk decompositions. The Astrophysical Journal Supplement Series, 59, 115-159.

Kormendy, J. (1977). Brightness distributions in compact and normal galaxies. III. Decomposition of observed profiles into spheroid and disk components. The Astrophysical Journal, 217, 406-419.

Laurikainen, E; Salo, H; Buta, R; Vasylyev, S. (2004). Bar-induced perturbation strengths in the Ohio State University Bright Galaxy Survey - I. MNRAS, 355, 1251-1271.

MacArthur, L.A; Courteau, S; Holtzman, J.A. (2003). Constraints on bulge formation scenarios. Rev. Mex. A. A. (Serie de conferencias), 17, 180-181.

Mallat S. G. (1998). A wavelet tour of signal processing. Academic Press, 637pp, London.

Margon, B. (1998). The Sloan Digital Sky Survey, arXiv:astro-ph/9805314v2.

Mason, J.C., & Handscomb, D.C. (2002). Chebyshev polynomials.

Massey, R; Refregier, A. (2005). Polar shapelets. MNRAS, 363, 197-210.

Moriondo, G; Giovanardi, C; Hunt, L.K. (1998). Near-infrared surface photometry of early-type spiral galaxies. I. Bulge and disk decomposition. Astronomy and Astrophysics Supplement Series, 130, 81-108.

Peng, C.Y; Ho, L.C; Impey, C.D; Rix, H.W. (2002). Detailed structural decomposition of galaxy images. The Astronomical Journal, 124, 266-293.

Peng, C.Y; Ho, L.C; Impey, C.D; Rix, H.W. (2010). Detailed decomposition of galaxy images. II. Beyond axisymmetric models. The Astronomical Journal, 139, 2097-2129.

Ratnatunga, K.U; Griffiths, R.E; Ostrander, E.J. (1999). Disk and bulge morphology of WFPC2 galaxies: the Hubble Space Telescope Medium Deep Survey database. The Astronomical Journal, 118, 86-107.

Refregier, A. (2003). Shapelets: I. Amethod for image analysis. MNRAS, 338, 1, 35-47.

Sérsic, J.L. (1963). Influence of the atmospheric and instrumental dispersion on the brightness distribution in a galaxy. Boletín de la Asociación Argentina de Astronomía, 6, 41.

Shaw, M.A; Gilmore, G. (1989). The luminosity distributions of edge-on spiral galaxies - I. A two dimensional model and its application to NGC891 and 4565. MNRAS, 237, 903-927.

Simard, L. (1998). GIM2D: An IRAF package for the quantitative morphology analysis of distant galaxies. Astronomical Data Analysis Software and Systems VII, ASP Conference Series, 145, 108-111.

Simard, L; Willmer, C.N.A; Vogt, N.P; Sarajedini, V.L; Phillips, A.C; Weiner, B.J; Koo, D.C; Im, M; Illingworth, G.D; Faber, S.M. (2002). The Deep Groth Strip Survey. II Hubble Space Telescope structural parameters of galaxies in the Groth Strip. The Astrophysical Journal Supplement Series, 142, 1-33.

Starck, J.L; Murtagh, F. (2002). Astronomical image and data analysis. Springer-Verlag, 289pp, Germany.

Starck, J.L. (2001). Astronomical image decomposition using wavelets, ridgelets, and curvelets: the combined transforms method. Proc. SPIE, Astronomical Data Analysis, 4477, 131-141.

Starck, J.L; Donoho, D.L; Candès, E.J. (2003). Astronomical image representation by the curvelet transform. A&A, 398, 785-800.

van der Kruit, P.C; Searle, L. (1981) Surface photometry on edge-on spiral galaxies. A& A, 95, 105-115.

Wadadekar, Y; Robbason, B; Kembhavi, A. (1999). Two-dimensional galaxy image decomposition. The Astronomical Journal, 117, 1219-1228.

2

Mathematical background and results

Image processing and analysis is a widely used tool which has become essential not only for Astrophysics but also for many other science fields as, for instance, Medicine, Biology or Chemistry. The necessity of extracting hidden information, that is, information which is not obvious from the usual point of view (in mathematical terms, the space-time domain) has made scientists develop new ways of looking at the data, shifting them to different domains. The better known approach is the translation of the data to the frequency domain, that is, the Fourier transform, although many other methods have been developed, as the cosine, the Laplace, the Radon or the wavelet transforms. The later has encouraged the development of many other wavelet-based techniques, as the ridgelet or the curvelet transforms. In Astrophysics, specific methods to analyze and decompose galaxy images have been created, with the GALFIT fitting (Peng et al. (2002)) and the shapelet transform (Refregier (2003)) being the most widely used ones nowadays.

GALFIT (Peng et al. (2002, 2010)) is a so called parametric fitting algorithm. That means that models are built as linear combinations of analytical functions, then the optimal values of the parameters for each component are found. Depending on the kind of the analytical profiles chosen for the modeling and the way the optimization is performed, different parametric fitting methods are obtained. On the other hand, shapelets constitute an example of a non-parametric fitting method, what means that reconstructions are based on a set of orthonormal functions which mathematically constitutes a basis in the Hilbert space of the smooth enough functions. The parameters to optimize in this case are usually the size (or scale) of the basis functions and the weights of the linear combination that composes the model.

Parametric techniques are obviously simpler to implement and the resulting parameters are much easier to understand and interpret. They are often related to the physical properties of the galaxies, as the size, the axis ratio or the position angle for example, and this leads to direct comparisons with other galaxies in a statistical fashion. In addition, the analytical functions are usually selected to mimic the shape of the galaxies being analyzed, thus provides a straightforward physical inter-

pretation. However, many of these parameters depend non-lineally on the rest of the variables, what makes the optimization step much more difficult and, in some cases, reaching the best value for them is not guaranteed since the possibility of lying on a local minimum is higher than with lineal techniques.

On the other hand, the complexity of non-parametric fitting techniques is a disadvantage; they are much more difficult to implement, and the shapes of the individual components often bear little resemblance to the galaxies being reconstructed, what makes the result harder to interpret. In addition, the parameters of the reconstruction have no direct link to the physical properties of the images, since they mathematically express just the contribution of each component to the global model. However, and despite these technical issues, the reliability and adaptability of non-parametric methods to efficiently model the vast majority of morphology types is matchless. Analytical techniques are highly constrained by their own profile shapes, so irregular galaxies or those ones displaying a large amount of substructure are not properly modeled. Unlike them, orthonormal bases methods are capable of reconstruct every significative feature present in the image, due to their great flexibility.

In this chapter, after describing the already existing GALFIT and shapelet techniques, we will introduce the CHEF orthonormal bases, the main subject of this thesis. Built in polar coordinates using Chebyshev rational functions and Fourier series, CHEFs constitute a non-parametric fitting method capable of reaching an excellent trade-off between the two aforementioned techniques, solving the problems and deficiencies these two approaches present. In particular, CHEFs are able to reconstruct galaxies with morphologies that GALFIT cannot deal with and they get the same accuracy both in the central bulge and the extended wings of the reconstructed model, problem that shapelets often manifest.

2.1. GALFIT fitting

GALFIT (Peng et al. (2002, 2010)) is a two-dimensional parametric fitting algorithm based on some well-known mathematical profiles as, for instance, the Nuker law, the Sérsic, King, and Ferrer profiles, the exponential disk and Gaussian and Moffat functions. Written in C language, GALFIT software allows the user to fit the galaxies using an arbitrary number of components with a wide variety of profile types simultaneously. In the initial version of the software, their shape was always ellipsoidal, what yielded many advantages, as the simplicity in the interpretation of the parameters (size, axis ratio or position angle, for instance), and its great capability to perform highly accurate models to fit simple elliptical or spherical galaxies with a small number of components. However, for more complex morphologies, these elliptical shapes were not enough, since they were absolutely incapable of efficiently reproduce detailed features in the galaxies, as spiral arms, axial twists or bars. Because of that, the last improvement of GALFIT software (Peng et al. (2010)) included the concepts of Fourier modes and coordinate rotation functions. This version implement azimuthal projections as a series expansion of Fourier modes, what allows the user to reproduce a wide range of isophotal shapes, whereas the coordinate rotation method produces the rotation of the isophotes as a function

of radius, what yields excellent results when dealing with isophotal twists.

Basically, the operation of GALFIT software consists on providing an input file to the program, where the user must specify the number and type of the components he desires to use for the fitting. In addition, the approximate values of the parameters for these components must be also introduced, so the algorithm will apply the Levenberg-Marquardt downhill-gradient method (Press et al. (1992)) until the minimization of the residual between the original data and the resulting multi-component model is achieved and, therefore, the optimal values of the parameters are found. An example of a GALFIT input file is shown in figure 2.1, where a two components model is required: a Sérsic profile plus an exponential disk. Let us detailedly explain the parameters appearing in this file.

Headers in GALFIT files always contain information about the image to be modeled and technical issues about its observation (*"IMAGE and GALFIT CONTROL PARAMETERS"*). Basic data as the name of both the input and the output fits images, the noise map and PSF files or bad pixel masks and parameters constraints are specified here. The rectangular region to be fitted inside the input image file and the size of the convolution box must also be determined in this header, as well as observational parameters as the magnitude of the photometric zeropoint and the pixel scale. All this information can be easily extracted by the users just by looking at the input image header.

In the *"INITIAL FITTING PARAMETERS"* section, the analytical components and their starting parameters are introduced. Analytical models available are:

- Sérsic profile:
$$f(r) = \Sigma_e \, \mathrm{e}^{-\kappa[(r/r_e)^{1/n}-1]},$$
where r_e is the effective radius of the galaxy, Σ_e the surface brightness at r_e, n the power law index, and κ is coupled to n such that half of the total flux is always within r_e.

- Exponential disk profile:
$$f(r) = \Sigma_0 \, \mathrm{e}^{-r/r_s},$$
where Σ_0 is the central surface brightness and r_s is the disk scale length.

- Nuker law:
$$f(r) = I_b 2^{(\beta-\gamma)/\alpha} \left(\frac{r}{r_b}\right)^{-\gamma} \left[1 + \left(\frac{r}{r_b}\right)^{\alpha}\right]^{(\gamma-\beta)/\alpha},$$
where γ is the slope of the inner power law, β is the slope of the outer one, r_b is the location where the profile changes slope, I_b is the surface brightness at r_b, and α describes how sharply the two power laws connect.

- Gaussian profile:
$$f(r) = \Sigma_0 \, \mathrm{e}^{-r^2/2\sigma^2},$$
where Σ_0 is the central surface brightness and σ is related to the full width half maximum (FWHM) by means of $FWHM = 2{,}355\sigma$.

```
================================================================================
# IMAGE and GALFIT CONTROL PARAMETERS
A) 341.0_orig.fits     # Input data image (FITS file)
B) 341.0_galfit_out.fits    # Output data image block
C) none                # Sigma image name (made from data if blank or "none")
D) psf_02.fits               # Input PSF image and (optional) diffusion kernel
E) 1                   # PSF fine sampling factor relative to data
F) none                # Bad pixel mask (FITS image or ASCII coord list)
G) none                # File with parameter constraints (ASCII file)
H) 1  108  1  108      # Image region to fit (xmin xmax ymin ymax)
I) 108   108           # Size of the convolution box (x y)
J) 21.1                # Magnitude photometric zeropoint
K) 0.2  0.2            # Plate scale (dx dy)    [arcsec per pixel]
O) regular             # Display type (regular, curses, both)
P) 0                   # Create ouput only? (1=yes; 0=optimize)
S) 0                   # Modify/create objects interactively?

# INITIAL FITTING PARAMETERS
#
#   For object type, the allowed functions are:
#       nuker, sersic, expdisk, devauc, king, psf, gaussian, moffat,
#       ferrer, powsersic, sky, and isophote.
#
#   Hidden parameters will only appear when they're specified:
#       C0 (diskyness/boxyness),
#       Fn (n=integer, Azimuthal Fourier Modes),
#       R0-R10 (PA rotation, for creating spiral structures).
#
# ------------------------------------------------------------------------------
#   par)    par value(s)    fit toggle(s)    # parameter description
# ------------------------------------------------------------------------------

# Object number: 1
 0) sersic                 #  object type
 1) 54.354 54.715  1 1     #  position x, y
 3) 5.65472     1          #  Integrated magnitude
 4) 3.04327     1          #  R_e (half-light radius)   [pix]
 5) 3.5         1          #  Sersic index n (de Vaucouleurs n=4)
 6) 0.0000      0          #     -----
 7) 0.0000      0          #     -----
 8) 0.9410      1          #  axis ratio (b/a)
 9) -25.7       1          #  position angle (PA) [deg: Up=0, Left=90]
10) 0.0         1          #  diskiness/boxiness
 Z) 0                      #  output option (0 = resid., 1 = Don't subtract)

# Object number: 2
 0) expdisk                #  object type
 1) 54.354 54.715  1 1     #  position x, y
 3) 20.6318     1          #  Integrated magnitude
 4) 9.02307     1          #  R_e (half-light radius)   [pix]
 6) 0.0000      0          #     -----
 7) 0.0000      0          #     -----
 8) 0.7650      1          #  axis ratio (b/a)
 9) -32.7       1          #  position angle (PA) [deg: Up=0, Left=90]
10) 0.0         1          #  diskiness/boxiness
 Z) 0                      #  output option (0 = resid., 1 = Don't subtract)

# Object number: 3
 0) sky                    #  object type
 1) 0.0255      1          #  sky background at center of fitting region [ADUs]
 2) 0.0000      0          #  dsky/dx (sky gradient in x)
 3) 0.0000      0          #  dsky/dy (sky gradient in y)
 Z) 0                      #  output option (0 = resid., 1 = Don't subtract)

================================================================================
```

Figure 2.1 Example of input file for GALFIT, with a two components model.

- Moffat/Lorentzian profile:

$$f(r) = \frac{\Sigma_0}{[1 + (r/r_d)^2]^n},$$

where Σ_0 is the central surface brightness,r_d is the dispersion radius, and n is the power law index.

In the particular example shown in figure 2.1, a Sérsic profile and an exponential disk are chosen. For both of them, the coordinates of the center, the integrated magnitude, the half-light radius, the axis ratio, and the position angle must be indicated. Initial estimates can be easily obtained by running SExtractor on the original image and asking for these parameters to the output catalog. In the case of the Sérsic profile, an additional number is required, the so called Sérsic index, which is related to the steepness of the source being decomposed, as it was explained previously.

Finally, a third component is taken into account: the background. The most important parameter for the sky is the level of noise present in the image, what can be easily estimated by running IRAF tasks or taken the value provided by SExtractor.

It is worth mentioning that even if the complete set of parameters has been accurately estimated, in many cases the GALFIT minimization algorithm crashes, what makes the user modify slightly the value of some of the inputs, preferentially, the Sérsic index. However, convergence of the method does not guarantee an optimal result either, since the technique has been shown to converge often to local minima depending on the initial parameters.

2.2. Shapelets

Shapelets arose as an alternative to the traditional parametric fitting of galaxies of GALFIT and the multiresolution image analysis provided by wavelets. Sharing the ideas of orthogonal bases and single scale methods, shapelets are defined as an infinite set of orthonormal functions which represents a basis of the space of smooth and integrable functions (Refregier (2003)). These functions are thought of as shape perturbations around the two-dimensional Gaussian or weighted Hermite polynomials. In fact, shapelet functions $\phi_{n,m}$ were first developed in cartesian coordinates:

$$\{S_{n,m}(x_1, x_2; \beta)\}_{n,m} = \left\{ \frac{H_n(x_1/\beta) H_m(x_2/\beta)\, \mathrm{e}^{-\sqrt{x_1^2+x_2^2}/2\beta^2}}{\beta 2^n \sqrt{\pi n! m!}} \right\}_{n,m}, \tag{2.1}$$

where $H_n(x)$ is the Hermite polynomial of order n (Abramowitz & Stegun (1970)) and β is the so called shapelet scale size, which varies the speed of the Hermite polynomials to reach their extrema. As this set can be proved to form an orthonormal and complete basis of the space of smooth enough functions, every object f can be expressed as a linear combination of these functions:

$$f(x_1, x_2) = \sum_{n=0}^{\infty} \sum_{m=0}^{\infty} f_{n,m} S_{n,m}(x_1, x_2; \beta), \tag{2.2}$$

where the $f_{n,m}$ are the so named shapelet coefficients and are uniquely determined by evaluating the integral:

$$f_{n,m} = \iint\limits_{\mathbb{R}^2} f(x_1, x_2) S_{n,m}(x_1, x_2; \beta)\, dx_1\, dx_2. \tag{2.3}$$

Cartesian shapelets display a wide range of smart mathematical properties (Refregier (2003)), such as their invariance under Fourier tranforms (up to a rescaling) or the fact that they are the eigenstates of the two-dimensional Quantum Harmonic Oscillator whose Hamiltonian is

$$\hat{H} = \frac{1}{2}\left[\hat{x}_1^2 + \hat{x}_2^2 + \hat{p}_1^2 + \hat{p}_2^2\right], \tag{2.4}$$

where $\hat{x}_i$ and $\hat{p}_i$ are the position and momentum operators respectively for each dimension.

Although this cartesian approach resulted very useful, polar shapelets (Massey & Refregier (2005)) were soon developed as a more intuitive and convenient expression, since they allowed to separate an image into components with explicit rotational symmetries. Polar shapelet basis functions $\chi_{n,m}$ are separable in the radial and the angular coordinates:

$$\{\chi_{n,m}(r,\theta;\beta)\}_{n,m} = \left\{ \frac{(-1)^{(n-|m|)/2}}{\beta^{|m|+1}} \left\{ \frac{[(n-|m|)/2]!}{\pi[(n+|m|)/2]!} \right\}^{1/2} r^{|m|} L^{|m|}_{(n-|m|)/2}\left(\frac{r^2}{\beta^2}\right) \mathrm{e}^{-r^2/2\beta^2}\, \mathrm{e}^{-im\theta} \right\}_{n,m}, \tag{2.5}$$

where the $L_p^q(x)$ are the Laguerre polynomials (Abramowitz & Stegun (1970)), which are related to Hermite polynomials used in cartesian shapelets by means of:

$$H_{n,m}(x) = (-1)^n n!\, x^{m-n} L_n^{m-n}(x^2) \tag{2.6}$$

being $m > n$. With these polar shapelets, decomposition of any smooth enough function $f(r,\theta)$ becomes:

$$f(r,\theta) = \sum_{n=0}^{\infty} \sum_{m=-n}^{n} f_{n,m} \chi_{n,m}(r,\theta;\beta), \tag{2.7}$$

where the polar shapelet coefficients $f_{n,m}$ are calculated just evaluating the following integral:

$$f_{n,m} = \iint\limits_{\mathbb{R}^2} f(r,\theta) \chi_{n,m}(r,\theta;\beta)\, r\, dr\, d\theta. \tag{2.8}$$

Finally, cartesian shapelet coefficients $f_{n,m}$ can be transformed into polar ones $f_{n,m}$ by means of the relation:

$$f_{n,m} = 2^{-n/2} i^m \left\{ \frac{n!m!}{[(n+2)/2]![(n-m)/2]!} \right\}^{1/2} \delta_{n+m,n} \sum_{n'_r=0}^{m} \sum_{n'_l=0}^{n} i^m \begin{pmatrix} \frac{n+m}{2} \\ n'_r \end{pmatrix} \begin{pmatrix} \frac{n-m}{2} \\ n'_l \end{pmatrix} \delta_{n'_l+n'_r,n} f_{n,m}. \tag{2.9}$$

The applications of shapelet bases, both in their cartesian and polar forms, have been numerous. Explicit expressions for photometry and astrometry parameters from the coefficients have been develo-

ped, as well as a matrix direct process to deconvolve the PSF of galaxies. One of fields where they have been more often applied to is the study of the weak gravitational lensing (Chang & Refregier (2002); Refregier & Bacon (2003); Massey et al. (2004, 2007); Goldberg & Bacon (2005); Kuijken (2006); Heymans et al. (2006)) where different approaches to estimate shear from shapelet decompositions have been developed. The invariant behaviour of shapelets under a Fourier transform made them suitable to reconstruct images from interferometric observations (Chang & Refregier (2002)). These bases were also used by Massey et al. (2004) to simulate realistic astronomical images containing galaxies with complex morphologies and by Kuijken (2008) to carry out photometry measurements. A principal component analysis has been also performed with the shapelet coefficients of about 3000 galaxies from SDSS in order to get an automated morphological classification system (Kelly & McKay (2004)).

However, the applicability and reliability of shapelets have been discussed by (Melchior et al. (2007); Bosch (2010)), since these bases have proved to be suboptimal for galaxy decomposition. Troubles range from the loss of orthonormality (due to discretization, undersampling and boundary effects) to the wrong selection of the external parameters (errors in the optimal value of the number of coefficients to calculate, the scale parameter and the centroid, even although these values match with the minimum in the χ^2). But the most important limitation of shapelets is their own shape. Although they display oscillating cores that make them perfect to fit bulges of galaxies, shapelets functions have all wings that tend to vanish due to the Gaussian, what makes that reconstructions are affected by the intrinsic cut-off of this exponential. The worst consequence is that flux recovered by shapelet models is bounded by these wings, and this leads to a misestimation of the photometric parameters. It has been also proved that if the image to analyze displays a high ellipticity or or the intrinsic galaxy profile becomes steeper, the shapelet decomposition performs more poorly, what leads to a worrying misestimation of the ellipticity and therefore to a large bias in weak shear measurements (Melchior et al. (2010); Bosch (2010)). This problem has tried to be solved using elliptical shapelets, but they have shown to be also useless, since they depend critically in accurate ellipticity priors.

2.3. CHEF polar bases

CHEF polar bases were born with the aim of solving the problems displayed by methods like GALFIT and the shapelets. The fact that makes CHEFs behave better than these others is the combination of flexibility with the lack of radial slope constrains. The flexibility comes from the orthogonality property of the bases, which makes them able to fit any kind of morphology at different scales. The lack of radial slope constrains is due to the profile of rational Chebyshev functions, which tend to 1 at the infinity and, therefore, do not limit the modeling of any profile. In addition, as it is shown in figure 2.3.1, these rational Chebyshev functions have proved to be highly efficient in modeling decaying profiles, and their superiority against other methods is specially observed in highly steep or compact sources.

2.3.1. Definition of the basis

The *Chebyshev polynomial* $T_n(x)$ of first kind is a polynomial in x of degree n, defined by the relation

$$T_n(x) = \cos(n\theta) \tag{2.10}$$

with $x = \cos\theta$ (Mason & Handscomb (2003); Boyd (2000)). These polynomials are defined on the finite interval $[-1, 1]$ and they constitute a basis of the $\mathcal{L}^2$-space of squared-integrable, real-valued functions defined on $[-1, 1]$:

$$\mathcal{L}^2\left([-1,1]\right) = \left\{ f : [-1,1] \to \mathbb{R} \;\middle|\; \int_{-1}^{1} f^2(x)\,dx < \infty \right\}. \tag{2.11}$$

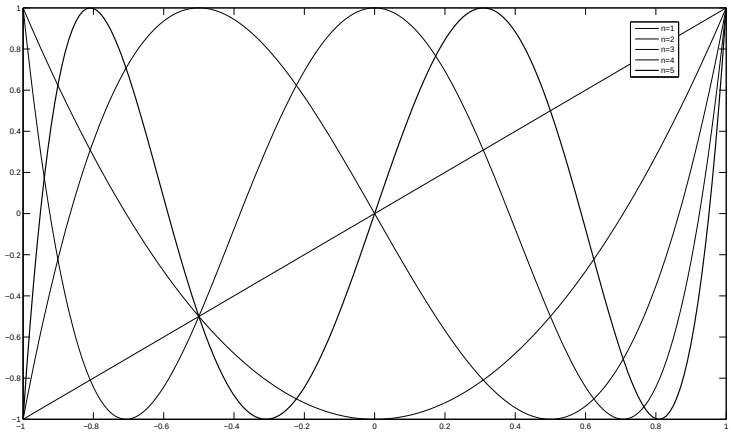

Figure 2.2 First five Chebyshev polynomials.

At the extrema of the domain interval, these polynomials do not vanish, but reach the value 1 or -1 (see figure 2.2). We want to use these Chebyshev polynomials to expand the radial component of galaxies, represented in polar coordinates, although they are defined on the interval $[-1, 1]$ instead of the semi-infinite interval $[0, +\infty)$ (as the radius is). Because of that, a rational function has been applied in such a way that the *rational Chebyshev functions* are defined by:

$$\begin{array}{rccl} TL: & [0,+\infty) & \longrightarrow & \mathbb{R} \\ & x & \longmapsto & TL_n(x) = T_n\left(\dfrac{x-L}{x+L}\right) = \cos\left(n \arccos\left(\dfrac{x-L}{x+L}\right)\right) \end{array} \tag{2.12}$$

where the parameter L will be called the *scale parameter* from now on and it is considered to be always strictly positive, thus application in (2.12) is well-defined. This scale parameter L is related to the "width" of the Chebyshev polynomial which each rational function comes from, that is, L works as an accordion, contracting and dilating the Chebyshev polynomials. The larger L is, the more slowly the extrema are reached, as it can be observed in figure 2.3.

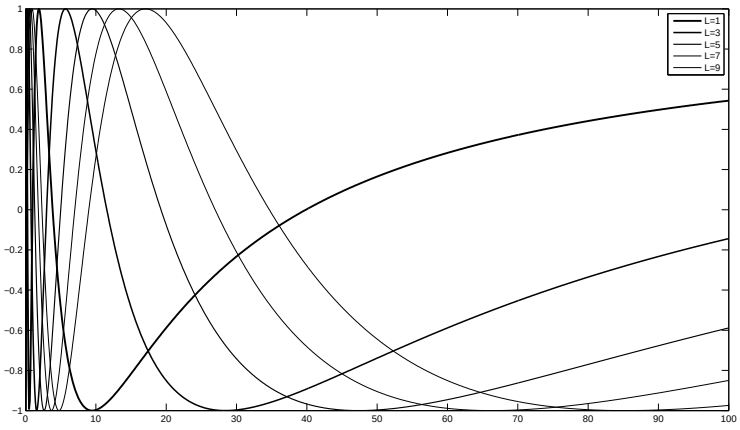

Figure 2.3 Chebyshev rational function of order $n = 5$ with different scale sizes.

As we can see, these rational Chebyshev functions tend monotously to one after their last minimum, more and more slowly as the order grows. They do not vanish quickly, as the shapelet radial components, and therefore CHEFs can fit extended galaxy wings of any shape. At small radii, they quickly oscillate and are thus capable of accurately describing the very fast change of flux with radius displayed by compact galaxies. The frontier between both regimes is roughly set by the scale parameter L. This very good adaptation to the actual properties of real galaxies is illustrated by figure 2.3.1 which shows the rational Chebyshev approximations to both a de Vaucouleur and a Sersic profile (with index $n_s = 0{,}75$), using different Chebyshev rational functions orders. It can be observed how they match quite tightly both profiles using just a few coefficients. (e.g. compare with fig. 2 from Bosch (2010)).

On the other hand, since f is a 2π-periodic function, its *Fourier series* can be defined as:

$$f \sim \sum_{n=-\infty}^{\infty} \hat{f}(n) e^{int}, \qquad \text{where } \hat{f}(n) = \frac{1}{2\pi} \int_{-\pi}^{\pi} f(t) e^{-int}\, dt, \tag{2.13}$$

and $\hat{f}(n)$ is called the *nth Fourier coefficient*. It can be proved (Katnelson (2004)) that if $f \in \mathcal{C}^1([-\pi,\pi]) = \left\{ f : [-\pi,\pi] \to \mathbb{R} \;\middle|\; \exists f', \text{with } f \text{ and } f' \text{continuous} \right\}$, then its Fourier series uniformly converges to the function f which is representing.

CHEF polar bases are built separably in polar coordinates, expanding the radial component using the rational Chebyshev functions described before and representing the angular coordinate by means of Fourier series, due to its 2π-periodicity (see figure 2.3.1). Thus, the following set of functions is considered:

$$\{\phi_{n,m}(r,\theta;L)\}_{n,m} = \left\{ TL_n(r) e^{im\theta} \right\}_{n,m}, \quad n \in \mathbb{N},\ m \in \mathbb{Z}. \tag{2.14}$$

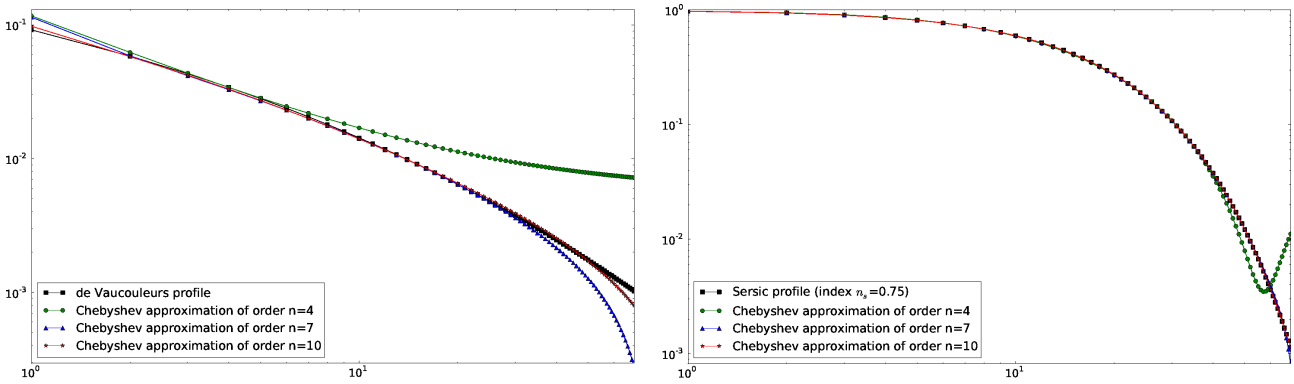

Figure 2.4 Chebyshev approximations to both a de Vaucouleurs and a Sersic profile (with index $n_s = 0{,}75$), using Chebyshev rational functions of different order n. Just a few coefficients provide high accuracy over several orders of magnitude.

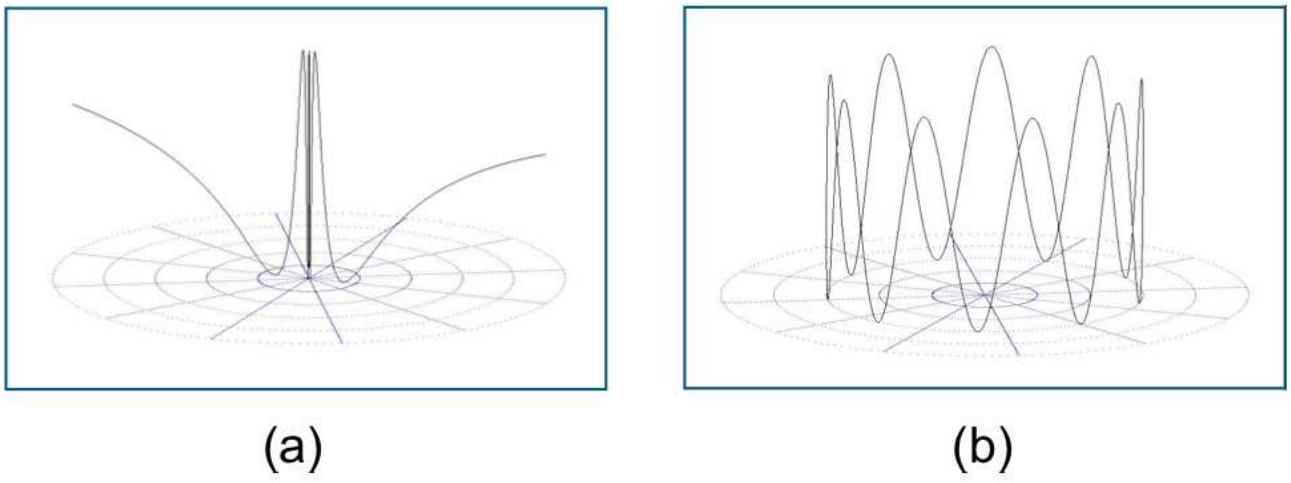

Figure 2.5 Construction of CHEF polar bases with (a) Chebyshev rational functions, and (b) Fourier series.

Let us prove that this set constitutes a basis of a certain space of functions and let us make it be orthonormal. In order to get these, it is first necessary to introduce some mathematical definitions. Let $\mathcal{L}^2\left([0,+\infty)\times[-\pi,\pi]\right)$ be the space of complex-valued functions f defined on polar coordinates such that the integral $\int_0^{\infty}\int_{-\pi}^{\pi}|f(r,\theta)|^2\,d\theta\,dr$ exists and is finite. Now, an operation in this space of functions is going to be introduced; given $f,g\in\mathcal{L}^2\left([0,+\infty)\times[-\pi,\pi]\right)$ we define an operation $\langle\cdot,\cdot\rangle$ by:

$$\langle f,g\rangle=\int_0^{\infty}\int_{-\pi}^{\pi}f(r,\theta)\,\overline{g(r,\theta)}\,\frac{1}{r+L}\sqrt{\frac{L}{r}}\,d\theta\,dr. \tag{2.15}$$

Proposition 2.1. *The operation defined in (2.15) constitutes an inner product in the* $\mathcal{L}^2\left([0,+\infty)\times[-\pi,\pi]\right)$ *space.*

Proof: In order to prove that (2.15) defines an inner product, four properties must be demonstrated. Let f, g and h be three functions in $\mathcal{L}^2\left([0,+\infty)\times[-\pi,\pi]\right)$, then:

1. Linearity of the sum:

$$\begin{aligned}\langle f+g,h\rangle &= \int_0^{+\infty}\int_{-\pi}^{\pi}\left[f(r,\theta)+g(r,\theta)\right]\overline{h(r,\theta)}\frac{1}{r+L}\sqrt{\frac{L}{r}}\,d\theta\,dr = \\ &= \int_0^{+\infty}\int_{-\pi}^{\pi}f(r,\theta)\,\overline{h(r,\theta)}\frac{1}{r+L}\sqrt{\frac{L}{r}}\,d\theta\,dr + \int_0^{+\infty}\int_{-\pi}^{\pi}g(r,\theta)\,\overline{h(r,\theta)}\frac{1}{r+L}\sqrt{\frac{L}{r}}\,d\theta\,dr = \\ &= \langle f,h\rangle+\langle g,h\rangle.\end{aligned}$$

2. Linearity of the product by a scalar. Let $\alpha\in\mathbb{R}$, then

$$\begin{aligned}\langle \alpha f,g\rangle &= \int_0^{+\infty}\int_{-\pi}^{\pi}\alpha f(r,\theta)\overline{g(r,\theta)}\frac{1}{r+L}\sqrt{\frac{L}{r}}\,d\theta\,dr = \alpha\int_0^{+\infty}\int_{-\pi}^{\pi}f(r,\theta)\overline{g(r,\theta)}\frac{1}{r+L}\sqrt{\frac{L}{r}}\,d\theta\,dr = \\ &= \alpha\langle f,g\rangle.\end{aligned}$$

3. Symmetry in complex space:

$$\langle f,g\rangle = \int_0^{+\infty}\int_{-\pi}^{\pi}f(r,\theta)\overline{g(r,\theta)}\frac{1}{r+L}\sqrt{\frac{L}{r}}\,d\theta\,dr = \overline{\int_0^{+\infty}\int_{-\pi}^{\pi}g(r,\theta)\overline{f(r,\theta)}\frac{1}{r+L}\sqrt{\frac{L}{r}}\,d\theta\,dr} = \overline{\langle g,f\rangle}.$$

4. It must be proved that $\langle f,f\rangle\geq 0$ for every function f and that $\langle f,f\rangle=0$ if and only if $f\equiv 0$. Let us start with the first assertion:

   - $\langle f,f\rangle = \int_0^{+\infty}\int_{-\pi}^{\pi}|f(r,\theta)|^2\frac{1}{r+L}\sqrt{\frac{L}{r}}\,d\theta\,dr\geq 0$ automatically because all the factors are positive or vanish (remember that $L\geq 0$).
   - For the second affirmation, one of the directions is trivial; let us check the opposite one. If $\langle f,f\rangle=0$, as the integrand is always non-negative, the only option is $|f(r,\theta)|^2\frac{1}{r+L}\sqrt{\frac{L}{r}}=0$ at almost every point, what implies that $f(r,\theta)=0$ at almost every point (because $L>0$), and, therefore, $f\equiv 0$.

■

Corollary 2.1. *The set $\mathcal{L}^2\left([0,+\infty)\times[-\pi,\pi],\langle\cdot,\cdot\rangle\right)$ constitutes a Hilbert space with the inner product defined in (2.15).*

Theorem 2.1. *The set of functions $\{\phi_{n,m}(r,\theta,L)\}_{n,m}$ defined in (2.14) constitutes for every $L>0$ an orthogonal basis of the Hilbert space $\mathcal{L}^2\left([0,+\infty)\times[-\pi,\pi],\langle\cdot,\cdot\rangle\right)$, with the inner product defined in (2.15).*

Proof: It is enough to prove that $\langle f, TL_j(r)e^{in\theta}\rangle = 0$, $\forall\ j \in \mathbb{N}, n \in \mathbb{Z}$ implies $f \equiv 0$, being $f \in \mathcal{L}^2([0,+\infty)\times[-\pi,\pi])$. Let us briefly develop this inner product:

$$0 = \langle f, TL_j(r)e^{in\theta}\rangle = \int_0^{+\infty}\int_{-\pi}^{\pi} f(r,\theta)TL_j(r)e^{-in\theta}\frac{1}{r+L}\sqrt{\frac{L}{r}}\,d\theta\,dr. \tag{2.16}$$

Firstly, the integral in r will be calculated separately. Applying the variables changes $y = \dfrac{r-L}{r+L}$ firstly and $y = \cos t$ secondly, it yields:

$$\begin{aligned} I(r) &= \int_0^{+\infty} f(r,\theta)TL_j(r)\frac{1}{r+L}\sqrt{\frac{L}{r}}\,dr = \int_0^{+\infty} f(r,\theta)\cos\left(j\arccos\left(\frac{r-L}{r+L}\right)\right)\frac{1}{r+L}\sqrt{\frac{L}{r}}\,dr = \\ &= \int_{-1}^{1} f\left(L\frac{1+y}{1-y},\theta\right)\cos(j\arccos y)\sqrt{\frac{1}{1-y^2}}\,dy = \int_0^{\pi} f\left(L\frac{1+\cos t}{1-\cos t},\theta\right)\cos(jt)\,dt = \\ &= \int_0^{\pi} f\left(L\frac{1+\cos t}{1-\cos t},\theta\right)\frac{e^{ijt}+e^{-ijt}}{2}\,dt = \\ &= \frac{1}{2}\left[\int_0^{\pi} f\left(L\frac{1+\cos t}{1-\cos t},\theta\right)e^{ijt}\,dt + \int_0^{\pi} f\left(L\frac{1+\cos t}{1-\cos t},\theta\right)e^{-ijt}\,dt\right]. \end{aligned} \tag{2.17}$$

Consider these two integrals separately, although they are conjugates each other since function f is real-valued, and define a new function F:

$$\begin{aligned} F : [-\pi,\pi]\times[-\pi,\pi] &\longrightarrow \mathbb{R} \\ (t,\theta) &\longmapsto F(t,\theta) := f\left(L\frac{1+\cos t}{1-\cos t},\theta\right) \end{aligned} \tag{2.18}$$

Note this function F is 2π-periodic and even with respect to the t coordinate, that is, $F(-t,\theta) = F(t,\theta)$. Applying the variable change $u = -t$ it is easy to see that

$$\int_0^{\pi} F(t,\theta)e^{ijt}\,dt = -\int_0^{-\pi} F(-u,\theta)e^{-iju}\,du = \int_{-\pi}^{0} F(u,\theta)e^{-iju}\,du. \tag{2.19}$$

Therefore

$$I(r) = \frac{1}{2}\left[\int_{-\pi}^{0} F(u,\theta)e^{-iju}\,du + \int_0^{\pi} F(t,\theta)e^{-ijt}\,dt\right] = \frac{1}{2}\int_{-\pi}^{\pi} F(t,\theta)e^{-ijt}\,dt = \pi\hat{F}(j,\theta), \tag{2.20}$$

... considering the Fourier transform in the first coordinate, t. If we define a new function g_j

$$\begin{aligned} g_j : [-\pi,\pi] &\longrightarrow \mathbb{R} \\ \theta &\longmapsto g_j(\theta) := \hat{F}(j,\theta) \end{aligned} \tag{2.21}$$

then, replacing (2.20) and (2.21) into (2.16), it is obtained

$$0 = \int_{-\pi}^{\pi} \pi \hat{F}(j,\theta) e^{-in\theta}\, d\theta = \pi \int_{-\pi}^{\pi} g_j(\theta) e^{-in\theta}\, d\theta = 2\pi^2 \widehat{g_j}(n), \quad \forall j, n. \tag{2.22}$$

Given that Fourier trigonometric system constitutes an orthonormal basis of the Hilbert space $\mathcal{L}^2([-\pi,\pi])$ whose g_j functions belong to for every $j \in \mathbb{N}$, that implies that g_j functions are identically zeros, that is, $g_j \equiv 0$, $\forall j$. Therefore, $\hat{F}(j,\theta) = 0$, $\forall\theta$ and also, by hypothesis, for all j, so $F \equiv 0$ and, consequently, $f \equiv 0$ too.

■

Corollary 2.2. *The set of functions* $\left\{ \frac{1}{C\pi}\, \phi_{n,m}(r,\theta,L) \right\}_{n,m}$, *with* $C = \begin{cases} \sqrt{2}, & \text{if } n = 0 \\ 1, & cc \end{cases}$ *constitutes for every* $L > 0$ *an orthonormal basis of the Hilbert space* $\mathcal{L}^2([0,+\infty) \times [-\pi,\pi], \langle\cdot,\cdot\rangle)$, *with the inner product defined in (2.15).*

Proof: According to the previous theorem, it is enough proving that $\langle \phi_{n,m}, \phi_{n,m} \rangle = (C\pi)^2$, for every $n \in \mathbb{N}, m \in \mathbb{Z}$. Applying the variable changes $y = \dfrac{r-L}{r+L}$ firstly and $y = \cos t$ lately, as in the theorem before, it yields:

$$\begin{aligned} \langle \phi_{n,m}, \phi_{n,m} \rangle &= \int_0^{+\infty} \int_{-\pi}^{\pi} TL_n^2(r) e^{im\theta} e^{-im\theta} \frac{1}{r+L} \sqrt{\frac{L}{r}}\, d\theta dr = 2\pi \int_{-1}^{1} T_n^2(y) \sqrt{\frac{1}{1-y^2}}\, dy = \\ &= 2\pi \int_0^{\pi} \cos^2(nt)\, dt = \begin{cases} 2\pi^2, & \text{if } n = 0 \\ \pi^2, & \text{cc.} \end{cases} . \end{aligned} \tag{2.23}$$

■

With these results, it can be concluded that given any $f \in \mathcal{L}^2([0,+\infty) \times [-\pi,\pi])$, this can be decomposed into

$$f(r,\theta) = \frac{1}{C\pi} \sum_{m=-\infty}^{+\infty} \sum_{n=0}^{+\infty} f_{n,m} TL_n(r) e^{im\theta}, \tag{2.24}$$

where the $f_{n,m}$ will be named the *CHEF coefficients* and can be calculated by means of

$$f_{n,m} = \frac{1}{C\pi} \int_0^{+\infty} \int_{-\pi}^{\pi} f(z,\psi) TL_n(z) \frac{1}{z+L} \sqrt{\frac{L}{z}}\, \mathrm{e}^{-im\psi}\, d\psi dz. \tag{2.25}$$

An azimuthal view of the first CHEF functions is shown in figure 2.6, where both the real and the imaginary components of the basis function with $0 \geq m \geq 10$ and $-4 \geq m \geq 4$ are displayed.

2.3.2. Coefficients decay

A fast decay of the CHEF coefficients is an essential property for practical implementations, since if they do not decrease quickly enough, it will not be possible to efficiently represent images using just

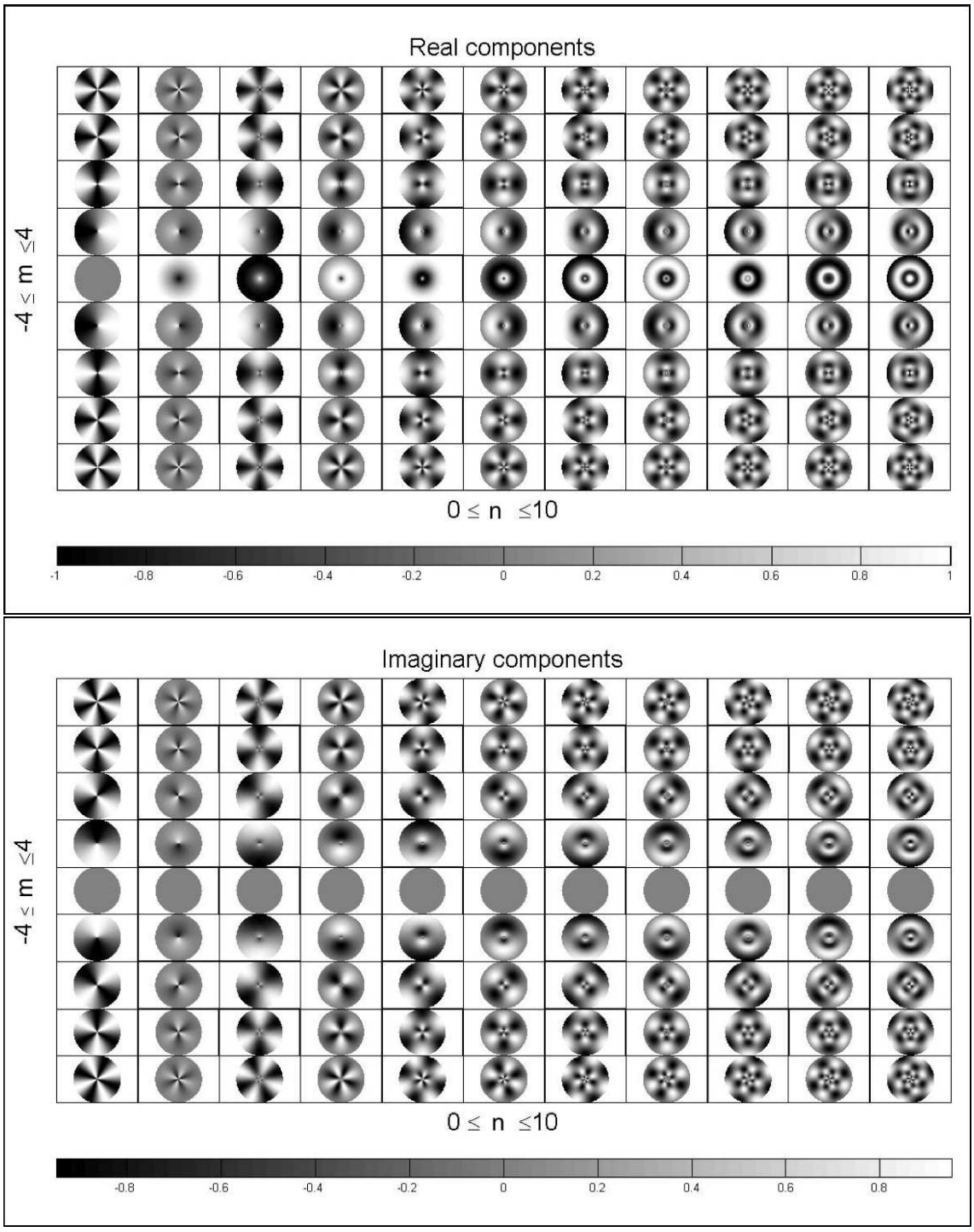

Figure 2.6 Azimuthal view of the first CHEFs functions.

a few coefficients. It is obvious that in a practical implementation infinite sums as (2.24) cannot be afforded. In this subsection, the decay rate of the CHEF coefficients will be calculated by introducing the concept of Chebyshev series and its associated properties. Once the relation between Chebyshev and CHEF series is determined, properties of the former are transferred to the latter, in particular, the coefficients decay rate.

Let us start defining the Chebyshev series of a function and its associate inner product. Given two real-valued functions $f, g \in \mathcal{L}^2([-1,1])$, we define an operation $\langle \cdot, \cdot \rangle_c$ by:

$$\langle f, g \rangle_c = \int_{-1}^{1} (1-x^2)^{-1/2} f(x) g(x)\, dx. \tag{2.26}$$

Proposition 2.2. *The operation defined in (2.26) constitutes an inner product in the $\mathcal{L}^2([-1,1])$ space.*

Proof: Result will be proved in the same way that proposition 2.1. Let f, g and h be three real-valued functions in $\mathcal{L}^2([-1,1])$, then:

1. Linearity of the sum:

$$\begin{aligned}\langle f+g, h \rangle_c &= \int_{-1}^{1} [f(x)+g(x)]\; h(x)(1-x^2)^{-1/2}\, dx = \int_{-1}^{1} f(x)\, h(x)(1-x^2)^{-1/2}\, dx + \\ &+ \int_{-1}^{1} g(x)\, h(x)(1-x^2)^{-1/2}\, dx = \langle f, h \rangle_c + \langle g, h \rangle_c.\end{aligned}$$

2. Linearity of the product by a scalar. Let $\alpha \in \mathbb{R}$, then

$$\langle \alpha f, g \rangle_c = \int_{-1}^{1} \alpha f(x)\, g(x)(1-x^2)^{-1/2}\, dx = \alpha \int_{-1}^{1} f(x)\, g(x)(1-x^2)^{-1/2}\, dx = \alpha \langle f, g \rangle_c.$$

3. Symmetry in complex space:

$$\langle f, g \rangle_c = \int_{-1}^{1} f(x)\, g(x)(1-x^2)^{-1/2}\, dx = \overline{\int_{-1}^{1} g(x)\, f(x)(1-x^2)^{-1/2}\, dx} = \overline{\langle g, f \rangle_c}.$$

4. It must be proved that $\langle f, f \rangle_c \geq 0$ for every function f and $\langle f, f \rangle_c = 0$ if and only if $f \equiv 0$. Let us start with the first assertion:

   - $\langle f, f \rangle_c = \int_{-1}^{1} |f(x)|^2 (1-x^2)^{-1/2}\, dx \geq 0$ automatically because all the factors are positive or vanish.
   - For the second affirmation, one of the directions is trivial; let us check the opposite one. If $\langle f, f \rangle_c = 0$, as the integrand is always non-negative, the only option is $|f(x)|^2 (1-x^2)^{-1/2} = 0$

at almost every point, what implies that $f(x) = 0$ at almost every point and, therefore, $f \equiv 0$.

■

Corollary 2.3. *The set $\mathcal{L}^2([-1,1], \langle\cdot,\cdot\rangle_c)$ constitutes a Hilbert space with the inner product defined in (2.26).*

With this inner product, the *Chebyshev series* of a function $f \in \mathcal{L}^2([-1,1])$ is defined by

$$f(x) \sim \sum_{i=0}^{\infty} f_i^c T_i(x), \tag{2.27}$$

where the *Chebyshev coefficients* f_i^c are obtained by $f_i^c = \dfrac{\langle f, T_i\rangle_c}{\langle T_i, T_i\rangle_c}$. Let us calculate the inner product of two of these Chebyshev polynomials T_i, T_j, with $i, j \in \mathbb{N}$:

$$\begin{aligned}
\langle T_i, T_j\rangle_c &= \int_{-1}^{1} T_i(x)\, T_j(x)(1-x^2)^{-1/2}\, dx = \int_{-1}^{1} \cos(i \cdot \arccos x)\cos(j \cdot \arccos x)(1-x^2)^{-1/2}\, dx = \\
&= \frac{1}{2}\left[\int_{-1}^{1} \cos((i+j)\cdot \arccos x)(1-x^2)^{-1/2}\, dx + \int_{-1}^{1} \cos((i-j)\cdot \arccos x)(1-x^2)^{-1/2}\, dx\right] = \\
&= \frac{1}{2}\left[\int_{0}^{\pi} \cos((i+j)\,t)\, dt + \int_{0}^{\pi} \cos((i-j)\,t)\, dt\right] = \begin{cases} \pi, & \text{if } i = j = 0 \\ \pi/2, & \text{if } i = j \neq 0 \\ 0, & \text{cc} \end{cases}
\end{aligned} \tag{2.28}$$

... this last step being achieved by means of the variables change $x = \cos t$. So finally the Chebyshev coefficients c_i will be given by:

$$f_i^c = \frac{\langle f, T_i\rangle_c}{k}, \qquad \text{with } k = \begin{cases} \pi, & \text{if } i = 0 \\ \pi/2, & \text{if } i \neq 0 \end{cases}. \tag{2.29}$$

Let us then calculate the decay rate of the CHEF coefficients using the fact that a Chebyshev series is a Fourier series with a change of variable, in such a way that the Chebyshev coefficients of a univariate function g are proportional to the Fourier coefficients of the composition $g \circ \cos$:

$$g_n^c = 2\,\widehat{G}[n], \quad \forall\, n \in \mathbb{N}, \quad \text{with } G(t) = g(\cos(t)). \tag{2.30}$$

Proposition 2.3. *Let f be a function of the space $\mathcal{L}^2([-1,1])$. Let us define the function F in the following way:*

$$\begin{array}{rccc} F: & [-\pi,\pi] & \to & \mathbb{R} \\ & t & \mapsto & f(\cos t) \end{array} \tag{2.31}$$

Then, the Fourier coefficients of F are proportional to the Chebyshev coefficients of f, that is,

$$\widehat{F}[n] = \frac{1}{k'}\, f_n^c, \quad \forall\, n \in \mathbb{N} \tag{2.32}$$

where f_n^c *is the n-th coefficient in the Chebyshev series of* f *and* $k' = \begin{cases} k' = 1, & \text{if } n = 0 \\ k' = 2, & \text{if } n > 0 \end{cases}$.

Proof: The function F is 2π-periodic, so its Fourier series can be calculated. Applying the variables changes $y = -t$ and $x = \cos y$, and noting that $F(t) = F(-t)$, it yields:

$$\begin{aligned}
\widehat{F}[n] &= \frac{1}{2\pi}\int_{-\pi}^{\pi} F(t)e^{-int}\,dt = \frac{1}{2\pi}\int_{-\pi}^{0} F(t)e^{-int}\,dt + \frac{1}{2\pi}\int_{0}^{\pi} F(t)e^{-int}\,dt = \\
&= \frac{1}{2\pi}\int_{0}^{\pi} F(y)\left[e^{iny} + e^{-iny}\right]\,dy = \frac{1}{\pi}\int_{0}^{\pi} F(y)\cos(ny)\,dy = \\
&= \frac{1}{\pi}\int_{-1}^{1} f(x)\cos(n\cdot \arccos x)(1-x^2)^{-1/2}\,dx = \frac{1}{\pi}\int_{-1}^{1} f(x)T_n(x)(1-x^2)^{-1/2}\,dx = \frac{1}{k'}\,f_n^c
\end{aligned}$$

■

This result is extremely useful since it allows us to transfer the Fourier series properties to the CHEF one. In addition to this, it is well-known that the Fourier coefficients of a smooth enough function f are bounded, as the following theorem states.

Theorem 2.2. *(Čížek (1986)) Let* f *be a periodic function with an interval of periodicity* $[0, P)$*, continuous with its derivatives up to order* $p-1$*,* $p \geq 1$*, that is,* $f \in \mathcal{C}^{p-1}$*. Let its derivative of order* p *be piecewise continuous in the interval. Then, there exists a constant* $A > 0$ *such that, for Fourier coefficients of the function* f*, we have*

$$\left|\hat{f}[l]\right| \leq \frac{A}{|l|^{p+1}}, \quad \forall\, l \in \mathbb{N}. \tag{2.33}$$

Therefore, using (2.32) and (2.33) it is easy to reach the decay rate of the CHEF coefficients, as it is shown in the following proposition.

Proposition 2.4. *Let* f *be a complex-valued function of the space* $\mathcal{L}^2([0,+\infty]\times[-\pi,\pi])$ *defined in polar coordinates. Let us assume that* f *is continuous in the angular coordinate with its partial derivatives up to order* $p-2$*, and its partial derivative of order* $p-1$ *is piecewise continuous in the interval* $[-\pi,\pi]$*. Let* f *be also piecewise continuous in the azimuthal coordinate (the interval* $[0,+\infty)$*). Then, there exists a constant* $K > 0$ *such that for the CHEF coefficients of* f *it has the following boundary:*

$$|f_{nm}| \leq \frac{C}{|n|\,|m|^{\frac{p+1}{2}}}, \quad \forall\, n, m \in \mathbb{N}. \tag{2.34}$$

Proof: Let us define the function g as

$$\begin{array}{rccc} g: & [-\pi,\pi] & \to & \mathbb{R} \\ & \theta & \mapsto & \displaystyle\int_0^{\infty} f(r,\theta)\, TL_n(r)\, \frac{1}{r+L}\sqrt{\frac{L}{r}}\, dr \end{array} .$$

This function can be extended in a periodic way to fulfil the condition that it is continuous with its derivatives up to order $p-1$, as well as the p-th derivative is piecewise continuous in the periodicity interval $[-\pi,\pi]$. Then, using the theorem 2.2, there exists a non-negative constant N_2' such that

$$|\hat{g}[l]| \leq \frac{N_2'}{|l|^{p+1}}, \quad \forall\, l \in \mathbb{N}.$$

Moreover, a relationship between the CHEF coefficients of f and these Fourier coefficients of g can be established:

$$f_{nm} = \int_{-\pi}^{\pi}\int_0^{\infty} f(r,\theta)\, TL_n(r) e^{-im\theta}\frac{1}{r+L}\sqrt{\frac{L}{r}}\, dr\, d\theta = \int_{-\pi}^{\pi} g(\theta) e^{-im\theta} d\theta = 2\pi\hat{g}[m].$$

Therefore,

$$|f_{nm}| \leq \frac{N_2}{|m|^{p+1}}. \tag{2.35}$$

On another front, let us define a function h as

$$\begin{array}{rccc} h: & (-1,1) & \to & \mathbb{R} \\ & t & \mapsto & \displaystyle\int_{-\pi}^{\pi} f\left(\frac{1+t}{1-t}\, L, \theta\right) e^{-in\theta}\, d\theta \end{array} .$$

Let us consider the function $H = h \circ \cos$. This function can be extended in a periodic way to $\mathbb{R}$ and it is continuous within its interval of periodicity. Its derivative is piecewise continuous in this interval, so we are under the assumption of theorem 2.2 and it can be stated that there exists a constant $N_1' > 0$ such that

$$|\widehat{H}[l]| \leq \frac{N_1'}{l^2}, \quad \forall\, l \in \mathbb{N}.$$

Working in a similar way and applying the variable change $r = \dfrac{1+z}{1-z}\, L$, we reach the following relation between the CHEF coefficients of f and the Chebyshev coefficients of h:

$$f_{nm} = \int_{-1}^{1}\left[\int_{-\pi}^{\pi} f\left(\frac{1+z}{1-z}\, L, \theta\right) e^{-im\theta}\, d\theta\right] T_n(z)(1-z^2)^{-1/2} dz = h_n^c.$$

Using the proposition 2.3, we have that $\widehat{H}[n] = \dfrac{1}{k}\, h_n^c$, being h_n^c the Chebyshev coefficients of the function h, then

$$|f_{nm}| \leq \frac{N_1}{n^2}. \tag{2.36}$$

Finally, using (2.35) and (2.36), it is obtained

$$|f_{nm}|^2 \leq \frac{N_1 N_2}{|m|^{p+1} n^2}.$$

■

2.3.3. Sturm-Liouville equations

The so called *Sturm-Liouville* differential equations fit the following expression

$$\left[r(x)\, y'\right]' + \left[q(x) + \lambda p(x)\right]\, y = 0. \tag{2.37}$$

The solutions $y(x)$ of this ordinary differential equation are called *eigenfunctions* while the valid values λ associated to them receive the name of *eigenvalues*. It can be proved that if the functions p, q and r are real and continuous over an interval $[a, b]$ being $p(x) > 0$ (or $p(x) < 0$),$\forall\, x \in [a, b]$, then all the eigenvalues *lambda* are real and the eigenfunctions y are orthogonal in $[a, b]$ with the weight function p (Courant & Hilbert (1989)).

It is easy to see that the rational Chebyshev functions constitute a family of eigenfunctions of a Sturm-Liouville equations, displaying, therefore, all the properties of the Sturm-Liouville eigenfunctions. This result is immediate since Chebyshev polynomials are also the eigenfunctions of another Sturm-Liouville equation, as the following proposition states.

Proposition 2.5. *(Courant & Hilbert (1989)) Chebyshev polynomials $T_n(x)$ form the solutions set of the following Sturm-Liouville equation:*

$$\left(\sqrt{1-x^2}\, u'\right)' + \frac{\lambda}{\sqrt{1-x^2}}\, u = 0, \tag{2.38}$$

with the boundary conditions that the solution be regular at $x = \pm 1$. The eigenvalue corresponding to the Chebyshev polynomial $T_n(x)$ is $\lambda = n^2$ and these λ and T_n exhaust all the eigenvalues and eigenfunctions.

Corollary 2.4. *Rational Chebyshev functions $\{TL_n(r)\}_n$ form the solutions set of the following Sturm-Liouville equation*

$$\left((r+L)\sqrt{\frac{r}{L}}\, u'\right)' + \frac{\lambda}{r+L}\sqrt{\frac{L}{r}}\, u = 0, \tag{2.39}$$

with the boundary conditions that the solution be regular at $r \in \{-L, 0\}$. The eigenvalue corresponding to the Chebyshev rational function $TL_n(r)$ is $\lambda = n^2$ and these λ and TL_n exhaust all the eigenvalues and eigenfunctions.

2.3.4. Morphological parameters determination

CHEFs can be used not only for modeling purposes but also to calculate morphological parameters of the sources as well as to measure physical properties of them. In order to do so, closed expressions of these parameters (flux, unweighted centroid, quadrupole moments, rms radius and ellipticity) depending on the CHEF coefficients must be found, and the previous evaluation of the generic integral $\int_0^R TL_n(r)\, r^p dr$, $p \geq 1$ will help us to reach simple formulas.

The generic integral $\int_0^R TL_n(r)\, r^p dr$, $p \geq 1$

Let us calculate the generic integral $\int_0^R TL_n(r)\, r^p dr$, with $p \geq 1$, which will be extremely useful for the development of compact analytic expressions of some morphological parameters, as for instance, the flux, the centroid, the rms radius or the ellipticity. Using the fact that $\arccos z = \frac{\pi}{2} + i \ln(iz + \sqrt{1-z^2})$, it yields

$$
\begin{aligned}
I_n^p &= \int_0^R TL_n(r)\, r^p dr = \int_0^R \cos\left(n \cdot \arccos\left(\frac{r-L}{r+L}\right)\right) r^p\, dr = \\
&= \frac{1}{2}\int_0^R \left(e^{in\arccos\left(\frac{r-L}{r+L}\right)} + e^{-in\arccos\left(\frac{r-L}{r+L}\right)}\right) r^p\, dr = \\
&= \frac{1}{2}\int_0^R \left(e^{in\left(\frac{\pi}{2}+i\ln\left(i\frac{r-L}{r+L}+\sqrt{1-\left(\frac{r-L}{r+L}\right)^2}\right)\right)} + e^{-in\left(\frac{\pi}{2}+i\ln\left(i\frac{r-L}{r+L}+\sqrt{1-\left(\frac{r-L}{r+L}\right)^2}\right)\right)}\right) r^p\, dr = \\
&= \frac{1}{2}\, e^{in\pi/2}\int_0^R \left(i\,\frac{r-L}{r+L} + \sqrt{1-\left(\frac{r-L}{r+L}\right)^2}\right)^{-n} r^p\, dr + \\
&\quad + \frac{1}{2}\, e^{-in\pi/2}\int_0^R \left(i\,\frac{r-L}{r+L} + \sqrt{1-\left(\frac{r-L}{r+L}\right)^2}\right)^{n} r^p\, dr = \\
&= \underbrace{\frac{1}{2}\, e^{in\pi/2}\int_0^R \left(i\,\frac{r-L}{r+L} + \frac{2\sqrt{rL}}{r+L}\right)^{-n} r^p\, dr}_{I_{n,1}} + \underbrace{\frac{1}{2}\, e^{-in\pi/2}\int_0^R \left(i\,\frac{r-L}{r+L} + \frac{2\sqrt{rL}}{r+L}\right)^{n} r^p\, dr}_{I_{n,2}}.
\end{aligned}
\tag{2.40}
$$

So integrals $I_{n,1}$ and $I_{n,2}$ must be calculated. For the first one, we will use the Newton binomial theorem:

$$
\begin{aligned}
I_{n,1} &= \int_0^R \left(\frac{i(r-L)+2\sqrt{rL}}{r+L}\right)^{-n} r^p\,dr = \int_0^R \left(i\,\frac{\sqrt{r}-i\sqrt{L}}{\sqrt{r}+i\sqrt{L}}\right)^{-n} r^p\,dr = \\
&= \int_0^R i^{-n}\left(\frac{\sqrt{r}+i\sqrt{L}}{\sqrt{r}-i\sqrt{L}}\right)^{n} r^p\,dr = i^{-n}\int_0^R \sum_{j=0}^{n}\left(\begin{array}{c} n \\ j \end{array}\right)\sqrt{r}^{j}\left(i\sqrt{L}\right)^{n-j}\frac{r^p}{\left(\sqrt{r}-i\sqrt{L}\right)^{n}}\,dr = \\
&= \sum_{j=0}^{n}\left(\begin{array}{c} n \\ j \end{array}\right) i^{-j}\sqrt{L}^{n-j}\int_0^R \frac{r^{p+j/2}}{\left(\sqrt{r}-i\sqrt{L}\right)^{n}}\,dr = \\
&= 2\sum_{j=0}^{n}\left(\begin{array}{c} n \\ j \end{array}\right) i^{-j}\sqrt{L}^{n-j}\int_0^{\sqrt{R}} \frac{z^{2p+j+1}}{\left(z-i\sqrt{L}\right)^{n}}\,dz = \\
&= 2\sum_{j=0}^{n}\left(\begin{array}{c} n \\ j \end{array}\right)(-1)^j i^{n+j} L^{-j/2}\frac{R^{p+j/2+1}}{2p+j+2}\;{}_2F_1\left(n, 2p+j+2, 2p+j+3; \frac{-i\sqrt{R}}{\sqrt{L}}\right)
\end{aligned}
\tag{2.41}
$$

where ${}_2F_1$ denotes the Gauss hypergeometric function and the last step has been carried out just by means of the variable change $z=\sqrt{r}$. This Gauss hypergeometric function ${}_2F_1(a,b,c;z)$ (Abramowitz & Stegun (1970)) was the first hypergeometric function to be studied and is derived from the hypergeometric differential equation

$$z(1-z)y'' + [c-(a+b+1)z]y' - aby = 0. \tag{2.42}$$

An explicit expression of it in power series can be defined using the Pochhammer's symbol $(k)_n = k(k+1)(k+2)\ldots(k+n-1)$:

$${}_2F_1(a,b,c;z) = \sum_{n=0}^{+\infty}\frac{(a)_n(b)_n}{(c)_n}\,\frac{z^n}{n!}, \tag{2.43}$$

or, equivalently, by means of the gamma function Γ, just taking into account that $(k)_n = \dfrac{\Gamma(k+n)}{\Gamma(k)}$:

$${}_2F_1(a,b,c;z) = \sum_{n=0}^{+\infty}\frac{\Gamma(a+n)\Gamma(b+n)}{\Gamma(c+n)}\,\frac{z^n}{n!}. \tag{2.44}$$

On the other hand, the calculation of the second integral $I_{n,2}$ is trivial, just noticing the fact that:

$$I_{n,1} = \int_0^R e^{-f(r)}r^p\,dr = \int_0^R \overline{e^{f(r)}r^p}\,dr = \overline{I_{n,2}} \tag{2.45}$$

Finally, replacing expressions (2.41) and (2.45) into equation (2.40), the final development for the generic integral I_n^p can be obtained:

$$I_n^p = \frac{1}{2}\left[e^{in\pi/2}I_1^n + e^{-in\pi/2}I_2^n\right] = \frac{1}{2}\left[e^{in\pi/2}I_1^n + e^{-in\pi/2}\overline{I_1^n}\right] = Re\left(e^{in\pi/2}I_1^n\right) =$$
$$= 2\sum_{j=0}^{n}\binom{n}{j}(-1)^j L^{-j/2}\frac{R^{p+j/2+1}}{2p+j+2}Re\left(e^{in\pi/2}i^{n+j}\,{}_2F_1\left(n, 2p+j+2, 2p+j+3; \frac{-i\sqrt{R}}{\sqrt{L}}\right)\right) \tag{2.46}$$

Flux

Photometry is in charge of estimating the flux (and, therefore, the magnitude) of the objects in the sky. These measurements can be combined with the inverse-square law to determine the luminosity of an object whose distance is known and vice versa. other physical properties of the galaxies, such as the temperature or the chemical composition of the galaxies can be derived from the flux parameter. But photometry is also extremely useful for many other sources apart from the galaxies, as the variable objects (stars, AGNs and supernovae) to analyze their fluctuations, the extrasolar planets, to detect their existence, and the binary systems, to study their orbital properties and behaviour.

The flux F, which is the total amount of light energy coming from the source and received by the detector, is the simplest parameter that can be calculated using the CHEF coefficients and the generic integral determined in last section:

$$\begin{aligned} F &= \iint_{\mathbb{R}^2} f(x,y)\,dx\,dy = \int_0^{\infty}\int_{-\pi}^{\pi} f\left(r\cos\theta, r\sin\theta\right) r\,dr\,d\theta \approx \\ &\approx \sum_{m=-\infty}^{+\infty}\sum_{n=0}^{+\infty} f_{n,m}\left(\int_0^R TL_n(r) r\,dr\right)\left(\int_{-\pi}^{\pi} \mathrm{e}^{im\theta}\,d\theta\right) = 2\pi\sum_{n=0}^{+\infty} f_{n,0} I_n^1 = \\ &= 4\pi\sum_{n=0}^{+\infty} f_{n,0}\sum_{j=0}^{n}\binom{n}{j}(-1)^j L^{-j/2}\frac{R^{j/2+2}}{j+4}\,Re\left[e^{in\pi/2}i^{n+j}\,{}_2F_1\left(n, j+4, j+5; \frac{-i\sqrt{R}}{\sqrt{L}}\right)\right] \end{aligned} \tag{2.47}$$

In this way, flux is obtained in a very simply way, just through the CHEF coefficients with $m = 0$, which are real.

Unweighted centroid

The unweighted centroid (x_c, y_c) can be also obtained from the CHEF coefficients of the object decomposition:

$$
\begin{aligned}
x_c + iy_c &= \frac{1}{F}\iint_{\mathbb{R}^2}(x+iy)f(x,y)\,dx\,dy = \frac{1}{F}\int_0^{+\infty}\int_{-\pi}^{\pi} f(r\cos\theta, r\sin\theta)r^2(\cos\theta + i\sin\theta)\,d\theta\,dr \approx \\
&\approx \frac{1}{F}\sum_{m=-\infty}^{\infty}\sum_{n=0}^{+\infty} f_{n,m}\left(\int_{-\pi}^{\pi} \mathrm{e}^{im\theta}\cos\theta\,d\theta\right)\left(\int_0^R TL_n(r)r^2\,dr\right) + \\
&+\frac{i}{F}\sum_{m=-\infty}^{\infty}\sum_{n=0}^{+\infty} f_{n,m}\left(\int_{-\pi}^{\pi} \mathrm{e}^{im\theta}\sin\theta\,d\theta\right)\left(\int_0^R TL_n(r)r^2\,dr\right) = \\
&= \frac{2\pi}{F}\sum_{n=0}^{+\infty}\left[(f_{n,-1}+f_{n,1}) + i\,(f_{n,1}-f_{n,-1})\right] I_m^2 = \\
&= \frac{\sum_{n=0}^{+\infty}\left[(f_{n,-1}+f_{n,1}) + i\,(f_{n,1}-f_{n,-1})\right]\sum_{j=0}^{n}\binom{n}{j}(-1)^j L^{-j/2}\frac{R^{j/2+3}}{j+6}\cdot}{\sum_{n=0}^{+\infty} f_{n,0}\sum_{j=0}^{n}\binom{n}{j}(-1)^j L^{-j/2}\frac{R^{j/2+2}}{j+4}\,Re\left[e^{in\pi/2}i^{n+j}\,{}_2F_1\left(n,j+4,j+5;\frac{-i\sqrt{R}}{\sqrt{L}}\right)\right]} \\
&\qquad \frac{\cdot Re\left[e^{in\pi/2}i^{n+j}\,{}_2F_1\left(n,j+6,j+7,\frac{-i\sqrt{R}}{\sqrt{L}}\right)\right]}{\sum_{n=0}^{+\infty} f_{n,0}\sum_{j=0}^{n}\binom{n}{j}(-1)^j L^{-j/2}\frac{R^{j/2+2}}{j+4}\,Re\left[e^{in\pi/2}i^{n+j}\,{}_2F_1\left(n,j+4,j+5;\frac{-i\sqrt{R}}{\sqrt{L}}\right)\right]}
\end{aligned}
\tag{2.48}
$$

Quadrupole moments

In this subsection, unweighted quadrupole moments of the functions representing the astronomical sources will be calculated. These expressions will help us obtain some other physical quantities as, for instance, the ellipticity or the rms radius. Following a similar development than in previous section, the first quadrupole moment F_{11} is obtained:

$$
\begin{aligned}
F_{11} &= \iint_{\mathbb{R}^2} f(x,y)\,x^2\,dx\,dy = \int_0^R\int_{-\pi}^{\pi} f(r\cos\theta, r\sin\theta)\,r^3\,\cos^2\theta\,dr\,d\theta \approx \\
&\approx \sum_{m=-\infty}^{+\infty}\sum_{n=-\infty}^{+\infty} f_{n,m}\left(\int_0^R TL_n(r)\,r^3\,dr\right)\left(\int_{-\pi}^{\pi}\cos^2\theta\;\mathrm{e}^{im\theta}\,d\theta\right) = \\
&= \sum_{n=0}^{+\infty}\left[\pi f_{n,0} + \frac{\pi}{2}\,(f_{n,-2}+f_{n,2})\right] I_n^3 = \\
&= 2\pi\sum_{n=0}^{+\infty}\left[f_{n,0} + \frac{1}{2}\,(f_{n,-2}+f_{n,2})\right]\sum_{j=0}^{n}\binom{n}{j}(-1)^j L^{-j/2}\frac{R^{j/2+4}}{j+8}\cdot \\
&\qquad \cdot Re\left[e^{in\pi/2}i^{n+j}\,{}_2F_1\left(n,j+8,j+9;\frac{-i\sqrt{R}}{\sqrt{L}}\right)\right]
\end{aligned}
\tag{2.49}
$$

and just the $m \in \{-2,0,2\}$ coefficients are needed. When it comes to the F_{22} quadrupole moment, calculations are quite similar:

$$
\begin{aligned}
F_{22} &= \iint_{\mathbb{R}^2} f(x,y)y^2\,dx\,dy = \int_0^{+\infty}\int_{-\pi}^{\pi} f(r\cos\theta, r\sin\theta)r^3\sin^2\theta\,dr\,d\theta \approx \\
&\approx \sum_{m=-\infty}^{+\infty}\sum_{n=0}^{+\infty} f_{n,m}\left(\int_0^R TL_n(r)r^3\,dr\right)\left(\int_{-\pi}^{\pi}\sin^2\theta\,\mathrm{e}^{im\theta}\;d\theta\right) = \\
&= \sum_{n=0}^{+\infty}\left[\pi f_{n,0} - \frac{\pi}{2}\left(f_{n,-2}+f_{n,2}\right)\right] I_n^3 = \\
&= 2\pi\sum_{n=0}^{+\infty}\left[f_{n,0} - \frac{1}{2}\left(f_{n,-2}+f_{n,2}\right)\right]\sum_{j=0}^{n}\binom{n}{j}(-1)^j L^{-j/2}\frac{R^{j/2+4}}{j+8}\cdot \\
&\quad \cdot Re\left[e^{in\pi/2}i^{n+j}\,{}_2F_1\left(n, j+8, j+9; \frac{-i\sqrt{R}}{\sqrt{L}}\right)\right].
\end{aligned}
\tag{2.50}
$$

And, finally, the last quadrupole moment, F_{12} would be:

$$
\begin{aligned}
F_{12} &= \iint_{\mathbb{R}^2} f(x,y)xy\,dx\,dy = \int_0^{+\infty}\int_{-\pi}^{\pi} f(r\cos\theta, r\sin\theta)r^3\cos\theta\sin\theta\,dr\,d\theta \approx \\
&\approx \sum_{m=-\infty}^{+\infty}\sum_{n=0}^{+\infty} f_{n,m}\left(\int_0^R TL_n(r)r^3\,dr\right)\left(\int_{-\pi}^{\pi}\cos\theta\sin\theta\,\mathrm{e}^{im\theta}\;d\theta\right) = \\
&= \sum_{n=0}^{+\infty}\frac{\pi i}{2}(f_{n,2}-f_{n,-2})I_n^3 = \pi i\sum_{n=0}^{+\infty}(f_{n,2}-f_{n,-2})\sum_{j=0}^{n}\binom{n}{j}(-1)^j L^{-j/2}\frac{R^{j/2+4}}{j+8}\cdot \\
&\quad \cdot Re\left[e^{in\pi/2}i^{n+j}\,{}_2F_1\left(n, j+8, j+9; \frac{-i\sqrt{R}}{\sqrt{L}}\right)\right].
\end{aligned}
\tag{2.51}
$$

Next, we will use these unweighted quadrupole moments to derive the rms radius and the ellipticity of the sources.

Rms radius

Since galaxies do not have sharp edges, it is usual to characterize their physical size defining some kind of radius. In particular, the rms radius R is a measure of the size of the object weighted by the mass distribution about its center of mass. It can be expressed by means of the unweighted quadrupole moments F_{11} and F_{22} in the following way:

$$
R^2 = \frac{\iint_{\mathbb{R}^2}(x^2+y^2)f(x,y)\,dx\,dy}{\iint_{\mathbb{R}^2} f(x,y)\,dx\,dy} = \frac{F_{11}+F_{22}}{F}
\tag{2.52}
$$

Thus replacing (2.47), (3.9) and (3.10) into (2.52), the rms radius can be expressed in terms of CHEF coefficients:

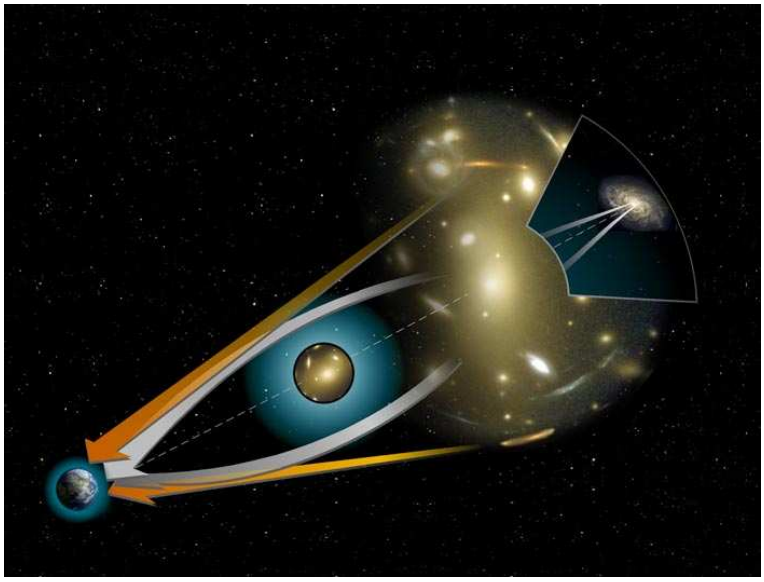

Figure 2.7 Scheme of the light bending due to the action of the gravitational force. Light coming from the source is deviated before arriving to the observer because of the mass of the galaxies encountered through the light path, so objects appear distorted to him. Image from NASA Hubble website, http://hubblesite.org/newscenter/archive/releases, is used with the author's consent.

$$
\begin{aligned}
R^2 &= \frac{2\pi \sum_{n=0}^{\infty} f_{n,0} I_n^3}{2\pi \sum_{n=0}^{\infty} f_{n,0} I_n^1} = \\
&= \frac{\sum_{n=0}^{+\infty} f_{n,0} \sum_{j=0}^{n} \begin{pmatrix} n \\ j \end{pmatrix} (-1)^j L^{-j/2} \frac{R^{j/2+2}}{j+4} Re\left[e^{in\pi/2} i^{n+j} \, {}_2F_1\left(n, j+4, j+5; \frac{-i\sqrt{R}}{\sqrt{L}}\right)\right]}{\sum_{n=0}^{+\infty} f_{n,0} \sum_{j=0}^{n} \begin{pmatrix} n \\ j \end{pmatrix} (-1)^j L^{-j/2} \frac{R^{j/2+4}}{j+8} Re\left[e^{in\pi/2} i^{n+j} \, {}_2F_1\left(n, j+8, j+9; \frac{-i\sqrt{R}}{\sqrt{L}}\right)\right]}.
\end{aligned}
\tag{2.53}
$$

Ellipticity

Gravitational lensing is the process in which light from distant galaxies is bent by the gravity of intervening mass in the Universe as it travels towards us (see figure 2.7) (Bridle et al., 2009). This bending causes the shapes of the galaxies to appear distorted, being this effect higher as the more massive the intervening object is. One of the most important observed distortions is shear, that is, ellipticity of original sources are changed due to the lens effect of the massive source. The precise measurement of this shear (an accuracy less than 1 % is required for cosmic shear) for millions of galaxies becomes quite important not only to quantify this lensing process, but also to relate it statistically to the properties of dark matter distribution at different times in the history of the Universe.

In the same way as rms radius, the unweighted ellipticity of the galaxies can be obtained from the its quadrupole moments and, therefore, from its CHEF coefficients:

$$\begin{aligned}\varepsilon &= \frac{F_{11}-F_{22}+2iF_{12}}{F_{11}+F_{22}} = \frac{\pi \sum\limits_{n=0}^{+\infty} f_{n,-2} I_n^3}{2\pi \sum\limits_{n=0}^{\infty} f_{n,0} I_n^3} = \\ &= \frac{\sum\limits_{n=0}^{+\infty} f_{n,-2} \sum\limits_{j=0}^{n} \binom{n}{j} (-1)^j L^{-j/2} \frac{R^{j/2+4}}{j+8} Re\left[e^{in\pi/2} i^{n+j}\, {}_2F_1\left(n, j+8, j+9; \frac{-i\sqrt{R}}{\sqrt{L}}\right)\right]}{2\sum\limits_{n=0}^{+\infty} f_{n,0} \sum\limits_{j=0}^{n} \binom{n}{j} (-1)^j L^{-j/2} \frac{R^{j/2+4}}{j+8} Re\left[e^{in\pi/2} i^{n+j}\, {}_2F_1\left(n, j+8, j+9; \frac{-i\sqrt{R}}{\sqrt{L}}\right)\right]}.\end{aligned} \tag{2.54}$$

Another definition of the ellipticity, more useful as a shear estimator can be also obtained from the CHEF coefficients using the quadrupole moments (Melchior et al. (2007)):

$$\begin{aligned}\epsilon &= \frac{F_{11}-F_{22}+2iF_{12}}{F_{11}+F_{22}+2(F_{11}F_{22}-F_{12}^2)^{1/2}} = \\ &= \frac{\sum\limits_{n=0}^{+\infty} f_{n,-2} I_n^3}{\sum\limits_{n=0}^{+\infty} f_{n,0}\, I_3^n + \frac{1}{\sqrt{2}} \left[\sum\limits_{l_1,l_2} (-f_{l_1,-2} f_{l_1,2} - f_{l_1,2} f_{l_2,-2} \right.} \\ &\qquad \left. + (f_{l_1,-2} + f_{l_1,2} + f_{l_1,0}) f_{l_2,0} + f_{l_1,0}(f_{l_2,-2} + f_{l_2,2} + f_{l_2,0}))\; I_3^{l_1} I_3^{l_2}\right]^{1/2}}.\end{aligned} \tag{2.55}$$

2.4. Conclusions

Two methods for galaxy modeling are widely-used nowadays: GALFIT and the shapelets. The former is a parametric method, that is, objects are decomposed using an arbitrary number of analytical profiles. With this approach, many morphological types and fine features cannot be fitted, although the advantage is that, for those objects properly fitted, the parameters are easily interpreted. This method is also quite straightforward to implement, but requires plenty of interactivity from the user, what makes it totally inadequate for large surveys processing.

The shapelets belong to the group of non-parametric methods, i.e., they are based on orthogonal bases theoretically capable of modeling any kind of morphology just using a high enough number of components. However, they do not behave specially well with steep sources since they have been built using Gaussians and Hermite polynomials, and those latter not only need a large number of components to model simple profiles (as Sérsic) but also tend to produce artifacts (as ringing effects) when fitting extended sources or highly elliptical ones.

The CHEF bases were developed with the aim of finding and efficient, flexible and automated way to process the huge amount of data coming from large surveys. Built in polar coordinates using

Chebyshev rational functions to expand the radial component and Fourier series for the angular coordinates, this set has been proved to constitute an orthonormal basis of the Hilbert space of finite energy functions $\mathcal{L}^2\left([0,+\infty)\times[-\pi,\pi]\right),\langle\cdot,\cdot\rangle$, with the inner product defined as:

$$\langle f,g\rangle=\int_0^{+\infty}\int_{-\pi}^{\pi}f(r,\theta)\overline{g(r,\theta)}\frac{1}{r+L}\sqrt{\frac{L}{r}}\,d\theta\,dr.$$

In this way, any function f smooth enough can be decomposed as

$$f(r,\theta)=\frac{1}{C\pi}\sum_{m=-\infty}^{+\infty}\sum_{n=0}^{+\infty}f_{n,m}TL_n(r)\,\mathrm{e}^{im\theta},$$

where the $f_{n,m}$ are the CHEF coefficients and can be calculated by means of

$$f_{n,m}=\frac{1}{C\pi}\int_0^{+\infty}\int_{-\pi}^{\pi}f(z,\psi)TL_n(z)\frac{1}{z+L}\sqrt{L}z\,\mathrm{e}^{-im\psi}\;d\psi dz.$$

These bases depend on the scalar parameter L, which will be related to the size of the object being modeled. They have been proved to be compact, due to the CHEF coefficients decay rate:

$$|f_{nm}|\geq\frac{C}{|n|\;|m|^{\frac{p+1}{2}}},\quad\forall n,m\in\mathbb{N},$$

for a certain $p\in\mathbb{N}$, which is related to the smoothness of the function f.

Some other results have been proved, such as the Chebyshev rational functions form the solution set of a certain Sturm-Liouville equation. Analytic formulae to compute some morphological an photometric parameters, like the flux, the centroid, the rms radius, or the ellipticity, just using the CHEF coefficients.

Bibliography

Abramowitz, M; Stegun, A. (1970). Handbook of mathematical functions: with formulas, graphs, and mathematical tables. Dover publications, 1046pp. New York.

Bosch, J. (2010). Galaxy modeling with compound elliptical shapelets. ArXiv:1007.1681.

Boyd, J.P. (2000). Chebyshev and Fourier spectral methods. Dover publications, 611pp. NewYork.

Chang, T.C; Refregier, A. (2002). Shape reconstruction and weak lensing measurement with interferometers: a shapelet approach. ApJ, 570, 447-456.

Čížek, V. (1986). Discrete Fourier Transforms and its applications. Adam Hilger, 141pp, England.

Courant, R; Hilbert, D. (1989) Methods of mathematical physics. John Wiley & Sons, 830pp, USA.

Goldberg, D.M; Bacon, D.J. (2005). Galaxy-galaxy flexion: weak lensing to second order. ApJ, 619, 741-748.

Heymans, K; Van Waerbeke, L; Bacon, D; Bergé, J; Bernstein, G; Bertin, E; Bridle, S; Brown, M.L; Clowe, D; Dahle, H; Erben, T; Gray, M; Hetterscheidt, M; Hoekstra, H; Hudelot, P; Jarvis, M; Kuijken, K; Margoniner, V; Massey, R; Mellier, Y; Nakajima, R; Refregier, A; Rhodes, J; Schrabback, T; Wittman, D. (2006). The Shear Testing Programme - I. Weak lensing analysis of simulated ground-based observations. MNRAS, 368, 1323-1339.

Katnelson, Y. (2004). An introduction to harmonic analysis. Cambridge Mathematical Library, 314pp, UK.

Kelly, B.C; McKay, T.A. (2004). Morphological classification of galaxies by shapelet decomposition in the Sloan Digital Sky Survey. ApJ, 127, 625-645.

Kuijken, K. (2006). Shears from shapelets. A& A, 456, 827-838.

Kuijken, K. (2008). GaaP: PSF- and aperture-matched photometry using shapelets. A& A, 482, 1053-1067.

Mason, J.C; Handscomb, D. (2003). Chebyshev polynomials. Chapman & Hall/CRC, 341pp, USA.

Massey, R; Refregier, A; Bacon, D. (2004). Shapelets "multiple multipole"shear measurement. Impact of gravitational lensing on cosmology, Proceedings of the IAU Symposium, 225.

Massey, R; Refregier, A; Conselice, C.J; Bacon, D.J. (2004). Image simulation with shapelets. MNRAS, 348, 214-226.

Massey, R; Refregier, A. (2005). Polar shapelets. Mon. Not. R. Astron. Soc, 363, 197-210.

Massey, R; Rowe, B; Refregier, A; Bacon, D; Bergé, J. (2007). Weak gravitational shear and flexion with polar shapelets. MNRAS, 380, 229-245.

Melchior, P; Meneghetti, M; Bartelmann, M. (2007). Reliable shapelet image analysis. A& A, 463, 1215-1225.

Melchior, P; Böhnert, A; Lombardi, M; Bartelmann, M. (2010). Limitations on shapelet-based weak-lensing measurements. A& A, 510, A75.

Peng, C.Y; Ho, L.C; Impey, C.D; Rix, H.W. (2002). Detailed structural decomposition of galaxy images. The Astronomical Journal, 124, 266-293.

Peng, C.Y; Ho, L.C; Impey, C.D; Rix, H.W. (2010). Detailed decomposition of galaxy images. II. Beyond axisymmetric models. The Astronomical Journal, 139, 2097-2129.

Press, W.H; Teukolsky, S.A; Vetterling, W.T; Flannery, B.P. (1992). Numerical recipes in C. Cambridge University Press, 994pp, New York.

Refregier, A. (2003). Shapelets - I. A method for image analysis. Mon. Not. R. Astron. Soc, 338, 35-47.

Refregier, A; Bacon, D. (2003). Shapelets: II. A method for weak lensing measurements. MNRAS, 338, 48-56.

3

Practical implementation

All the CHEF mathematical background described in section 2 has been implemented as a Python pipeline,which is described in detail in this chapter. However, many practical hurdles have had to be overcome in the way, not only from the computational point of view but also from the conceptual one, since the theory developed in the last section is based on continuous functions defined on $\mathbb{R}^2$, whereas galaxy objects are discrete matrices. This discretization does away with many of the mathematical properties described before, in particular, the orthonormality. How to deal with this and many other obstacles towards practical application will be explained in the following section.

3.1. CHEF pipeline

The full process of decomposing real image data using the CHEF basis involves the use of several scientific and technical softwares as SExtractor (Bertin & Arnouts (1996)), Python, and IRAF (Doug (1986)). The final Python software package is being applied to the ALHAMBRA survey data (Moles et al., 2008; Benítez et al., 2009) and the CLASH data (Postman et al, 2011). As it will be seen, the only inputs for this pipeline are the image to be analyzed and the maximum number of coefficients allowed for the decomposition. The full pipeline is briefly described below step by step, and the most problematic issues will be explained in more detail in the following subsections. Note that in this process outlined below we do not deal yet separately with the PSFs, fitting directly the objects without attempting any deconvolution.

1. *Image analysis with SExtractor and source filtering.* The sources present in the image are detected using SExtractor, and an appropriate input file. Depending on the images to analyze, some parameters must be appropriately set on this input .sex file, such as the detect threshold, the deblend nthreshold (which indicates the level of separation between too close sources), or the background parameters (extremely important to perform an adequate sky estimation). The output values provided by SExtractor, stored in an ASCII catalog, are the following: centroid, right ascension and declination, coordinates of the brightest pixel, coordinates of the lower left and upper right corners of the tightest frame containing the source, minor and major axes,

position angle, stellarity parameter, full width half maximum assuming a Gaussian core, fraction of light radii, magnitude, the peak surface brightness above the background, the isophotal area about the analysis threshold, the flux measured using different apertures as well as their associate errors, and the running number. These 24 parameters will be used in the following processing. An example of both a configuration parameters file and an output catalog can be observed in figures 3.1 and 3.2 respectively, by way of illustration.

In order to eliminate spurious detections, galaxies too near to the edges or too faint in comparison with the brightest object in the image are masked. Stars are also removed, according to the SExtractor stellarity parameter previously mentioned (considering that a value greater than 0.85 for a very bright object, i.e., with magnitude less than 0.9, usually identifies the object as a point source).

2. Extraction of the frame. The frame containing the object to analyze must be large enough to enclose all the light flux coming from the source, but small enough to avoid many other galaxies to enter into it and contaminate the resulting model. Therefore, frame must be chosen proportionally to the size of the source, and it is selected to have a side four times greater than the half light radius r_{hl} determined by SExtractor:

$$size_{max} = 4 \times r_{hl} \tag{3.1}$$

This parameter has happened to be much more stable than the usual FWHM to estimate the "extension" of the galaxies. In practically all cases this frame fully includes the galaxy flux.

3. Masking the neighbour objects out. Objects inside the frame apart from the main one which are detected by SExtractor are masked out using the segmentation map also provided by this software. In this way, the CHEF basis will only try to fit the principal object and the resulting model will be less affected by the presence of these fainter objects.

4. Determination of the maximum number of coefficients. The number of coefficients N and M to calculate, both for the Chebyshev polynomials and the Fourier series, will determine the accuracy of the result. The maximum order where these parameters are allowed to range to are the only inputs of the algorithm (apart from the image to analyze, of course), and their optimal values depend on the morphology and size of the object. However, this optimization will be performed automatically by the code, as it will be seen later. As a general rule, the larger the number of pixels in the image to be fit, the larger the required number of coefficients. For instance, for two images of the same galaxy, the one with a smaller pixel scale will require more coefficients (assuming of course that the S/N is similar in both cases). We set N^{max}, M^{max} and choose this value according to the image size. For instance, for a regular image of 60×60 pixels the usual choice is $N^{max} = M^{max} = 7$, whereas for more extended sources of about 120×120 pixels we set $N^{max} = M^{max} = 10$.In the case of huge images as clusters of galaxies or sources with a great amount of subestructure on it, a maximum number of $N^{max} = M^{max} = 15$ has been tried, with very good results although the calculations take long time.

```
# SExtractor configuration file
# For use with "KECK" images wregister'ed to ACS coordinates
# (*) indicates parameters which can be omitted from this config file.

#-------------------------------- Catalog ----------------------------------

CATALOG_NAME    temp.cat
CATALOG_TYPE    ASCII_HEAD          # "ASCII_HEAD","ASCII","FITS_1.0" or "FITS_LDAC"
PARAMETERS_NAME shex.param

#-------------------------------- Extraction -------------------------------

DETECT_TYPE     CCD             # "CCD" or "PHOTO" (*)
DETECT_MINAREA  15.             # minimum number of pixels above threshold
DETECT_THRESH   1.5             # <sigmas> or <threshold>,<ZP> in mag.arcsec-2
ANALYSIS_THRESH 1.5             # <sigmas> or <threshold>,<ZP> in mag.arcsec-2

FILTER          Y               # apply filter for detection ("Y" or "N")?
FILTER_NAME     tophat_3.0_3x3.conv    # name of the file containing the filter

DEBLEND_NTHRESH 64              # Number of deblending sub-thresholds
DEBLEND_MINCONT 0.0002          # Minimum contrast parameter for deblending

CLEAN           Y               # Clean spurious detections? (Y or N)?
CLEAN_PARAM     1.              # Cleaning efficiency

MASK_TYPE       CORRECT         # Blank detected objects (Y or N)?

#-------------------------------- Photometry -------------------------------

PHOT_APERTURES  25.0            # MAG_APER aperture diameter(s) in pixels (5.6)
PHOT_AUTOPARAMS 2.5, 5.0        # MAG_AUTO parameters: <Kron_fact>,<min_radius>

SATUR_LEVEL     50000.0         # level (in ADUs) at which arises saturation

MAG_ZEROPOINT   25.             # magnitude zero-point
MAG_GAMMA       4.0             # gamma of emulsion (for photographic scans)
GAIN            4.              # detector gain in e-/ADU.
PIXEL_SCALE     0.221           # size of pixel in arcsec (0=use FITS WCS info).

#------------------------- Star/Galaxy Separation ---------------------------

SEEING_FWHM     0.25            # stellar FWHM in arcsec
STARNNW_NAME    default.nnw     # Neural-Network_Weight table filename

#-------------------------------- Background -------------------------------

BACK_SIZE       16              # Background mesh: <size> or <width>,<height>
BACK_FILTERSIZE 1               # Background filter: <size> or <width>,<height>

BACKPHOTO_TYPE  LOCAL           # can be "GLOBAL" or "LOCAL" (*)
BACKPHOTO_THICK 24              # thickness of the background LOCAL annulus (*)

#---------------------- Memory (change with caution!) -----------------------

MEMORY_OBJSTACK 15000           # number of objects in stack
MEMORY_PIXSTACK 2600000         # number of pixels in stack
MEMORY_BUFSIZE  4600            # number of lines in buffer

#-------------------------------- Check Image ------------------------------

#CHECKIMAGE_TYPE APERTURES
#CHECKIMAGE_NAME ap_ACS1.fits

#-------------------------------- Flag -------------------------------------

#FLAG_TYPE      AND             # COMBINATION OF INTERNAL + EXTERNAL FLAGS
#FLAG_IMAGE     f04p01_1_acs_flag.fits  # FLAG IMAGE (INTEGER)

#-------------------------------- Weight -----------------------------------

WEIGHT_TYPE    BACKGROUND       # Since there is no background
#WEIGHT_IMAGE  f04p01_deep_1.swpweight.fits


#-------------------------------- ASSOC ------------------------------------

#ASSOC_NAME      f02p01_deep_1.dat
#ASSOC_PARAMS    2,3
#ASSOC_TYPE      NEAREST
#ASSOCSELEC_TYPE MATCHED
#ASSOC_RADIUS    2
#ASSOC_DATA      0
```

Figure 3.1 Example of configuration parameters file for SExtractor.

```
#   1 X_IMAGE         Object position along x                      [pixel]
#   2 Y_IMAGE         Object position along y                      [pixel]
#   3 ALPHA_J2000     Right ascension of barycenter (J2000)        [deg]
#   4 DELTA_J2000     Declination of barycenter (J2000)            [deg]
#   5 XPEAK_IMAGE     x-coordinate of the brightest pixel          [pixel]
#   6 YPEAK_IMAGE     y-coordinate of the brightest pixel          [pixel]
#   7 XMIN_IMAGE      Minimum x-coordinate among detected pixels   [pixel]
#   8 YMIN_IMAGE      Minimum y-coordinate among detected pixels   [pixel]
#   9 XMAX_IMAGE      Maximum x-coordinate among detected pixels   [pixel]
#  10 YMAX_IMAGE      Maximum y-coordinate among detected pixels   [pixel]
#  11 A_IMAGE         Profile RMS along major axis                 [pixel]
#  12 B_IMAGE         Profile RMS along minor axis                 [pixel]
#  13 THETA_IMAGE     Position angle (CCW/x)                       [deg]
#  14 CLASS_STAR      S/G classifier output
#  15 FWHM_IMAGE      FWHM assuming a gaussian core                [pixel]
#  16 FLUX_RADIUS     Fraction-of-light radii                      [pixel]
#  17 MAG_APER        Fixed aperture magnitude vector              [mag]
#  18 MU_MAX          Peak surface brightness above background     [mag * arcsec**(-2)]
#  19 FLUX_AUTO       Flux within a Kron-like elliptical aperture  [count]
#  20 ISOAREA_IMAGE   Isophotal area above Analysis threshold      [pixel**2]
#  21 FLUX_ISO        Isophotal flux                               [count]
#  22 FLUXERR_ISO     RMS error for isophotal flux                 [count]
#  23 NUMBER          Running object number
#  24 FLUXERR_AUTO    RMS error for AUTO flux                      [count]
   348.362    379.622   0.0000000  +0.0000000        348        379        230        283        473        553    23.909    22.986 -83.3
0.03     0.00     22.577   8.4245   5.7033 3.438561e+07      6044 3.320912e+07     7909.693          1     8791.154
   397.301     33.726   0.0000000  +0.0000000        398         33        375         30        411         48     5.172     2.479  -2.3
0.82     0.00      3.122  12.2849   7.1981     306211.1         44     296375     1050.5           2     1479.422
   236.198     16.595   0.0000000  +0.0000000        236         17        235         16        237         17     0.755     0.450 -18.8
0.35     0.00      1.575  17.2788  11.5585     3915.864          0     1583.58     135.163          3     418.7807
   582.084    686.310   0.0000000  +0.0000000        594        677        508        672        598        747    34.045     1.456 -38.5
0.01     0.00     15.098  13.3367  10.1076     272178.2         39     216745.9     1265.072          4     2906.438
   498.357    750.743   0.0000000  +0.0000000        498        751        493        742        513        754     3.555     2.016 -20.3
0.92     0.00      2.024  12.0369   6.9605     357813.2         58     347369.2     815.5587          5     1002.462
   492.880    743.762   0.0000000  +0.0000000        493        743        484        734        503        752     3.849     2.423 -57.3
0.79     0.00      3.538  12.0402   7.8709     349933.6         72     328881.1     934.5507          6     1161.193
```

Figure 3.2 Example of output catalog file from SExtractor.

5. Selection of the center and the scale size L. The determination of these two values is crucial to establish the origin of the grid where the CHEF functions will be evaluated, as well as the characteristic scale of the basis, which is obviously related to the size of the object (see sections 3.2.4 and 3.2.5). The centroid provided by SExtractor is the one selected to set the grid, and the scale is obtained from the half-light radius. However, a version of the code allows the user to find the optimal scale size, in case more accuracy is required. This is not the option by default, since the stability of the CHEF bases leads to highly precise results even in the case of using a suboptimal value, and the computational time decreases. In addition, we obtained an empirical law relating the FWHM of the sources and the optimal scale values for the galaxies in the UDF.

6. Evaluation of the basis. The CHEF basis corresponding to the maximum N^{max} and M^{max} introduced in step 4, and with the origin and scale size determined in step 5, is evaluated. This discrete version of the CHEF basis is no longer either orthogonal or even a basis (see section 3.2.2), so the Modified Gram-Schmidt algorithm is applied. It is remarkable to say that, thanks to the exceptional stability and robustness of CHEF bases again, they can be precalculated (for different values of the scale parameter L), in such a way that the software just looks for the one with the nearest value of L stored in the database of functions. With this approach, the database must be loaded just at the beginning of the analysis and the code is much faster. For large data volumes this results in a speed up of more than a factor of 3.

7. Determination of the optimal number of coefficients N and M. The best values for these parameters are calculated iteratively by applying a chi squared test, as it will be explained in section 3.2.6. The basis functions corresponding to these concrete values of N and M are extracted as

a submatrix from the whole set of functions calculated for the maximum number of coefficients allowed (see step 6), so a new evaluation is not needed and a great amount of computational time is saved.

8. Computation of the CHEF coefficients and evaluation of the model. The $n_{coeffs} = (N+1)\cdot(2M+1)$ coefficients of the CHEF expansion are computed by means of a discrete and real version of the inner product 2.15, which coincides with the usual inner product defined in $\mathbb{R}^{p_1 \times p_2}$, where $p_1 \times p_2$ is the size in pixels of the frame extracted in step 2. The model of the galaxy is then computed as a linear combination of the discretized and orthonormalized functions from step 6 (see sections 3.2.2 and 3.2.3), weighted by these CHEF coefficients.

9. Iteration of the algorithm. If necessary, steps from 2 to 8 are repeated for each one of the objects present in the image and which have been detected by SExtractor in step 1.

3.2. From theory to practice

As it was mentioned previously, the practical implementation of the algorithm had to overcome some practical hurdles, specially due to the fact that the whole mathematical background where CHEF bases rely on is constructed from the continuous point of view and for the complex space. Discretization inevitably entailed some problems and a few adjustments had to be made to deal with them. In addition to this, finding the best values for some parameters was not a trivial task, and involved the search for appropriate optimization algorithms. These issues, together with the best way we have found to solve them, are described in this section.

3.2.1. From the complex to the real world

The exponential in (2.14) makes CHEF bases complex, as well as the derived CHEF coefficients and the models they produce. From the mathematical point of view, the complex formulation of the CHEFs is much more compact and elegant. However, although CHEFs constitute bases of the Hilbert space $\mathcal{L}^2([0,+\infty)\times[-\pi,\pi])$ of complex-valued functions, galaxy data imaging belongs to real world, and the imaginary results of the bases become meaningless. Nevertheless, the real components of the CHEF models are also influenced by the imaginary part of the bases, so removing the latter is not a solution. A deeper look into the bases reveals that the parts of the components related to the crossed products are irrelevant, i.e. those involving the real part by the imaginary one and vice versa, since these ones are the responsible for the imaginary outputs. Therefore, and despite losing some of the original beauty of the basis, we decided to introduce a "real" version of the basis, which is faster and involves fewer calculations. Real and imaginary components of the original bases were split into different element of the new bases. As they all belong to real space, operations between them were reduced to the usual ones in $\mathbb{R}^2$, what meant a decrease of the computational time by half. Therefore, the new real bases become:

$$\{\phi_{n,m}(r,\theta;L)\}_{n,m} = \left\{\frac{1}{C\pi} TL_n(r)W_m(\theta)\right\}_{n,m}, \quad n,m \in \mathbb{N} \tag{3.2}$$

where $C = \begin{cases} \sqrt{2}, & \text{if } n = 0 \\ 1, & \text{cc} \end{cases}$, TL_n is the Chebyshev rational function of order n and $W_m(\theta)$ represents both the trigonometric functions $\sin(m\theta)$ and $\cos(m\theta)$. Taking into account the development displayed in section 2, it can be trivially concluded that this set of functions constitutes an orthonormal basis of the Hilbert space $\mathcal{L}^2([0,+\infty) \times [-\pi,\pi])$ of real-valued functions, where the inner product is now defined as follows:

$$\langle f, g \rangle = \int_0^{\infty} \int_{-\pi}^{\pi} f(r,\theta)\, g(r,\theta) \frac{1}{r+L} \sqrt{\frac{L}{r}}\, d\theta\, dr. \tag{3.3}$$

With this new approach, any smooth enough function can be decomposed into:

$$\begin{aligned} f(r,\theta) &= \frac{1}{C\pi} \sum_{m=0}^{+\infty} \sum_{n=0}^{+\infty} f_{n,m}\, TL_n(r)\, W_m(\theta) = \\ &= \frac{1}{C\pi} \sum_{m=0}^{+\infty} \sum_{n=0}^{+\infty} \left[f^c_{n,m}\, TL_n(r) \cos(m\theta) + f^s_{n,m}\, TL_n(r) \sin(m\theta) \right] \end{aligned} \tag{3.4}$$

where the new coefficients $f^c_{n,m}$ and $f^s_{n,m}$ are calculated in the usual way, with the inner product defined in 3.3:

$$\begin{aligned} f^c_{n,m} &= \langle f(r,\theta), \cos(m\theta) \rangle = \frac{C}{2\pi^2} \int_{-\pi}^{\pi} \int_{0}^{+\infty} f(z,\phi)\, TL_n(z)\, \frac{1}{z+L} \sqrt{\frac{L}{z}} \cos(m\phi)\, dz\, d\phi \\ f^s_{n,m} &= \langle f(r,\theta), \cos(m\theta) \rangle = \frac{C}{2\pi^2} \int_{-\pi}^{\pi} \int_{0}^{+\infty} f(z,\phi)\, TL_n(z)\, \frac{1}{z+L} \sqrt{\frac{L}{z}} \sin(m\phi)\, dz\, d\phi. \end{aligned} \tag{3.5}$$

Please note that now m-sums in (3.4) do not include negative values of m, since basis functions with $m < 0$ coincide with their corresponding positive element in the basis (up to the sign):

$$\phi_{n,m}(r,\theta;L) = \frac{1}{C\pi} TL_n(r) W_m(\theta) = \frac{k}{C\pi} TL_n(r) W_{-m}(\theta) = k\, \phi_{n,-m}(r,\theta;L), \tag{3.6}$$

where $k = \begin{cases} 1, & \text{if } W_m(\theta) = \cos(m\theta) \\ -1, & \text{if } W_m(\theta) = \sin(m\theta) \end{cases}$. So the new basis has half of the elements of the complex original basis, what obviously contributes to a faster final algorithm.

In addition, all the properties displayed for CHEF complex basis in section 2.3 keep on being satisfied by the real version of it, as can be trivially proven. Special interest must be devoted to the translation of expressions for morphological shape measurement into these new bases. As the process to arrive to them slightly differs from the complex case, the whole process and the formulas is shown:

- Flux:

$$\begin{aligned} F &= \iint\limits_{\mathbb{R}^2} f(x,y)\,dx\,dy = \int\limits_0^{\infty}\int\limits_{-\pi}^{\pi} f\left(r\cos\theta, r\sin\theta\right) r\,dr\,d\theta \approx \\ &\approx \sum_{m=0}^{+\infty}\sum_{n=0}^{+\infty} f^s_{n,m}\left(\int\limits_0^R TL_n(r) r\,dr\right)\left(\int\limits_{-\pi}^{\pi}\sin(m\theta)\,d\theta\right) + \\ &\quad + \sum_{m=0}^{+\infty}\sum_{n=0}^{+\infty} f^c_{n,m}\left(\int\limits_0^R TL_n(r) r\,dr\right)\left(\int\limits_{-\pi}^{\pi}\cos(m\theta)\,d\theta\right) = 2\pi\sum_{n=0}^{+\infty} f^c_{n,0} I^1_n = \\ &= 4\pi\sum_{n=0}^{+\infty} f^c_{n,0}\sum_{j=0}^{n}\binom{n}{j}(-1)^j L^{-j/2}\frac{R^{j/2+2}}{j+4}\,Re\left[e^{in\pi/2} i^{n+j}\,{}_2F_1\left(n, j+4, j+5; \frac{-i\sqrt{R}}{\sqrt{L}}\right)\right] \end{aligned} \tag{3.7}$$

- Unweighted centroid:

$$\begin{aligned} &x_c + iy_c = \frac{1}{F}\iint\limits_{\mathbb{R}^2}(x+iy) f(x,y)\,dx\,dy = \frac{1}{F}\int\limits_0^{+\infty}\int\limits_{-\pi}^{\pi} f(r\cos\theta, r\sin\theta) r^2(\cos\theta + i\sin\theta)\,d\theta\,dr \approx \\ &\approx \frac{1}{F}\sum_{m=0}^{\infty}\sum_{n=0}^{+\infty}\left(f^c_{n,m}\int\limits_{-pi}^{pi}\cos(m\theta)\cos\theta\,d\theta + f^s_{n,m}\int\limits_{-pi}^{pi}\sin(m\theta)\cos\theta\,d\theta\right)\left(\int\limits_0^R TL_n(r) r^2\,dr\right) + \\ &+\frac{i}{F}\sum_{m=0}^{\infty}\sum_{n=0}^{+\infty}\left(f^c_{n,m}\int\limits_{-pi}^{pi}\cos(m\theta)\sin\theta\,d\theta + f^s_{n,m}\int\limits_{-pi}^{pi}\sin(m\theta)\sin\theta\,d\theta\right)\left(\int\limits_0^R TL_n(r) r^2\,dr\right) = \\ &= \frac{2\pi}{F}\sum_{n=0}^{+\infty}\left[\left(f^c_{n,-1} + f^c_{n,1}\right) + i\left(f^s_{n,1} - f^s_{n,-1}\right)\right] I^2_m = \\ &= \frac{\sum\limits_{n=0}^{+\infty}\left[\left(f^c_{n,-1} + f^c_{n,1}\right) + i\left(f^s_{n,1} - f^s_{n,-1}\right)\right]\sum\limits_{j=0}^{n}\binom{n}{j}(-1)^j L^{-j/2}\frac{R^{j/2+3}}{j+6}\cdot}{\sum\limits_{n=0}^{+\infty} f^c_{n,0}\sum\limits_{j=0}^{n}\binom{n}{j}(-1)^j L^{-j/2}\frac{R^{j/2+2}}{j+4}\,Re\left[e^{in\pi/2} i^{n+j}\,{}_2F_1\left(n, j+4, j+5; \frac{-i\sqrt{R}}{\sqrt{L}}\right)\right]} \\ &\qquad \cdot Re\left[e^{in\pi/2} i^{n+j}\,{}_2F_1\left(n, j+6, j+7, \frac{-i\sqrt{R}}{\sqrt{L}}\right)\right] \\ &\frac{}{\sum\limits_{n=0}^{+\infty} f^c_{n,0}\sum\limits_{j=0}^{n}\binom{n}{j}(-1)^j L^{-j/2}\frac{R^{j/2+2}}{j+4}\,Re\left[e^{in\pi/2} i^{n+j}\,{}_2F_1\left(n, j+4, j+5; \frac{-i\sqrt{R}}{\sqrt{L}}\right)\right]} \end{aligned} \tag{3.8}$$

- Quadrupole moments:

1.

$$\begin{aligned}
F_{11} &= \iint\limits_{\mathbb{R}^2} f(x,y)\,x^2\,dx\,dy = \int\limits_0^R \int\limits_{-\pi}^{\pi} f(r\cos\theta, r\sin\theta)\,r^3\,\cos^2\theta\,dr\,d\theta \approx \\
&\approx \sum_{m=0}^{+\infty}\sum_{n=0}^{+\infty}\left(\int\limits_0^R TL_n(r)\,r^3\,dr\right)\left(f^c_{n,m}\int\limits_{-\pi}^{\pi}\cos^2\theta\,\cos(m\theta) + f^s_{n,m}\int\limits_{-\pi}^{\pi}\cos^2\theta\,\sin(m\theta)\right) = \\
&= \sum_{n=0}^{+\infty}\left(\pi f^c_{n,0} + \frac{\pi}{2}f^c_{n,2}\right) I_n^3 = \\
&= 2\pi\sum_{n=0}^{+\infty}\left(f^c_{n,0} + \frac{1}{2}f^c_{n,2}\right)\sum_{j=0}^{n}\binom{n}{j}(-1)^j L^{-j/2}\frac{R^{j/2+4}}{j+8}\cdot \\
&\quad \cdot Re\left[e^{in\pi/2}i^{n+j}\,{}_2F_1\left(n, j+8, j+9; \frac{-i\sqrt{R}}{\sqrt{L}}\right)\right].
\end{aligned} \tag{3.9}$$

2.

$$\begin{aligned}
F_{22} &= \iint\limits_{\mathbb{R}^2} f(x,y)y^2\,dx\,dy = \int\limits_0^{+\infty} \int\limits_{-\pi}^{\pi} f(r\cos\theta, r\sin\theta)r^3\sin^2\theta\,dr\,d\theta \approx \\
&\approx \sum_{m=0}^{+\infty}\sum_{n=0}^{+\infty}\left(\int\limits_0^R TL_n(r)r^3\,dr\right)\left(f^c_{n,m}\int\limits_{-\pi}^{\pi}\sin^2\theta\cos(m\theta)\,d\theta + f^s_{n,m}\int\limits_{-\pi}^{\pi}\sin^2\theta\sin(m\theta)\,d\theta\right) = \\
&= \sum_{n=0}^{+\infty}\left(\pi f^c_{n,0} - \frac{\pi}{2}f^c_{n,2}\right) I_n^3 = \\
&= 2\pi\sum_{n=0}^{+\infty}\left(f^c_{n,0} - \frac{1}{2}f^c_{n,2}\right)\sum_{j=0}^{n}\binom{n}{j}(-1)^j L^{-j/2}\frac{R^{j/2+4}}{j+8}\cdot \\
&\quad \cdot Re\left[e^{in\pi/2}i^{n+j}\,{}_2F_1\left(n, j+8, j+9; \frac{-i\sqrt{R}}{\sqrt{L}}\right)\right].
\end{aligned} \tag{3.10}$$

3.

$$\begin{aligned}
F_{12} &= \iint\limits_{\mathbb{R}^2} f(x,y)xy\,dx\,dy = \int\limits_0^{+\infty} \int\limits_{-\pi}^{\pi} f(r\cos\theta, r\sin\theta)r^3\cos\theta\sin\theta\,dr\,d\theta \approx \\
&\approx \sum_{m=0}^{+\infty}\sum_{n=0}^{+\infty}\left(\int\limits_0^R TL_n(r)r^3\,dr\right)\left(f^c_{n,m}\int\limits_{-\pi}^{\pi}\cos\theta\sin\theta\cos(m\theta)\,d\theta + f^s_{n,m}\int\limits_{-\pi}^{\pi}\cos\theta\sin\theta\sin(m\theta)\,d\theta\right) = \\
&= \sum_{n=0}^{+\infty}\frac{\pi}{2}f^s_{n,2}I_n^3 = \pi\sum_{n=0}^{+\infty}f^s_{n,2}\sum_{j=0}^{n}\binom{n}{j}(-1)^j L^{-j/2}\frac{R^{j/2+4}}{j+8}\cdot \\
&\quad \cdot Re\left[e^{in\pi/2}i^{n+j}\,{}_2F_1\left(n, j+8, j+9; \frac{-i\sqrt{R}}{\sqrt{L}}\right)\right].
\end{aligned} \tag{3.11}$$

- rms radius:

$$
\begin{aligned}
R^2 &= \frac{2\pi \sum_{n=0}^{\infty} f^c_{n,0} I^3_n}{2\pi \sum_{n=0}^{\infty} f^c_{n,0} I^1_n} = \\
&= \frac{\sum_{n=0}^{+\infty} f^c_{n,0} \sum_{j=0}^{n} \left(\begin{array}{c} n \\ j \end{array} \right) (-1)^j L^{-j/2} \frac{R^{j/2+2}}{j+4} Re\left[e^{in\pi/2} i^{n+j} \, {}_2F_1\left(n, j+4, j+5; \frac{-i\sqrt{R}}{\sqrt{L}} \right) \right]}{\sum_{n=0}^{+\infty} f^c_{n,0} \sum_{j=0}^{n} \left(\begin{array}{c} n \\ j \end{array} \right) (-1)^j L^{-j/2} \frac{R^{j/2+4}}{j+8} Re\left[e^{in\pi/2} i^{n+j} \, {}_2F_1\left(n, j+8, j+9; \frac{-i\sqrt{R}}{\sqrt{L}} \right) \right]}.
\end{aligned}
\tag{3.12}
$$

- Ellipticity (first definition):

$$
\begin{aligned}
\varepsilon &= \frac{F_{11} - F_{22} + 2iF_{12}}{F_{11} + F_{22}} = \frac{\pi \sum_{n=0}^{+\infty} \left(f^c_{n,2} + i f^s_{n,2} \right) I^3_n}{2\pi \sum_{n=0}^{\infty} f^c_{n,0} I^3_n} = \\
&= \frac{\sum_{n=0}^{+\infty} \left(f^c_{n,2} + i f^s_{n,2} \right) \sum_{j=0}^{n} \left(\begin{array}{c} n \\ j \end{array} \right) (-1)^j L^{-j/2} \frac{R^{j/2+4}}{j+8} Re\left[e^{in\pi/2} i^{n+j} \, {}_2F_1\left(n, j+8, j+9; \frac{-i\sqrt{R}}{\sqrt{L}} \right) \right]}{2 \sum_{n=0}^{+\infty} f^c_{n,0} \sum_{j=0}^{n} \left(\begin{array}{c} n \\ j \end{array} \right) (-1)^j L^{-j/2} \frac{R^{j/2+4}}{j+8} Re\left[e^{in\pi/2} i^{n+j} \, {}_2F_1\left(n, j+8, j+9; \frac{-i\sqrt{R}}{\sqrt{L}} \right) \right]}.
\end{aligned}
\tag{3.13}
$$

- Ellipticity (second definition):

$$
\begin{aligned}
\epsilon &= \frac{F_{11} - F_{22} + 2iF_{12}}{F_{11} + F_{22} + 2(F_{11}F_{22} - F^2_{12})^{1/2}} = \\
&= \frac{\sum_{n=0}^{+\infty} \left(f^c_{n,2} + f^s_{n,2} \right) I^n_3}{2 \sum_{n=0}^{+\infty} f^c_{n,0} I^n_3 + \left[\sum_{l_1,l_2} \left[\left(f^c_{l_1,0} + \frac{1}{2}(f^c_{l_1,-2} + f^c_{l_1,2}) \right) \left(f^c_{l_2,0} - \frac{1}{2}(f^c_{l_2,-2} + f^c_{l_2,2}) \right) - \right. \right.} \\
&\quad \left. \left. \frac{}{\frac{1}{4}(-f^s_{l_1,-2} + f^s_{l_1,2})(-f^s_{l_2,-2} + f^s_{l_2,2}) \right] I^{l_1}_3 I^{l_2}_3 \right]^{1/2}}.
\end{aligned}
\tag{3.14}
$$

3.2.2. From the continuous to the discrete world

The whole mathematical theory built both in sections 2.3 and 3.2.1 is based on continuous and smooth functions (remember $f \in \mathcal{L}^2([0, +\infty) \times [-\pi, \pi])$), but astronomical images are finite matrices obtained by integrating the flux coming from the sources in the sky. As it was pointed out by Massey & Refregier (2005), two different solutions to this general problem are proposed: either smoothing the data or pixelating the basis functions. The former involves the selection of a certain arbitrary interpolation algorithm which maps the matrix space of the real data onto the continuous world of CHEFs. However, plenty of open issues come up with the former approach: which interpolation scheme to use, how accurate this interpolation will be, how long the algorithm will take to interpolate the hundreds

of pixels in an image... In addition to this, if the original image has steep or irregular areas or it is simply too grainy, interpolation is not a trivial issue. Therefore, from experience with other methods, smoothing the data is not a good solution and it was not explored in detail.

On the other hand, discretizing the smooth CHEF functions is a much practical idea, not only because of its own simplicity but also because integrals in (3.5) become sums and computations can be coded. However, this apparently easy implementation can become a double-edged sword due to the so called *aliasing*. Aliasing refers to the distortion or artifact which results when the sampled signal is different from original continuous function. Let us show the origin of this aliasing from an incorrect sampling. Let f be any continuous function and f^{dig} its discrete or digitized version. This f^{dig} can be obtained by multiplying the original f by several Dirac delta functions:

$$\begin{aligned} f^{dig}(x,y) &= f(x,y)\cdot S(x,y) = f(x,y)\cdot\left(\sum_{j_1=-\infty}^{+\infty}\sum_{j_2=-\infty}^{+\infty}\delta(x-j_1\Delta x, y-j_2\Delta y\right) = \\ &= \sum_{j_1=-\infty}^{+\infty}\sum_{j_2=-\infty}^{+\infty} f(j_1\Delta x, j_2\Delta y)\cdot\delta(x-j_1\Delta x, y-j_2\Delta y). \end{aligned} \tag{3.15}$$

In this way, the function f is being sampled on a grid of $(\Delta x, \Delta y)$ cells size. If we calculate the two-dimensional Fourier transform of the sampled image:

$$\begin{aligned} \widehat{f^{dig}}(\omega_x,\omega_y) &= (\widehat{f\cdot S}(\omega_x,\omega_y) = \frac{1}{4\pi}\hat{f}(\omega_x,\omega_y) * \hat{S}(\omega_x,\omega_y) = \\ &= \frac{1}{\Delta x\Delta y}\hat{f}(\omega_x,\omega_y) * \left(\sum_{j_1=-\infty}^{+\infty}\sum_{j_2=-\infty}^{+\infty}\delta(\omega_x - j_1\omega_{xs}, \omega - j_2\omega_{ys})\right) \end{aligned} \tag{3.16}$$

where $*$ is the convolution operator and $\omega_{xs} = \dfrac{2\pi}{\Delta x}$ and $\omega_{ys} = \dfrac{2\pi}{\Delta y}$ the frequency rate in Fourier domain (we have adopted the assumption that f is bandlimited in frequency space, so $\hat{f}(\omega_x,\omega_y) = 0$ for $|\omega_x| > \omega_{xc}$ and $|\omega_y| > \omega_{yc}$, for certain ω_{xc} and ω_{yc}). Then:

$$\begin{aligned} \widehat{f^{dig}}(\omega_x,\omega_y) &= \frac{1}{\Delta x,\Delta y}\int_{-\infty}^{+\infty}\!\!\!\int \hat{f}(\omega_x-\alpha,\omega_y-\beta)\cdot\left(\sum_{j_1=-\infty}^{+\infty}\sum_{j_2=-\infty}^{+\infty}\delta(\alpha-j_1\omega_{xs},\beta-j_2\omega_{ys})\right)\,d\alpha\,d\beta = \\ &= \frac{1}{\Delta x,\Delta y}\sum_{j_1=-\infty}^{+\infty}\sum_{j_2=-\infty}^{+\infty} f(\omega_x-j_1\omega_{xs},\omega_y-j_2\omega_{ys}). \end{aligned} \tag{3.17}$$

That is, the spectra of the sampled image coincides with that of the continuous function, infinitely repeated on the frequency plane, on a grid with resolution $\left(\dfrac{2\pi}{\Delta x}, \dfrac{2\pi}{\Delta y}\right)$. So, if $(\Delta x, \Delta y)$ are chosen to be too large in comparison with the limits of $\hat{f}$ in Fourier domain, its individual spectra could overlap, producing the aforementioned aliasing (Pratt (2007)).

Many different ways are proposed to carry out this discretization, such as sampling the CHEFs on a pre-established grid, integrating analytically the basis functions within rectangular pixels or applying a Monte-Carlo method. As it was pointed out by Berry et al. (2004), discretization by just evaluating

the basis functions on a grid is highly inaccurate, since if the object has features smaller than a pixel size, these cannot be modeled. When it comes to integration by pixels, this is much slower than the other methods, but it is also the most precise one. So, we reached an acceptable trade-off adopting two different strategies according to the size of the images and the scale of the features present in them:

- If the object to analyze is smaller than 100 by 100 pixels or has features within a scale smaller than the pixel size, the integration by pixels method is applied to get the CHEF bases:

$$\{\phi_{nm}(r_j,\theta_k,L)\}_{nm} = \left\{ \iint\limits_{(r_j,\theta_k)\ \text{pixel}} \frac{C}{\pi} TL_n(r_j)W_m(\theta_k) \right\}_{nm}, \tag{3.18}$$

  where (r_j,θ_k) are the coordinates of the nodes of a polar grid of size $p_1 \times p_2$. As this process is quite slow a whole "dictionary" of basis functions with different scale values has been previously computed on a grid of 100 by 100 pixels, with $N^{max} = M^{max} = 10$. In this way, to decompose an object it is just necessary to pick the basis functions corresponding to the nearest scale to the galaxy half-light radius and selecting the desired number of coefficients.

- If the object to analyze is greater than 100 by 100 pixels, features are highly unlikely to be smaller than the pixel size, since they will be spread out all over the image. In these cases it is enough to sample the basis functions at the center of each pixels, just taking into account that the resolution of the grid cannot be smaller than the scale of the basis functions (in order to avoid lying two peaks on the same pixel):

$$\{\phi_{nm}(r_j,\theta_k,L)\}_{nm} = \left\{ \frac{C}{\pi} TL_n(r_j)W_m(\theta_k) \right\}_{nm}. \tag{3.19}$$

Thanks to the high stability of CHEF bases, approximating the scale parameter for small images does not represent a great loss of accuracy, and the improvement on the computational time is very significant.

3.2.3. Orthonormalization of the discrete functions

Once we got the matrix forms of the analytical CHEF functions by any of the two method described in the previous section, we have to make them orthogonal, since the previous discretization step does not produce a complete, let alone orthonormal, basis on the pixel space. In principle, one could sample the basis at the pixel centers and fit the galaxies using an optimization scheme. The basis is so well suited to fit galaxy profiles that it can be used in this way with reasonably good results. However, completeness and orthonormality are essential for a robust and automated approach. The first property ensures the flexibility of the basis, the capability of fitting all possible galaxy profiles, including irregulars. The second is crucial for a fast implementation, since the coefficients of the decomposition can be calculated in a straightforward way, using the inner product defined in the space of real vectors. Because of the importance of this problem, two radically different approaches have been tried:

- *SVD approach.* It can be shown that in the case that the matrices are linearly independent, there exists a unique vector of coefficients a that minimizes the residual between the model and the original galaxy image f (Berry et al. (2004)):

$$\epsilon = |\Phi a - f|, \tag{3.20}$$

where Φ is a matrix composed by the CHEF matrices (reshaped as vector columns). It can be proved that if

$$\Phi = U\Sigma V^* \tag{3.21}$$

is the Singular Value Decomposition (SVD) of the CHEF matrix Φ (where U and V are unitary matrices, Σ is a diagonal one and $*$ denotes the transpose conjugate), then the vector of coefficients a minimizing (3.20) is:

$$a = V\overline{\Sigma}^* U^* f \tag{3.22}$$

where $\overline{\Sigma}^*$ is constructed by taking the transpose of Σ and replacing each non-zero singular value in the diagonal by its inverse.

Using this result, it is possible to find the best fit to the original image with the discrete CHEF matrices directly, without making any modification on them. This solution is smart and fast, due to the matrix implementation of the whole process, where the slowest step is performing the SVD, although there exist several optimized routines to carry out this task.

- *CGS approach.* The whole set of CHEF matrices Φ can be orthogonalized using an orthonormalization method and, in this way, coefficients may be calculated by means of the usual inner product. Firstly, the Classical Gram-Schmidt (CGS) orthonormalization process was chosen, by its simplicity and the possibility of being implemented in a matrix form. However, CGS final vectors are usually not orthonormal, due to rounding errors and the algorithm's very poor numerical properties (Golub & Van Loan (1996)). Because of that, we decided to use the Modified Gram-Schmidt algorithm (MGS), which yields the same results as CGS in exact arithmetic but displays a much better behaviour in finite-precision arithmetic (Giraud & Langou (2001)). The purpose of the MGS algorithm is decomposing a matrix $A \in \mathbb{R}^{m\times n}$ into the product of two matrices $Q \in \mathbb{R}^{m\times n}$ and $R \in \mathbb{R}^{n\times n}$, so that $A = QR$. The matrix Q must have orthonormal columns and R must be upper triangular. This initial part of the method is also common to the CGS algorithm, but the difference between the two methods is that in the MGS the norm $\|I - QQ^T\|$ can be predicted by an upper bound, whereas there exists no such bound for the CGS (Björck (1994)). In this work, we have implemented the MGS according to the algorithm described in Golub & Van Loan (1996), but there are numerous the efforts to parallelize the process (Rünger & Schwind (2005)). Concretely, the implemented algorithm consists on:

```
for k = 1:n
    R(k,k) = ||A(1:m,k)||_2
    Q(1:m,k) = A(1:m,k)/R(k,k)
```

```
    for j = k+1:n
       R(k,j) = Q(1:m,k)^T A(1:m,j)
       A(1:m,j) = A(1:m,j)-Q(1:m,k)R(k,j)
    end
end
```

The use of orthonormalized CHEF matrices allow us to compute CHEF coefficients in a simpler way than using SVD, since the integral (3.3) becomes the usual inner product in the $\mathbb{R}^{p_1 \times p_2}$ space (being $p_1 \times p_2$ the size of the image):

$$\langle f, W_m \rangle = \sum_{i=0}^{m_1} \sum_{j=0}^{m_2} f(r_i, \theta_j) W_m(\theta_j). \tag{3.23}$$

and, in this way, using the new basis ϕ_{nm} we have that the image light distribution f can be decomposed as

$$f(r_j, \theta_k) = \sum_{nm}^{NM} f_{nm} \phi_{nm}(r_j, \theta_k), \tag{3.24}$$

where the values of the decomposition coefficients are fast and accurately calculated by means of the usual inner product in the matrix space, that is:

$$f_{nm} = \sum_{j,k} f(r_j, \theta_k) \phi_{nm}(r_j, \theta_k), \tag{3.25}$$

where the sum $\sum_{j,k}$ goes over all the pixels in the image.

Although the SVD method is easier to implement and faster to execute, it presents two obstacles. The first is that the coefficients obtained by this method have no way of being used for the determination of morphological parameters (see section 2.3.4), since the expressions developed in that section rely on the orthonormality of the basis functions and they have no equivalence in the discrete world without this condition. So, just in the case that a morphological model is required (for image denoising, for instance) and the coefficients of the decomposition are no longer used for anything, SVD method is not really suitable. In addition, the optimized routines for SVD involve the inversion of such large matrices that memory usually runs out, when the size of the image being analyzed is too big. Therefore, we have opted to orthonormalize the CHEF matrices, although the computational effort required is higher (in the case of the MGS method, not the classical one).

3.2.4. Choice of the center

The radial symmetry of the CHEF basis functions makes them highly suitable to model astronomical images, since they are designed to efficiently represent objects that are well described in polar coordinates. The origin of this polar grid where CHEF functions will be evaluated on is extremely important, specially because the basis functions have a extreme at it, and it is important that this one matches the center of the astronomical object, where the light flux intensity is higher. If they

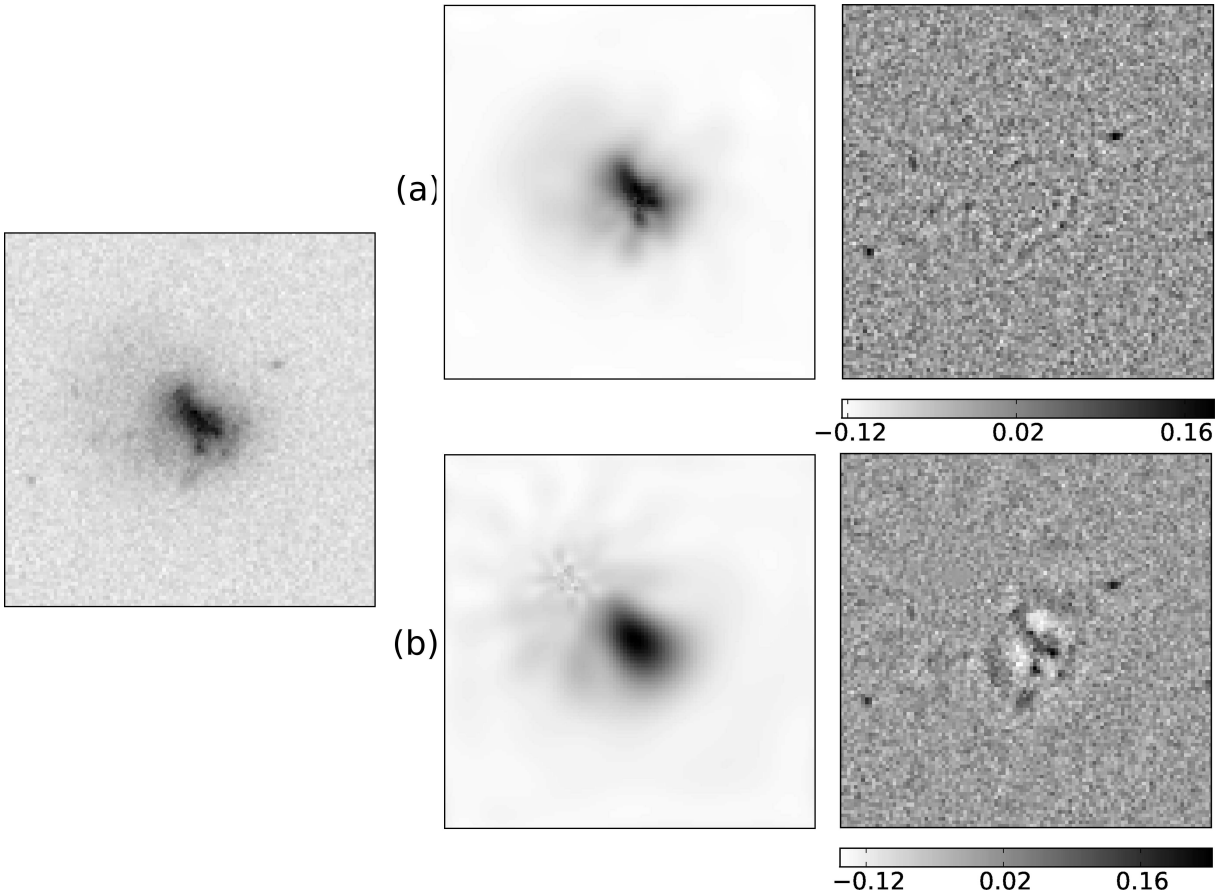

Figure 3.3 Real galaxy from UDF decomposed using: a) a correct estimated center and b) a center moved 20 pixels both in the x and y coordinates to the upper left corner. Both the resulting models and the residuals are displayed.

are not properly centered on the object, the results may not be the desired ones. For instance, if the origin of the grid does not match the center of the galaxy, this could always be modeled away (because CHEFs constitute a basis, so every image can be decomposed), but the number of coefficients that would be needed would become clearly higher. So, for fixed values of N^{max} and M^{max}, the resulting reconstruction could be poorer if the center is wrongly determined. By way of illustration, a real galaxy from UDF has been decomposed using both a correct estimation of the center and a shifted center by a distance of approximately $\sqrt{20^2 + 20^2} \approx 28{,}28$ pixels to the northwest (see figure 3.3). The same number of coefficients, $N = M = 10$, has been used in both cases, but results are obviously more accurate in the first one.

After testing several possibilities, such as the centroid provided by SExtractor, the center of mass of the frame containing the galaxy or the center of mass of the object, calculated using Sextractor segmentation map, we determined that the best estimator was the first one, the SExtractor centroid.

3.2.5. Choice of the scale size

The scale parameter L is not related to the shape of the CHEF basis functions, but to their width (the scale has an "accordion" effect over the basis functions). The larger the scale is, the more slowly the basis functions reach their last extreme, as can be seen in figure 2.3. Therefore, the steepness of the peaks in central area of CHEFs is closely related to this scale parameter, and thus also their capability to represent features of a certain size. A too small scale value would make all the high frequencies in the image be represented accurately, that is, we would overfit the noise in the central part of the fit. On the contrary, a too large scale size would make the basis functions lose the high frequencies of the image, and we would model a smooth version of the objects, that is, the decomposition would work with poor resolution incapable of fitting the central peak and the tiny features. Two different options are available to solve this issue:

- Optimization of the scale parameter. In case that a great accuracy is required to model an object, the Levenberg-Marquardt algorithm (Levenberg (1944)) is applied until the optimal value of L is found, that is, the one which minimizes the residual between the original profile of the source and the model profile (these profiles are both determined by IRAF task ELLIPSE).

- Approximation of the scale parameter. As CHEF bases have been proved to be very stable and robust under relatively small changes in the scale parameter, in most of the cases is not necessary to find the exact best value for L, but to take the half-light radius of the galaxy as a proxy, provided by SExtractor (remember that this parameter has happened to be much more reliable to measure galaxies size than the classical FWHM). This option yields very accurate results in spite of not being the optimal one and it is the approach used by default in the code.

By way of example, the same galaxy from the UDF used in the previous section has been decomposed using the same number of coefficients ($N = M = 10$) three different values for the scale parameter L: the fraction of light radii provided by SExtractor (figure 3.4(b)), ten times its value (figure 3.4(c)), and 1/10 of its value (figure 3.4(a)). As it can be observed, the residual maximal values do not differ too much, but this subtle difference is enough to introduce high differences in the morphological shape measurement formulas in section 3.2.1. The noticeable difference is due to the way in which central bulge is modeled: in figure 3.4(a), it appears overfitted, since the bulge is rich in high frequencies, so a so small scale generates a detailed modeling, even down to the noise; however, in figure 3.4(c) the central area in underfitted, because the scale is too high to contain its small features.

3.2.6. Choice of the number of coefficients

Theoretically, if the whole infinite set of CHEF coefficients could be calculated, the image would be perfectly represented. In practise, we must choose a number of coefficients high enough to model the objects accurately, but optimizing the computation time. In addition to this, if too many coefficients are used in the decomposition, the noise present in the image would be modeled as well. Because of that we have decided to apply a chi square criterium to automatically estimate the number of coefficients needed for the decomposition. The chosen chi square is obtained so that it yields a value

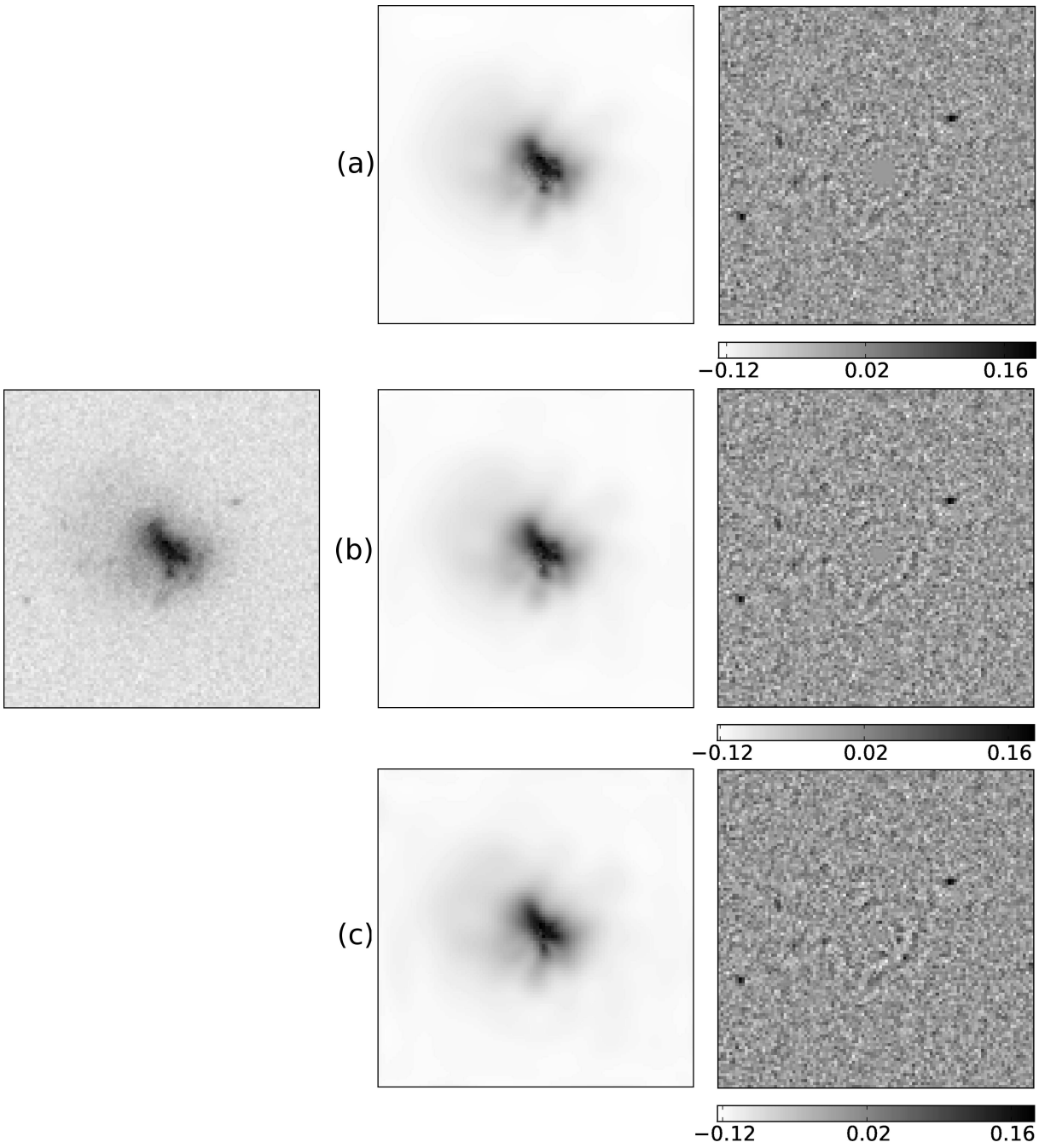

Figure 3.4 Real galaxy from UDF decomposed using: b) a correct estimated scale parameter L^{opt}, a) a too small scale $L^{opt}/10$, and c) a too large scale $L^{opt} * 10$. Both the resulting models and the residuals are displayed.

close to one for the reconstruction residual between the model and the original image, weighted by the pixel error and the number of coefficients:

$$\chi^2 = \frac{1}{n_{pixel} - n_{coeff}} \sum_{j,k} \frac{\left(f(r_j, \theta_k) - \sum\limits_{n,m} f_{n,m} \phi(r_j, \theta_k, L) \right)^2}{\delta^2(r_j, \theta_k)} \tag{3.26}$$

where f is the observed image, f_{nm} are its CHEF coefficients, δ^2 is referred to the pixel noise map, n_{pixel} is the number of pixels in f (that is, $n_{pixel} = p_1 \cdot p_2$), and n_{coeff} represents the number of CHEF coefficients used to decompose f (i.e., $n_{coeff} = (N+1)(2M+1)$). At the point where $\chi^2 = 1$, the residual between the observed data and the model is consistent with the noise level.

As in the previous sections, figure 3.5 displays the difference in the results after choosing the number of coefficients ($N = M = 10$) which yields $\chi^2 = 1$, a smaller one ($M = M = 3$) and a too large value ($N = 15, M = 20$). In the case of a poor combination of coefficients (figure 3.5(a)), the resulting model is very rough, hardly a smooth version of the original data. When using too many coefficients, we can observe that a large fraction of the noise is also modeled, and some other artifacts appear in the image (figure 3.5(c)).

It is interesting to visualize which features in a galaxy correspond to which coefficients. Figure 3.6 shows the decomposition of an spiral galaxy using just some subsets of coefficients: the central bulge is captured by the $|m| < 2$ coefficients while the spiral arms are described by the $|m| \geq 2$ components.

Based on results of our fits, we see that the optimal combination of N and M for objects displaying radial symmetry and low eccentricity requires a higher number of Chebyshev than Fourier components (that is, $N > M$). That is the case of the spiral galaxy shown in figure 3.6. On the contrary, if the source to decompose has an elliptical shape with great eccentricity or it is irregular, the best option is, on average, computing a higher number of Fourier than Chebyshev components (i.e., $M > N$).

3.3. Examples

By way of illustration, three representative real galaxies from UDF (Beckwith et al., 2004; Coe et al., 2006) have been extracted and processed using CHEF algorithm, to show the performance of the method when dealing with different types of morphologies and complexity levels.

Figures 3.7,3.8, and 3.9 show some examples of Hubble Ultra Deep Field galaxies. The large amount of detail revealed in those images makes them a useful testbed for galaxy decomposition methods. These objects, while typical, are not trivial to fit due to their complicated structure. The first is a spiral galaxy, displayed in figure 3.7. The image frame has 121×121 pixels, and the algorithm establishes that the best fit is obtained with $N = 15$ and $M = 14$, i.e., using $n_{coeff} = (15+1)(14 \times 2 + 1) = 464$

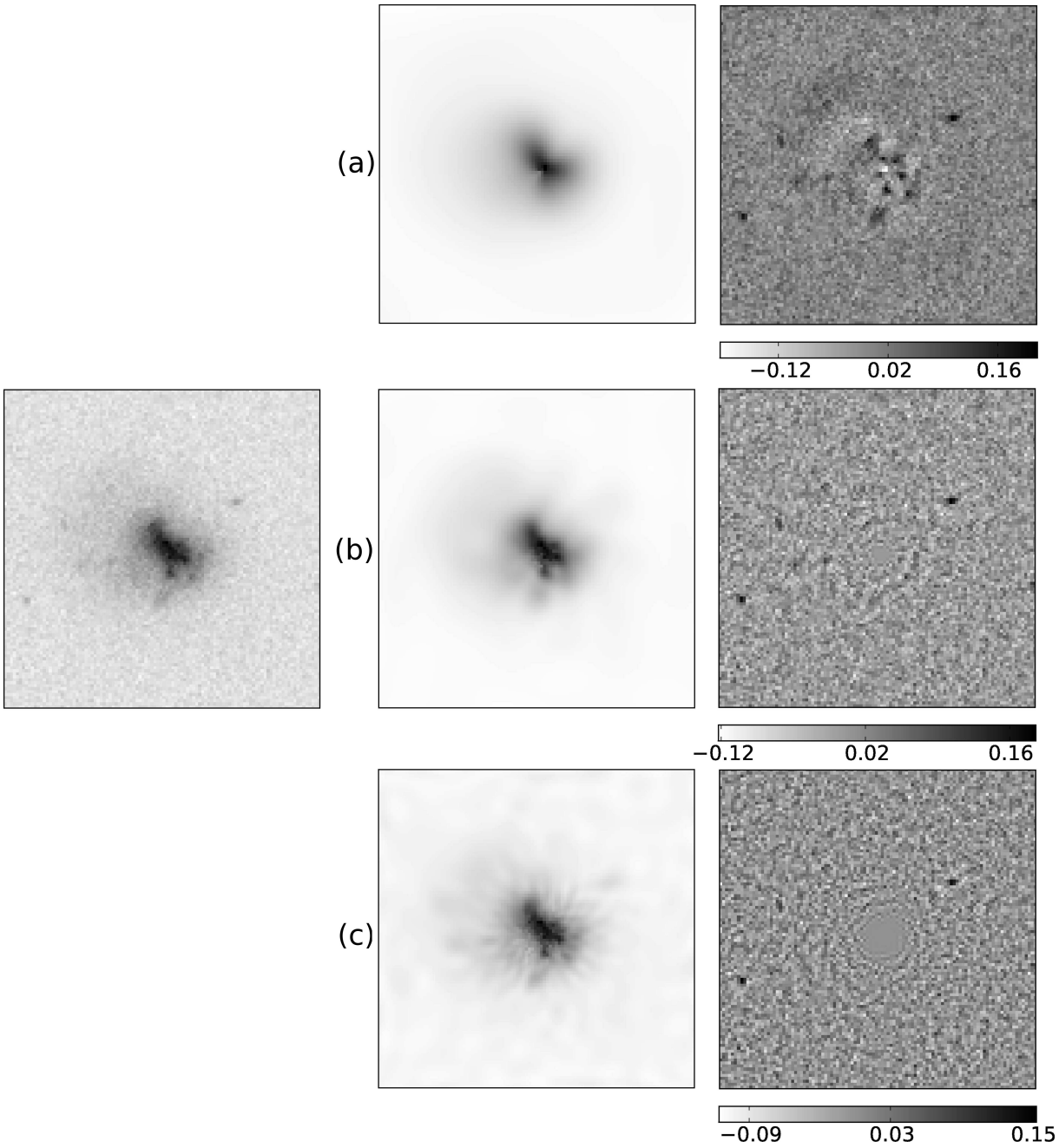

Figure 3.5 Real galaxy from UDF decomposed using: b) a number of coefficients $N = M = 10$ which yields $\chi^2 = 1$, a) too few coefficients $N = M = 4$, and c) too many coefficients $N = 15, M = 20$. Both the resulting models and the residuals are displayed.

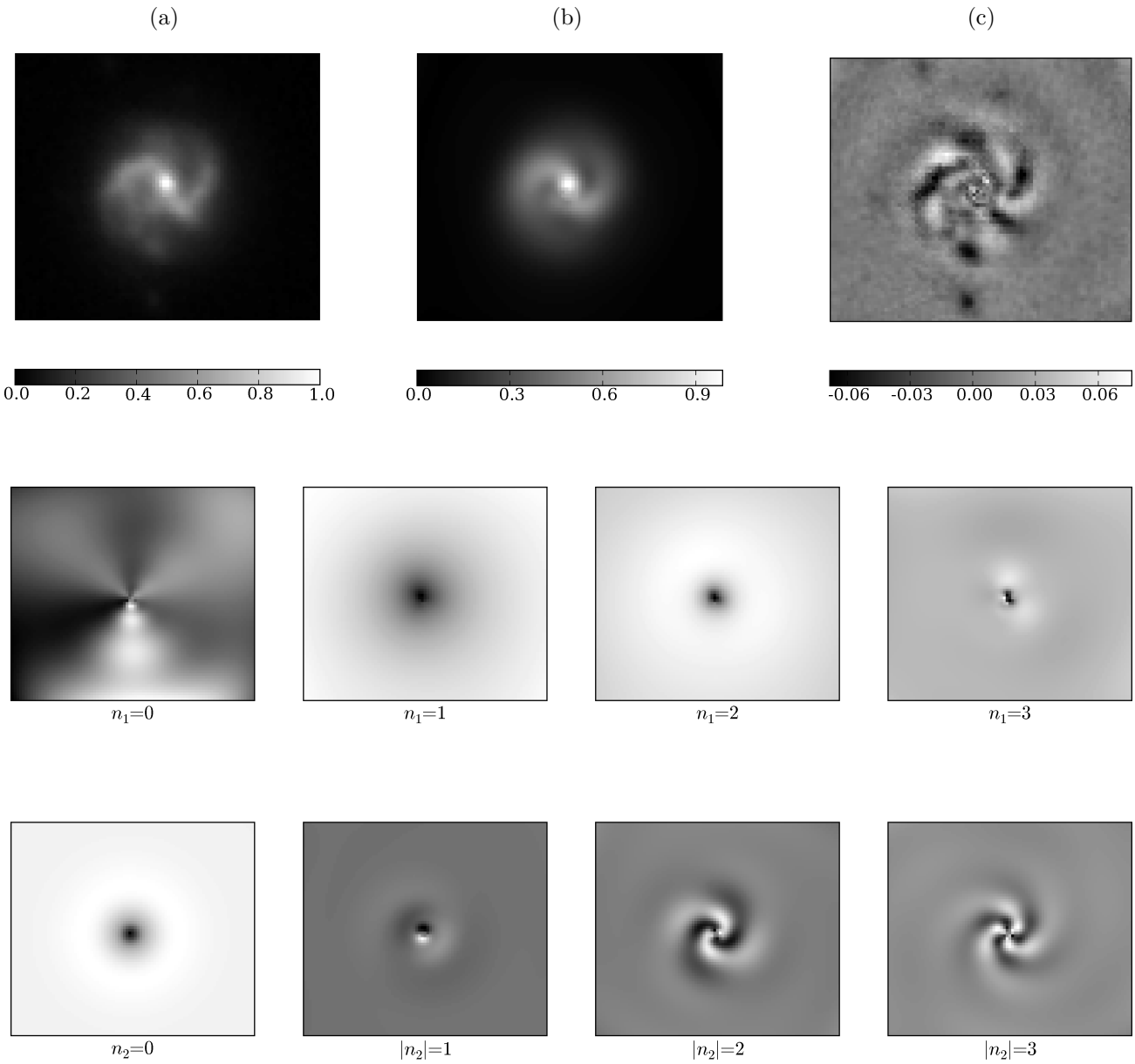

Figure 3.6 Reconstruction of a spiral galaxy from the HDF. The original image and the final Chebyshev-Fourier reconstruction are shown in the top panels (a) and (b), whereas (c) shows the obtained residuals in linear scale. The bottom panel displays the partial reconstruction of the image, using just a few coefficients: the central bulge is captured by the $|m| < 2$ coefficients while the spiral arms are defined by the $|m| \geq 2$ components.

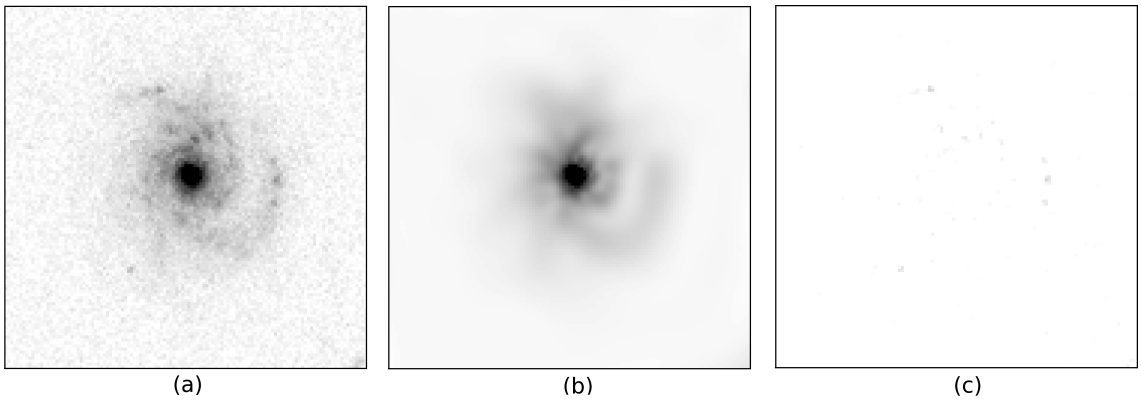

Figure 3.7 CHEF decomposition of a spiral galaxy from the UDF: a) original image, b) CHEF reconstruction using $N = 15$ radial and $M = 14$ angular coefficients, (c) residuals

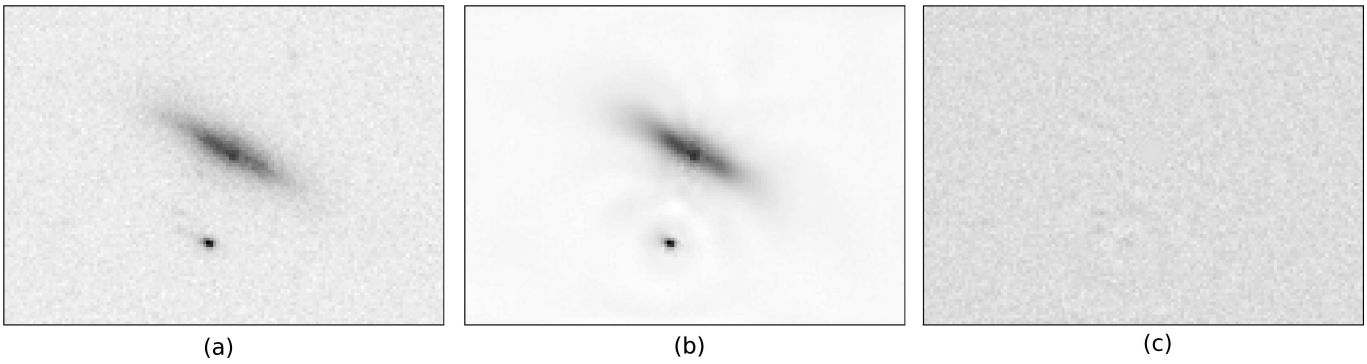

Figure 3.8 CHEF decomposition of an edge-on galaxy from the UDF: a) original image b) CHEF reconstruction with $N = 5$ and $M = 7$, and c) residuals (note that the small object below the main galaxy is also fit separately)

coefficients. The very low level of the residuals shows that the CHEF basis can easily fit both the central bulge and large structures like spiral arms. We apply the same procedure to other two galaxies, an edge on galaxy with very high observed ellipticity (figure 3.8) and a highly irregular galaxy (figure 3.9). The fits are also excellent, what illustrates the flexibility of the CHEF basis, able to handle most galaxy morphologies.

3.4. Conclusions

Throughout this chapter, all the hurdles we found in the process to implement the CHEF algorithm have been described. The CHEF pipeline, written in a Python package, can be summarized in nine steps, and we must remark that the only inputs for the code are the image to be processed and the maximum number allowed of coefficients, N^{max} and M^{max}. The whole pipeline has shown to be fast and precise, and every step has been conveniently automated to require a low level of interactivity from the user, so the method can be easily applied to large surveys data.

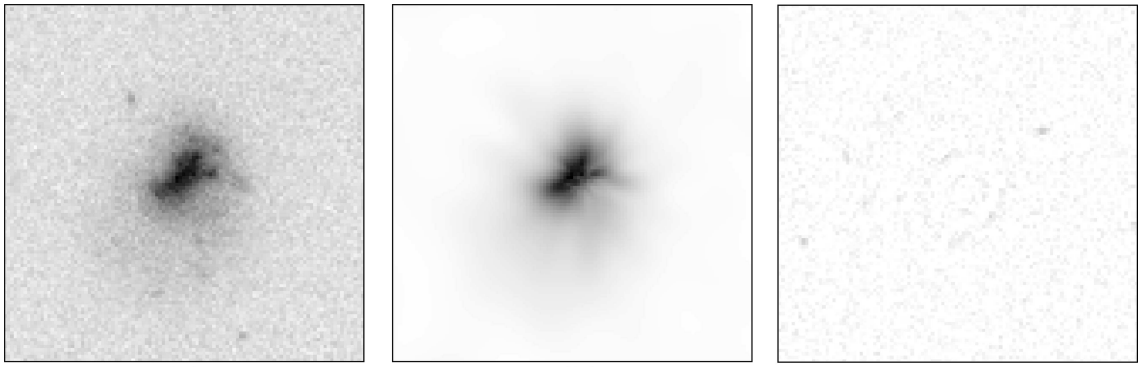

Figure 3.9 CHEF decomposition of an irregular galaxy from the UDF: a) original image b) CHEF reconstruction with $N = 5$ and $M = 7$, and c) residuals

Although the mathematical background of CHEFs has been developed in the complex world, its practical implementation has been performed in real world, since galaxy images are real and crossed, imaginary products of the basis functions are useless. In this way, computational speed has been increased, and the number of coefficients needed to represent an image is reduced by half. All the formulae inferred in chapter 2 has been translated into this real world, even those to calculate the morphological and photometric parameters.

Discretization of the basis has been performed using the integration by pixels, although a great set of basis functions with different values of the scale parameter L has been pre-calculated and stored to make the computations faster. The loss of orthogonality due to this pixellation has been solved by means of the Modified Gram-Schmidt orthonormalization method, which has been proved to be more stable and accurate than the classical one. Another approach, avoiding the orthonormalization of the bases, has also been tried, just calculating the coefficients of the decompositions by using a Singular Value Decomposition of the discretized basis functions. However, due to the computational requirements, the former option is the one mainly used in the CHEF pipeline.

The choice of several parameters as the center, the scale size, or the optimal number of coefficients is made automatically by the algorithm, according to several criteria. The centroid provided by SExtractor has been proved to be a good option for the center, while the half-light radius has resulted to be a proper candidate for the scale parameter. However, a version of the pipeline allow the user to find the exact and optimal value for L is available, in case that an extreme accuracy is required. When it comes the optimal number of coefficients N and M, a chi square test has been implemented to calculate them, avoiding in this way the overfitting or the poor modeling of the sources.

Some examples of real galaxies from UDF have been displayed, in order to show the reliability of the method when dealing with different types of morphologies and complexity levels.

Bibliography

Beckwith, S.V.W. (2004). The Hubble Ultra Deep Field. STScI.

Benítez, N. et al. (2009). Optimal Filter Systems for Photometric Redshift Estimation. ApJ, 692, 1, L5

Berry, R.H; Hobson, M.P; Withington, S. (2004). Modal decomposition of astronomical images with application to shapelets. MNRAS, 354, 199-211.

Bertin, E; Arnouts, S. (1996). SExtractor: software for source extraction. Astronomy & Astrophysics Supplement Series, 117, 393-404.

Björck, A. (1994). Numerics of Gram-Schmidt Orthogonalization. Linear Algebra Appl., 197-198:297-316.

Coe, D., Benítez, N., Sánchez, S.F., Jee, M., Bouwens, R., Ford, H. (2006). Galaxies in the Hubble Ultra Deep Field. I. Detection, Multiband Photometry, Photometric Redshifts, and Morphology. AJ, 132, 2, 926c

Doug, T. (1986). The IRAF data reduction and analysis system. Instrumentation in Astronomy VI, Proceeding of the meeting, Society of photo-optical instrumentation engineers, p. 733.

Giraud, L; Langou, J. (2001). When modified Gram-Schmidt generates a well-conditioned set of vectors. CERFECS, Technical Report, TR/PA/01/17.

Golub, G.H; Van Loan, C.F. (1996). Matrix Computations, The John Hopkins University Press, 694pp, USA.

Levenberg, K. (1944). A method for the solution of certain non-linear problems in least squares. The quarterly of applied mathematics, 2, 164-168.

Massey, R; Refregier, A. (2005). Polar shapelets. Mon. Not. R. Astron. Soc, 363, 197-210.

Moles, M. et al. (2008). The Alhambra Survey: a Large Area Multimedium-Band Optical and Near-Infrared Photometric Survey. AJ, 136, 1325.

Postman, M; Coe, D; Ford, H; Riess, A; Zheng, W; Donahue, M; Moustakas, L; and CLASH team. CLASH: Cluster lensing and supernova survey with Hubble. In AAS Meeting #217, #227.06. Bulletin of the American Astronomical Society, 43.

Pratt, W.K. (2007). Digital image processing. John Wiley & Sons, USA, 786pp.

Rünger, G; Schwind, M. (2005). Comparison of different parallel modified Gram-Schmidt algorithms. Lecture Notes in Computer Science, 3648/2005, 826-836.

4

Comparison of different methods

We compare the CHEF decomposition with two of the most widely available techniques for galaxy modeling, GALFIT (Peng et al., 2002, 2010) and the IDL Shapelets software. GALFIT (Peng et al., 2002, 2010) uses several two-dimensional analytic models to fit the galaxy images, as the Sérsic profile, the exponential disk, the Nuker law or the Gaussian and Moffat/Lorentzian functions. It is possible to use an arbitrary number of components. The shapelets software (Massey & Refregier, 2005) is based on an orthonormal basis built from Hermite polynomials and Gaussians. Figures 4.1 and 4.2 shows the results of fitting 12 randomly chosen galaxies from UDF with GALFIT, IDL Shapelets and our CHEF pipeline.

The GALFIT results show that radially symmetrical multicomponent models fail to adequately represent the wide variety of shapes displayed by galaxies observed at high S/N, and that it is essential to include angular components, as indeed the new version of GALFIT does. However, the main drawback of GALFIT is the requirement that fits must be performed interactively, in order to provide the right initial parameters, the number and type of the components, etc. This precludes its use to obtain highly accurate fits of large numbers of galaxies.

We have run the IDL shapelets software allowing $n_{max} = 20$ as the maximum order, equivalent to $n_{coeff} = 400$ coefficients. For comparison, we use $N^{max} = M^{max} = 10$, equivalent to $n_{coeff} = 231$ coefficients, for the CHEF decomposition, which also runs faster, even taking into account the orthonormalization process. Despite using more coefficients, we see that the shapelet reconstruction often fails to adequately fit all galaxy shapes and tends to produce ring-like artifacts, probably as a consequence of the inestability of the radial profile fits (Bosch, 2010).

The CHEF decomposition manages to keep the residuals to a very low level, fitting very complicated galaxy shapes, producing very few artifacts. In addition, as we will see below, it obtains highly accurate estimates of galaxy total fluxes and shapes.

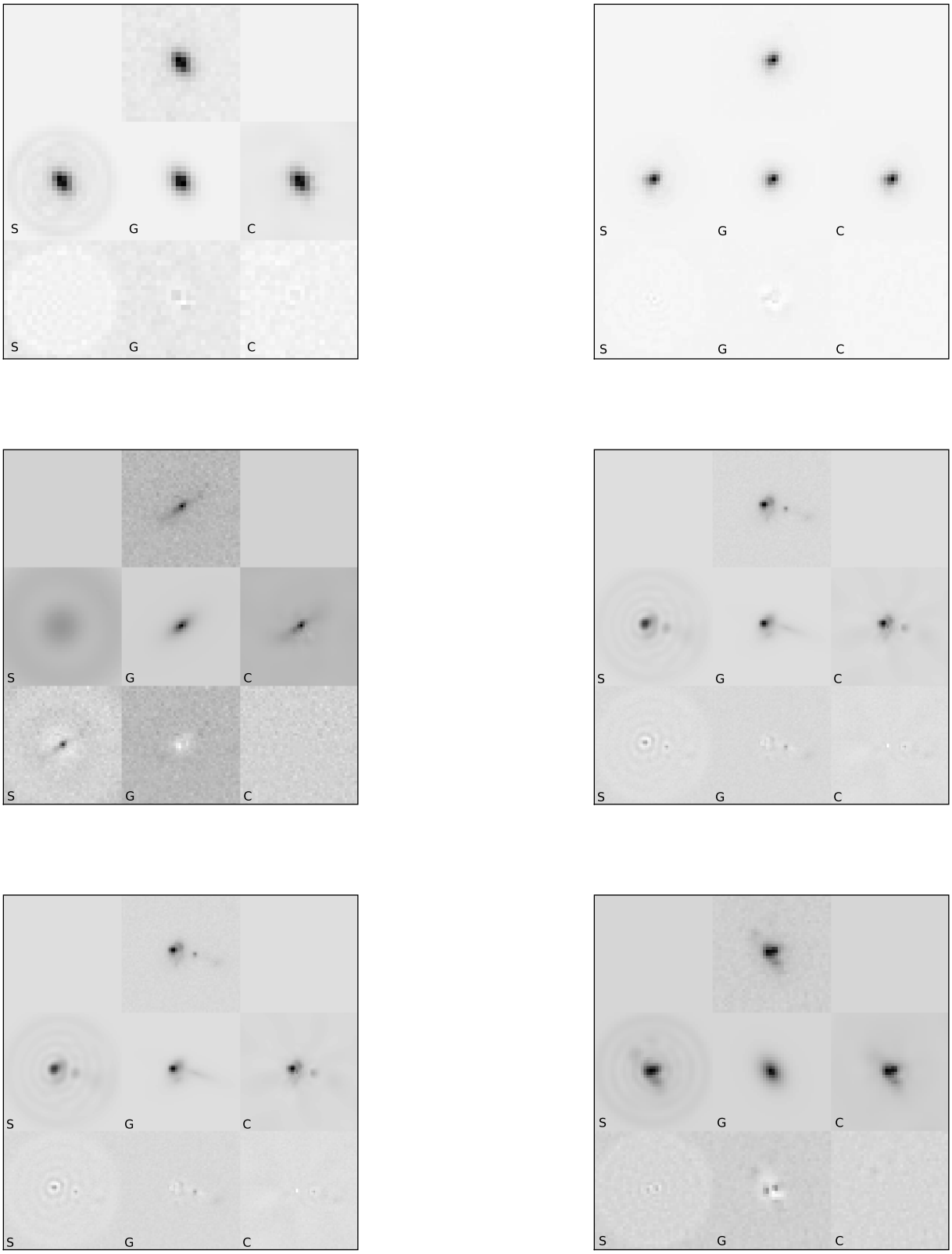

Figure 4.1 Reconstructions and obtained residuals, after applying the three methods to an ensemble of galaxies randomly extracted from UDF: images on the top correspond to the original galaxies, first row below it represents the reconstructions obtained by shapelets, GALFIT and CHEF softwares (from left to right), and second row shows the resulting residuals, in linear scale.

A comparison more objective and quantitative than the visual one between shapelets and CHEFs, has been performed by creating a realistic sample of more than 350 mock galaxy profiles with different morphological characteristics. Each simulated image consists on a matrix of 100×100 pixels, displaying a Sérsic profile whose index ranges from 0.5 to 4 (i.e., from a Gaussian to a de Vaucouleurs profile), which has been sheared with different levels of ellipticity. The ellipticity parameter ranges from 0 to 0.5, and shear operation just consisted on applying to the cartesian coordinates the following transformation:

$$\begin{pmatrix} x^s \\ y^s \end{pmatrix} = \begin{pmatrix} 1-\gamma_1 & -\gamma_2 \\ -\gamma_2 & 1+\gamma_1 \end{pmatrix} \begin{pmatrix} x \\ y \end{pmatrix}$$

where γ_1 and γ_2 are the ellipticity parameters, (x, y) the original cartesian grid, and (x^s, y^s) the sheared grid where the different Sérsic profiles will be evaluated.

We then fit the galaxy shapes using the IDL shapelet software and our CHEF pipeline (see section 3.1). We can see in figure 4.3 that, as expected (Melchior et al. (2010)), shapelets fail to adequately represent objects with high ellipticities, specially for Sérsic indexes $n \approx 1{,}2$, where the relative error in the measurement of the ellipticity reaches 10 %. Although we are using circular shapelets here, elliptical shapelets are also affected by this problem (Bosch, 2010).

Using the formula (2.55), we estimate the ellipticities of our CHEF fits. Our error is $\lesssim 0{,}5\,\%$ for all the explored combinations of profiles and shears. In addition, error in the estimation is much more homogeneous than the one obtained from shapelets code, what proves our pipeline does not seem to introduce any bias. This shows that CHEFs are a very promising tool for weak lensing measurements, an issue which will be explored elsewhere.

On the other hand, to verify the performance of the CHEFs for photometric purposes, we added very low Gaussian noise to the aforementioned galaxies, and applied both the shapelets and CHEF algorithms to the data. In the case of CHEFs, the flux is estimated by means of the formula (3.7). The results are presented in figure 4.4. Again we see that CHEFs provide highly accurate measurements of the total flux for almost all combinations of profile steepness and ellipticity, with a typical error of only $\approx 0{,}4\,\%$. Shapelets, on the other hand, introduce up to 4 % errors in this very high S/N simulated images. Moreover, error by shapelets software is greater for objects with higher Sérsic index, that is, the most extended ones. That is easily understandable, as it was previously pointed out that shapelets fail to properly model both central bulge and extended wings of the objects, so the less compact the source is, the higher the error becomes. On the other hand, CHEFs again display an homogeneous behavior, since they do not impose any constrain on the object extension.

In order to state the good behaviour of CHEFs under the presence of noise, a new whole set of mock galaxies was prepared, this time adding high level Gaussian noise, and the process described in the paragraph before was fully repeated. Results can be observed in figure 4.5.

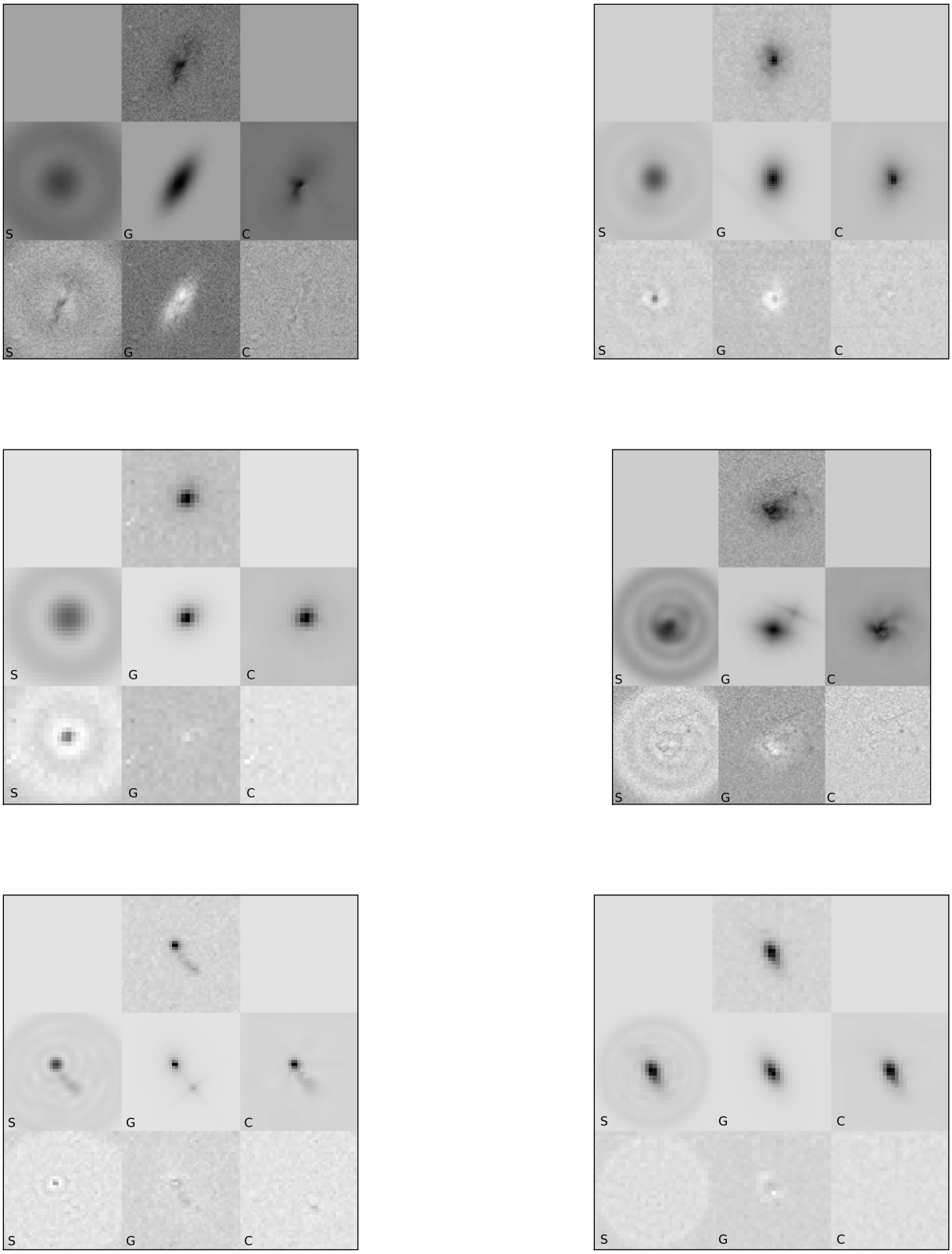

Figure 4.2 Reconstructions and obtained residuals, after applying the three methods to an ensemble of galaxies randomly extracted from UDF: images on the top correspond to the original galaxies, first row below it represents the reconstructions obtained by shapelets, GALFIT and CHEF softwares (from left to right), and second row shows the resulting residuals, in linear scale.

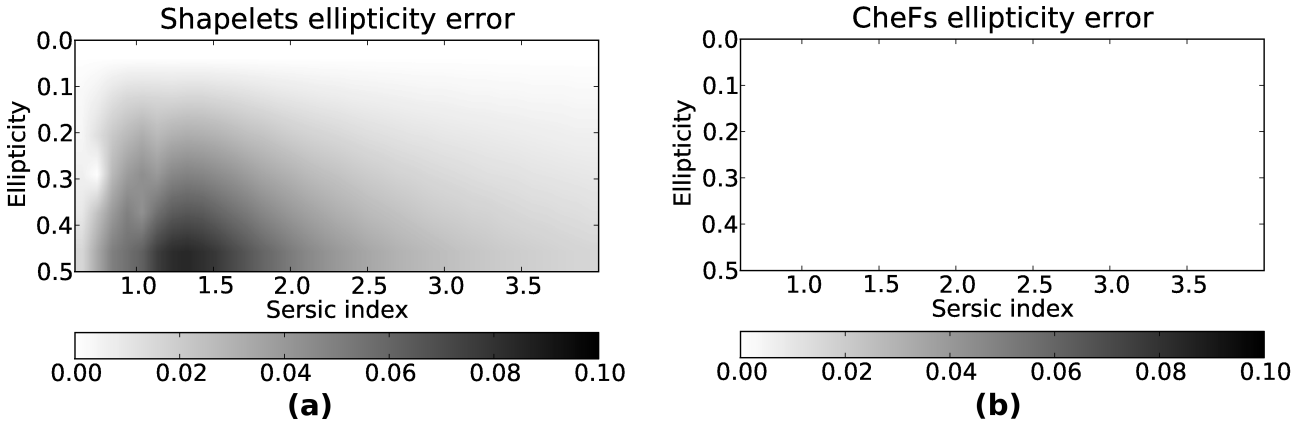

Figure 4.3 Ellipticity absolute error obtained by applying shapelet and CHEF algorithms to a sample of simulated galaxies with different Sérsic profiles and ellipticity parameters.

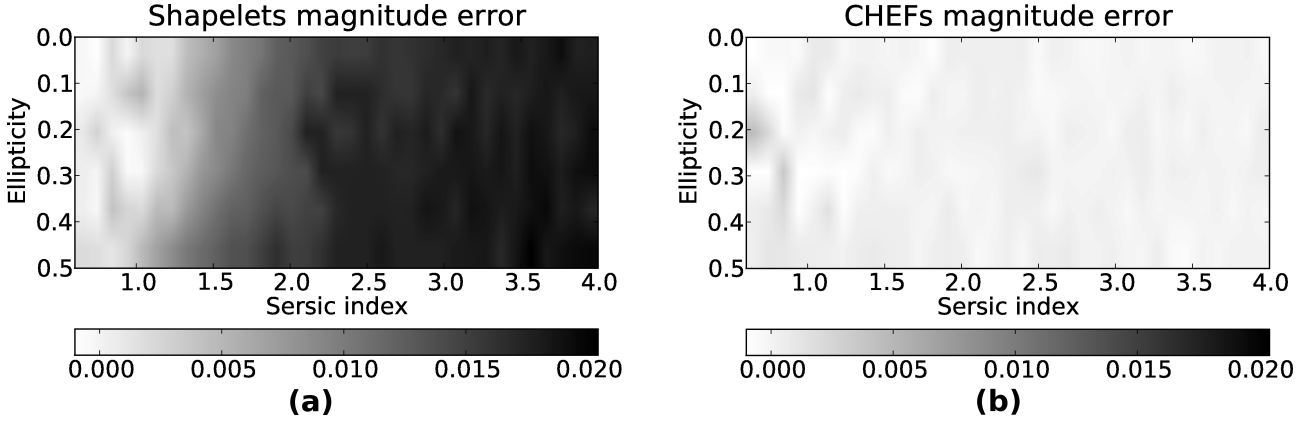

Figure 4.4 Magnitude relative error obtained by applying shapelet and CHEF algorithms to a sample of simulated galaxies with different Sérsic profiles and ellipticity parameters, and contaminated with low level Gaussian noise.

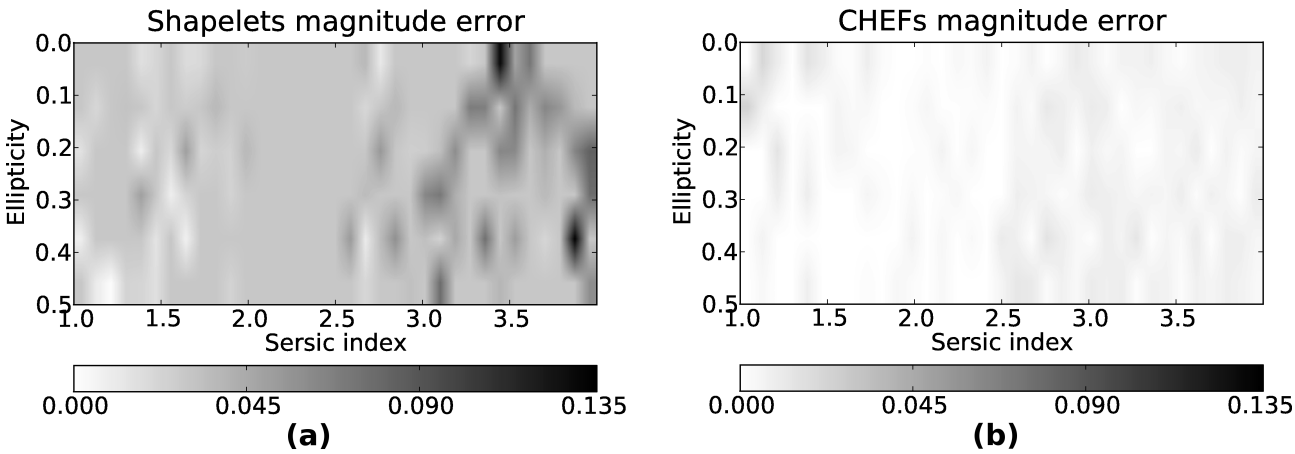

Figure 4.5 Magnitude relative error obtained by applying shapelet and CHEF algorithms to a sample of simulated galaxies with different Sérsic profiles and ellipticity parameters, and contaminated with high level Gaussian noise.

4.1. Conclusions

The CHEF analysis is compared with two of the most widely used techniques in galaxy fitting: GALFIT and the IDL shapelets software, and some visual and representative examples are displayed. It is concluded that GALFIT fails to properly represent certain types of morphologies, specially those ones observed at high S/N with plenty of substructure on them. On the contrary, shapelets behave much better with these complex shapes, but in some cases so many coefficients are needed that the reconstruction suffers from some artifacts like the ringing effect. In addition, they are not able of reaching the same accuracy in both the central bulge and the extended wings of the galaxies. However, the CHEFs have shown to be able to model al kind of shape and using a much fewer number of coefficients than shapelets. In addition, no kind of artifacts are observed in CHEF models.

A more objective and quantitative test has been carried out, creating a mock sample of more than 350 realistic galaxies and applying both the shapelet and CHEF softwares on it. Then, both the magnitude and the ellipticity of the models have been estimated and compared to the original ones, concluding that CHEFs provide much more accurate results in both cases.

Bibliography

Bosch, J. (2010). Galaxy modeling with compound elliptical shapelets, arXiv:1007.1681.

Massey, R; Refregier, A. (2005). Polar shapelets. Mon. Not. R. Astron. Soc, 363, 197-210.

Melchior, P; Böhnert, A; Lombardi, M; Bartelmann, M. (2010). Limitations on shapelet-based weak-lensing measurements. A& A, 510, A75.

Peng, C.Y; Ho, L.C; Impey, C.D; Rix, H.W. (2002). Detailed structural decomposition of galaxy images. The Astronomical Journal, 124, 266-293.

Peng, C.Y; Ho, L.C; Impey, C.D; Rix, H.W. (2010). Detailed decomposition of galaxy images. II. Beyond axisymmetric models. The Astronomical Journal, 139, 2097-2129.

5

CHEF Applications

The role of CHEF bases is not just limited to create morphological models or denoise the images. They have direct applications such as the deconvolution of the PSF, the calculation of morphological parameters using the coefficients or the morphological classification of galaxies, plus a few of more indirect applications as the estimation of the shear for weak lensing, the subtraction of central galaxies in clusters for strong gravitational lensing or the simulation of models.

5.1. PSF deconvolution

The effect of the atmospheric turbulence and the imperfections in the optical system of the telescope makes the observed images be convolved with the so called point spread function (PSF). Many efforts and resources, both technical (better telescopes and cameras) and observational (choice of good seeing astronomical sites, space observations), are spent trying to minimize this effect. However, none of them totally remove the presence of the PSF, so the deconvolution of the original data is needed to recover the real image of the objects. We will show the way this deconvolution can be performed in CHEF domain.

Unlike most operations, the deconvolution operation has no direct mathematical definition, but it is just defined as the inverse of the convolution operator $*$, described by:

$$(f * g)(t) = \int_{-\infty}^{\infty} f(\tau) \cdot g(t-\tau)\, d\tau = \int_{-\infty}^{\infty} f(t-\tau) \cdot g(\tau)\, d\tau \tag{5.1}$$

where f and g are integrable functions. In astronomical images, f represents the object in the sky and g is the PSF, which is defined as the total instrumental profile, that is, the image of a point source obtained with the instrument considered, including the atmospheric perturbation (seeing) if relevant (Magain et al, 1998). In this way, the observed image f^{obs} can be expressed as:

$$f^{obs} = f * PSF + n \tag{5.2}$$

where n is the noise map function. The linearity of both the CHEF bases and the convolution operator makes the PSF deconvolution a very simple task formally speaking, involving the reconstruction of the image with the basis without convolving:

$$f^{obs} + n = f * \mathrm{PSF} + n = \left(\sum_{m=0}^{+\infty} \sum_{n=0}^{+\infty} f_{nm} \phi_{nm} \right) * \mathrm{PSF} + n = \sum_{m=0}^{+\infty} \sum_{n=0}^{+\infty} f_{nm} \left(\phi_{nm} * \mathrm{PSF} \right) + n. \quad (5.3)$$

That is, the CHEF coefficients of the image convolved with the PSF coincide with the coefficients of the data without convolving, so it is enough to construct the model using these coefficients and the original basis (without convolution) to recover the deconvolved original data.

The process followed to test this method has consisted on convolving a simulated source with a PSF generated by TinyTim (see figures 5.1(b) and (a), respectively). Then, the convolved image (figure 5.1(c)) is modelled using the CHEF basis (figure 5.1(d)), which has also been previously convolved with the psf. The deconvolved image is recovered with these coefficients and the original CHEF basis. The obtained result and the residuals with regard to the original data (figure 5.1(a)) are displayed in figures 5.1(e) and (f), respectively.

However, this naive solution does not work well in practice because of several issues. Let us described them.

Mathematically, deconvolution is an ill-posed problem due where many solutions satisfy the equations, specially in the presence of noise (Bennia & Riad, 1990) and solutions are not stable at all since they depend strongly on the precision of the input data. Let us support this assertion mathematically to explain it. In the numerical sense, deconvolution in the time-domain can be seen as a differentiation operator (remember definition (5.1)), since it implies subtractions, specially in the case of discrete vectors instead of functions. Any tiny imprecision in the input data, that is, $f * g$ and g leads to great inaccuracies in the final estimation of f, due not only to the intrinsic instability of the raising of the problem but also to the rounding errors. Translating these operations into Fourier-domain does not happen to be a smart solution either, since convolution is transformed to a product in frequency domain:

$$\widehat{f * g} = \hat{f} \cdot \hat{g} \quad (5.4)$$

which involves a division to recover f and, therefore, the fast spreading of the initial errors. Finally, we cannot forget that due to bandwidth limitation of the waveform detector and the sampling, the acquired waveform is different to a certain extent from the true time signal, so the presence of this problem is unavoidable.

Another important problem in deconvolution is the appearance of some artifacts like ringing effects os spikes. Explanation of these latter is quite simple just having a look at the Fourier definition of convolution (5.4). The fact that signals or images are band-limited in the frequency domain introduces a great level of uncertainty when it comes to evaluate the deconvolution, since the small values in the data spectra are translated into sharp spikes in the deconvolved signal (Riad, 1986). Suppose $\widehat{f * g}$

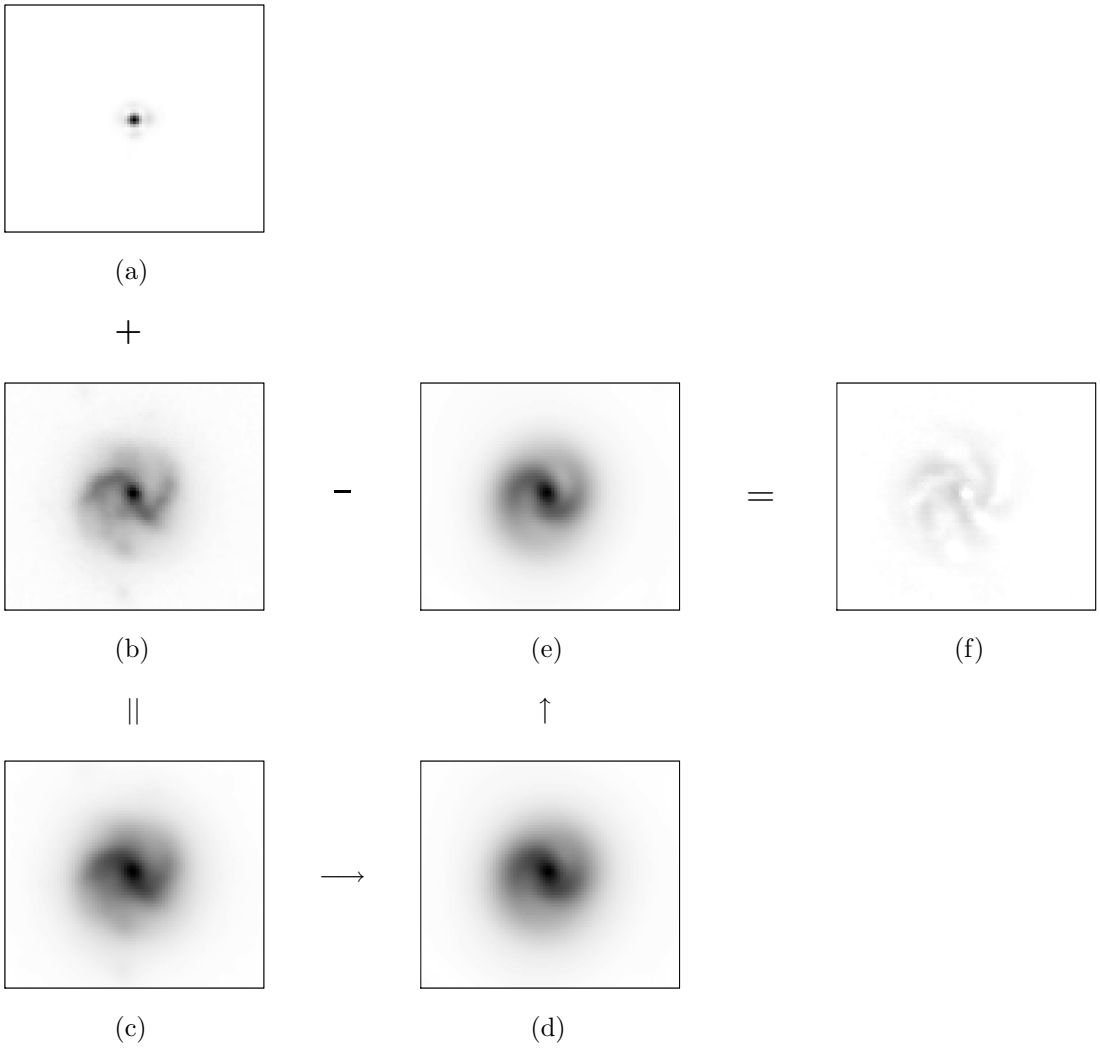

Figure 5.1 Outline of the process for the PSF deconvolution of real data: (a) PSF generated by TinyTim, (b) original source, (c) image convolved with the PSF, (d) CHEF model of the convolved image, (e) deconvolved image using CHEF original basis, and (f) obtained residual after subtracting the deconvolved model to the real image, in linear scale.

and $\hat{g}$ are realistically detected and sampled, using a bandlimited detector. From some point ν_0 on, registered frequencies will have amplitudes down to the noise level or even with a really low value (remember that Fourier coefficients decay due to the compactness of the basis), what means that the inversion required by deconvolution becomes extremely high:

$$\hat{f}(\nu) = \frac{\widehat{f * g(\nu)}}{\hat{g}(\nu)} >> 0, \quad \forall \nu > \nu_0 \tag{5.5}$$

That indicates that f is significantly composed by high frequencies with great amplitude, what it is translated into those spikes previously mentioned. This effect is usually reduced by filtering the final and spiky form of f, mostly based on Wiener theory (Nahman & Guillaume, 1981; Riad & Stafford, 1980), to reduce the noise that contaminates the transfer function.

To explain the other kind of artifacts, we will have to use the concepts developed in section 3.2.2 to prove the aliasing effect, but let us consider the one-dimensional case for simplicity. We can remember that expression (3.17) described how the spectra of a sampled signal coincided with the spectra of the continuous function where it came from, repeated periodically on the Fourier plane and summed at each frequency. Then, one period must be isolated and sampled, resulting in the Fourier transform of the digitized signal. This isolation is translated into a multiplication by a box function $B(\eta) = \begin{cases} 1 & \text{if } -\eta_0 \geq \eta \geq \eta_0 \\ 0 & \text{cc} \end{cases}$ in Fourier space, that is, a convolution in time domain by the inverse of this box function, which is:

$$\check{B}(x) = \int_{-\infty}^{\infty} B(\xi)\, \mathrm{e}^{i\xi x}\, d\xi = \int_{-\eta_0}^{\eta_0} B(\xi)\, \mathrm{e}^{i\xi x}\, d\xi = \frac{1}{ix}\, \mathrm{e}^{i\xi}\, x \Big]_{\xi=-\eta_0}^{\eta_0} = \frac{1}{ix} \left[\mathrm{e}^{i\eta x} - \mathrm{e}^{-i\eta x}\right] = \frac{2\sin(\eta x)}{x}. \tag{5.6}$$

If the original image has point sources (what is usual in astronomical data), which can be mathematical expressed as delta functions, after convolution they will be replaced by oscillatory function $\sin x/x$, and this is the origin of that ringing effect so commonly observed.

However, the lack of information in Fourier domain is not an absolute disadvantage. The sampling theorem points out the necessity of a band-limited input signal in order to properly reconstruct it from sampled data:

Theorem 5.1. *(Shannon, 1949) If a continuous function f contains no frequencies higher than a cutoff frequency ν, it is completely determined by giving its ordinates at a series of points spaced $\nu/2$ units.*

In real data is not really possible to determine clearly this cutoff frequency, since functions are seldom focused on a finite number of Fourier coefficients but they are spread all over the spectra. Because of that, in practice, ν is taken as the highest frequency at which the Fourier transform emerges from the noise (Magain et al, 1998). Moreover, data must be sampled in such a way that both the observed image and the deconvolved one obey the sampling theorem. Observing instruments are usually built obeying this sampling theorem, under average observing conditions. A typical rate of $\sim$ two sampling intervals per FWHM of the PSF is encountered, what often works for low S/N images.

In order to make the deconvolved signal obey the Shannon theorem too, we have chosen the solution proposed by Magain et al (1998); according to this, the sampled signal will not be deconvolved by the total PSF (PSF^{orig}) but by a narrower function h specially selected so that the resolution of the deconvolved image is compatible with the adopted sampling rate, since it will be convolved with its own PSF (PSF^{final}). So, these three functions will be related by:

$$PSF^{orig} = PSF^{final} * h, \tag{5.7}$$

and the purpose is recovering $f * PSF^{final}$, which will not be exactly the original image f (what is impossible, according to the sampling theorem) but a similar version of it, avoiding in this way spikes and ringing effects common to the traditional deconvolution methods. The way to choose PSF^{final} is arbitrary, just taking into account that equation (5.7) must admit a solution. In our case, we have designed it to be equals to the original PSF^{orig} but much narrower, with a width of two pixels.

Finally, it is also observed that the size of the frame surrounding the convolved source must be inversely proportional to the source radius, if this latter is much smaller than the PSF radius. This is quite reasonable, since the discrete convolution introduces some artifacts in the convolved image, due to the "fake"values added in the surroundings of the original image by different techniques (periodically, specularly or by zero-padding).

5.2. Gaap aperture fluxes

The estimation of the estructural parameters is a crucial task in galaxy evolution. It is necessary to classify galaxies into different types, which has strong implications on their origin and evolution. The shear estimation is also basic for gravitational weak lensing and, therefore, the discovery of the composition of the Universe and the identification of the dark matter.

As stated above, one of the main motivations to develop the CHEF basis is having a tool to automatically measure accurate fluxes and shapes in the context of large galaxy surveys. Analytical formulae to calculate different morphological parameters were showed in section 3.2.1 , particularly, for flux and ellipticity. However, it must be noticed that they have been developed both in complex and real approaches of the CHEF bases, but not for the discrete case. It is trivial translating integrals and infinite intervals in expressions (2.47), (3.8), (3.12) and (3.13) into sums and bounded image frames, but, how longer are these approximations accurate in practical implementation? To answer this question, an exhaustive test was performed, by applying CHEFs on a sample of more than 350 mock galaxy profiles displaying different morphologies and characteristics. Both the flux and the ellipticity of the models created by CHEFs and measured by the formulae displayed in (3.7) and (3.14) were calculated and compared to the original ones. Results and a deeper explanation of the test can be found in chapter 4, where the test is also applied to shapelets algorithm, to compare the reliability of both methods (see figures 4.3 and 4.4).

Despite the good performance of this "direct"method, it is instructive to explore other approaches, as the one described by Kuijken (2008), who does not compute the usual flux parameter, but the so named *GaaP* much more consistent and adapted to the shape of the functions used in the galaxy analysis, in this particular case, shapelets. This approach is specially well adapted to astronomical surveys with varying PSF, since it estimates the fluxes of an homogeneous PSF for all filters.

The *Gaussian-aperture-and-PSF* (GaaP), F_q of aperture q is defined as the Gaussian-weighted flux of the source, if this was observed with a Gaussian PSF of the same width as the weight function (Kuijken (2008)):

$$F_q \equiv \iint f(r') \, \frac{\mathrm{e}^{-(r-r')^2}/2q^2}{2\pi q^2} \, \mathrm{e}^{-r^2/2q^2} \; dr \; dr' = \frac{1}{2} \int f(r) \, \mathrm{e}^{-r^2} \, 4q^2 \, dr. \tag{5.8}$$

where f represents the light distribution of the galaxy. The last step shows how this way of measuring the flux is equivalent to calculating the weighted flux of f with a Gaussian weight function of dispersion $\sqrt{2}q$.

The selection of this formula for flux is not arbitrary; in fact, the author in Kuijken (2008) decides to weight the parameter using a Gaussian because the intention is to later represent the source by means of shapelet functions, which are composed by Hermite polynomials and Gaussians (see section 2.2). In fact, using expressions (2.1) and (2.2) to represent the f function in (5.8) and changing coordinates from polar to cartesian, the integral can be separated in x and y:

$$F_q = \sum_{m,n} f_{m,n} F_q^m F_q^n \tag{5.9}$$

with

$$F_q^a = \frac{1}{2} \int \mathrm{e}^{-x^2/4q^2} \, \frac{H^a(x/\beta) \, \mathrm{e}^{-x'^2/2\beta^2}}{\sqrt{\sqrt{\pi} 2^a a! \beta}} = \frac{\pi^{1/4} \beta^{1/2}}{\sqrt{1 + \beta^2/2q^2}} \sqrt{\frac{(a-1)!!}{a!!}} \left(\frac{2q^2 - \beta^2}{2q^2 + \beta^2} \right)^{a/2}, \tag{5.10}$$

where H^a represents the Hermite polynomial of order a, β is the shapelet scale, and the operator !! is recursively defined by $0!! = 1!! = 1$ and $n!! = n(n-2)!!$.

In our case, we have developed an analogous procedure firstly resolving the indefinite integral (5.8) and later applying the integration limits, but decomposing the function f using CHEF basis; so,

replacing (2.24) into (5.8) it yields:

$$\begin{aligned} F_q &= \frac{1}{2}\int_0^{+\infty}\int_{-\pi}^{\pi} \mathrm{e}^{-r^2/4q^2} \sum_{m=-\infty}^{+\infty}\sum_{n=0}^{+\infty}\left(f_{n,m}TL_n(r)\,\mathrm{e}^{im\theta}\right)\,dr\,d\theta \approx \pi\sum_{n=0}^{+\infty} f_{n,0}\int_0^R \mathrm{e}^{-r^2/4q^2}\,TL_n(r)\,dr = \\ &= \frac{\pi}{2}\sum_{n=0}^{+\infty} f_{n,0}\left[\underbrace{\int_0^R \mathrm{e}^{-r^2/4q^2}\,\mathrm{e}^{in\arccos\left(\frac{r-L}{r+L}\right)}\,dr}_{I_a} + \underbrace{\int_0^R \mathrm{e}^{-r^2/4q^2}\,\mathrm{e}^{-in\arccos\left(\frac{r-L}{r+L}\right)}\,dr}_{I_b}\right] \end{aligned} \tag{5.11}$$

Let us calculate these two last integrals separately. We will solve the first one by parts:

$$I_a = q\sqrt{\pi}\,\mathrm{erf}\left(\frac{r}{2q}\right)\mathrm{e}^{in\arccos\left(\frac{r-L}{r+L}\right)} + q\sqrt{\pi}in\int \mathrm{erf}\left(\frac{r}{2q}\right)\mathrm{e}^{in\arccos\left(\frac{r-L}{r+L}\right)}\sqrt{\frac{L}{r}}\frac{1}{r+L}\,dr \tag{5.12}$$

where erf is the error function (Abramowitz & Stegun (1970)), whose McLaurin series expansion is:

$$\mathrm{erf}\,z = \frac{2}{\pi}\sum_{i=0}^{\infty}\frac{(-1)^i z^{2i+1}}{i!(2i+1)}, \tag{5.13}$$

which can be replaced into integral I_1 to apply the method of integration by parts:

$$\begin{aligned} I_a &= \frac{2}{\pi}\sum_{i=0}^{\infty}\frac{(-1)^i}{(2q)^{2i+1}i!(2i+1)}\int r^{2i+1}\,\mathrm{e}^{in\arccos\left(\frac{r-L}{r+L}\right)}\sqrt{\frac{L}{r}}\frac{1}{r+L}\,dr = \\ &= \frac{2}{\pi}\sum_{i=0}^{\infty}\frac{(-1)^i}{(2q)^{2i+1}i!(2i+1)}\left[\frac{-1}{in}r^{2i+1}\,\mathrm{e}^{in\arccos\left(\frac{r-L}{r+L}\right)} + \frac{2i+1}{in}\int r^{2i}\,\mathrm{e}^{in\arccos\left(\frac{r-L}{r+L}\right)}\,dr\right]. \end{aligned} \tag{5.14}$$

Integral I_b is evaluated analogously, so it yields:

$$I_b = \frac{2}{\pi}\sum_{i=0}^{\infty}\frac{(-1)^i}{(2q)^{2i+1}i!(2i+1)}\left[\frac{1}{in}r^{2i+1}\,\mathrm{e}^{-in\arccos\left(\frac{r-L}{r+L}\right)} - \frac{2i+1}{in}\int r^{2i}\,\mathrm{e}^{-in\arccos\left(\frac{r-L}{r+L}\right)}\,dr\right]. \tag{5.15}$$

And finally, replacing (5.14) and (5.15) into (5.11), it is obtained

$$\begin{aligned} F_q &= \pi\sum_{n=0}^{+\infty} f_{n,0}\left[q\sqrt{\pi}\,\mathrm{erf}\left(\frac{r}{2q}\right)TL_n(r) + \right. \\ &\quad \left. +2\sum_{i=0}^{+\infty}\frac{(-1)^i}{(2q)^{2i+1}i!(2i+1)}\left(-r^{2i+1}TL_n(r) + (2i+1)\int TL_n(r)r^{2i}\,dr\right)\right]. \end{aligned} \tag{5.16}$$

Note once the integration limits are applied to this result, the last integral becomes the generic one calculated in section 2.3.4, by means of the hypergeometric function, according to expression (2.46).

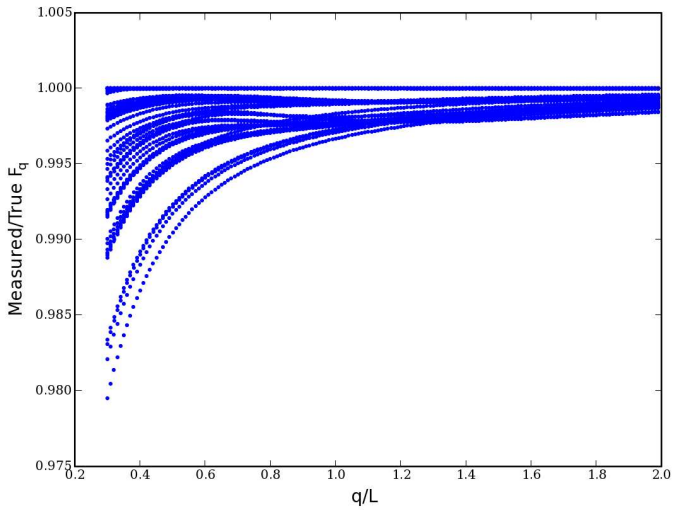

Figure 5.2 Relative error obtained for GaaP flux using method described in Kuijken (2008).

Then, for $R > 0$,

$$\begin{aligned} F_q \equiv \frac{1}{2}\int_0^R f(r)\,\mathrm{e}^{-r^2}\,4q^2\,dr = \pi\sum_{n=0}^{+\infty} f_{n,0}\left[q\sqrt{\pi}\,\mathrm{erf}\left(\frac{R}{2q}\right)TL_n(R) + 2(-1)^{n+1} + \right. \\ \left. +2\sum_{i=0}^{+\infty}\frac{(-1)^i}{(2q)^{2i+1}i!(2i+1)}\left(-r^{2i+1}TL_n(r) + (2i+1)I_n^{2i}\right)\right] \end{aligned} \tag{5.17}$$

Results after applying this last formula to a sample of simulated galaxies with different Sérsic indices and ellipticity parameters, can be observed in figure 5.2. This figure can be compared with figure 2 in Kuijken (2008): the observed error is much lower in CHEFs for steep objects, that is, those ones with a small Sérsic index, whereas for more extended sources the error decreases and seems to converge to one, just the opposite of what happens with shapelets. That is perfectly reasonable, since as it was stated previously, shapelets are not able to describe with the same precision both bulge and disk of the galaxies, so for not very compact sources wings are not properly modeled and flux estimation becomes poorer.

In relation to the flux estimation technique presented in chapter 4 by means of the analytical formula (3.7), this GaaP method has proved to obtain less accurate results, although it is easier to implement. For these reasons, we highly recommend the use of the former to obtain accurate photometric results.

5.3. Shear estimation by least square minimization

The one described in previous section is not the only method we have implemented to measure flux and shear using the CHEF decompositions. Another approach, proposed in Kuijken (2006) for shapelets bases was adapted to CHEFs. In this paper, observed image is decomposed using three different operators: the one in charge of convolving with the PSF, the shear operators responsible of the ellipticity of the object and the one which yields the shapelet model of the real galaxy. This decomposition can be then expressed as a composition of these three operators, the last two being a linear combination of others. The method prposed by Kuijken consists on estimating the optimal coefficients of these linear combinations using a least square minimization and, therefore, the ellipticity parameters are obtained (they match the coefficients of the linear combination in the shear operator). We will devote the following paragraphs to develop a similar method for CHEFs, but without attempting any deconvolution, to test the actual reliability of the technique.

Let us note the first order shear operators in the x axis and the $y = x$ line as S_1 and S_2 respectively, that is:

$$S_1 = \begin{pmatrix} 1 & 0 \\ 0 & -1 \end{pmatrix} \qquad S_2 = \begin{pmatrix} 0 & 1 \\ 1 & 0 \end{pmatrix}. \tag{5.18}$$

being S_1 in charge of the ellipticity along the x-axis and S_2 the one which produces the ellipticity in the $y = x$ line.

Then, using expression (2.24) again, any sheared source f^{shear} can be represented in the following way:

$$f^{shear} = (1 + e_1 S_1 + e_2 S_2) f = (1 + e_1 S_1 + e_2 S_2) \left(\frac{1}{C\pi} \sum_{m=-\infty}^{+\infty} \sum_{n=0}^{+\infty} f_{n,m} TL_n(r) e^{im\theta} \right). \tag{5.19}$$

Fitting this model to the observed source yields the best-fit ellipticity parameters (e_1, e_2) as well as the coefficients for the decomposition of the same source with spherical shape, that is, the original one before being sheared. This minimization has been performed using the Levenberg-Marquardt algorithm (Levenberg (1944)), and the obtained results can be observed in figure 5.3, where the relative errors for both ellipticity parameters in the $y = 0$ and $y = x$ directions are displayed.

As it can be observed, with this method the shear parameter along the first bisector is not well estimated, while the one along the x axis yields better results. However, CHEF basis are totally isotropic, so it can be concluded that they are not responsible of this bias, but the minimization algorithm which first optimize the e_1 parameter and later the e_2 (see equation (5.19)). For this reason, as well as the better results it yielded, the method based on analytical formulae described in the previous section is obviously a better option than this one.

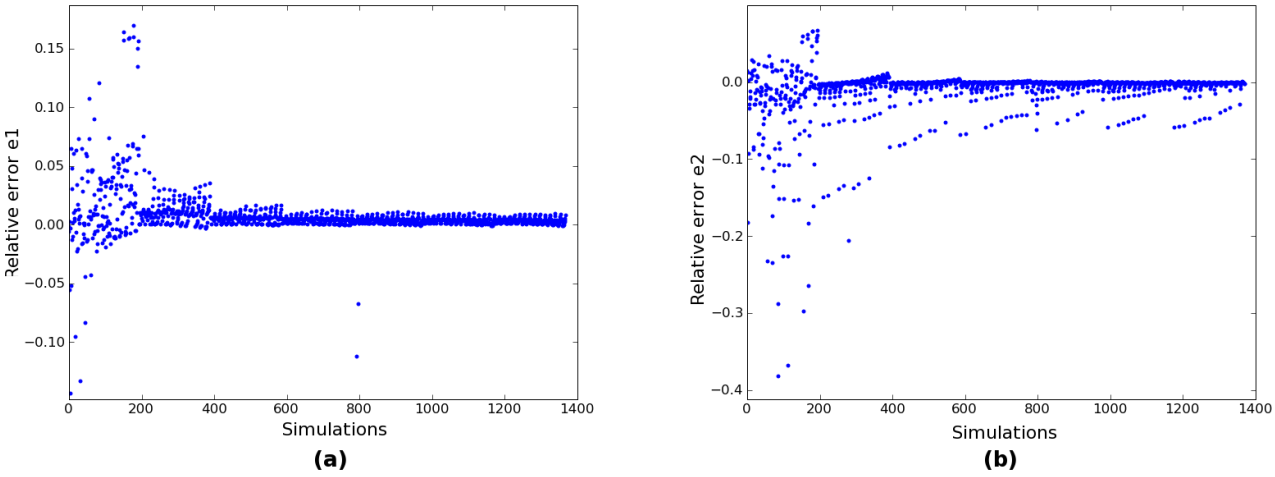

Figure 5.3 Relative errors obtained for both ellipticity parameters e_1 and e_2 using least square minimization method.

5.4. Image simulation

Galaxy simulation is an extremely powerful and useful tool to test and calibrate the effectiveness of many image analysis and detection methods. For example, it has been used to test weak shear estimation techniques (Heymans et al., 2006; Bridle et al., 2009; Schrabback et al., 2009), to determine the accuracy and loss of precision in compression-decompression (codec) algorithms (Bernstein et al., 2009) or in specific mission development, to optimize the optical design and observation strategies, for instance, for ESA's cosmic visions candidate Euclid (Refregier et al., 2010) or NASA/DOE Joint Dark Energy Mission concepts (Jelinsky et al., 2006; High et al., 2007).

For this reason, several packages have been developed to create large catalogues of mock galaxies. Some of the most remarkable ones are Skymaker (Erben et al., 2001; Bertin, 2009), which uses a de Vaucouleurs profile to simulate elliptical sources plus an exponential disk in the case of spirals, Artdata from IRAF, the method by Bouwens et al. (1998a,b) to reuse well-resolved galaxies from HDF, or Skylens (Meneghetti et al., 2008) based on shapelets decompositions as well as the works described by Massey et al. (2004), Ferry et al. (2008), and Dobke et al. (2010). Many of these works could just faithfully reproduce deep ground-based data, whereas current and future surveys require the imitation of deep space-based galaxies too, with more complex resolved features.

A complete and detailed catalogue of mock data requires a wide set of galaxies displaying every type of morphologies, ranging from the simple ellipticals to those ones with more complex features (spiral arms, bars, mergers, dust lanes, knots). In addition, to make the simulations more realistic, every instrumental effect must be convenient and carefully modeled, adequating the pixel scale size to the model, convolving it with the proper PSF, or adding noise with the type and the level adapted to the final sample. Our method consist basically on elaborating models of real images from the UDF

(Beckwith et al., 2004) and storing the coefficients in a catalogue of artificial data. These models are then provided with all the physical characteristics desired for the output image. Let us outline an scheme of the followed process:

1. *Elaboration of the catalogue.* The whole UDF field is processed using CHEFs, according to the algorithm described in section 3.1.

2. *Storing of the models.* The number of coefficients N^{max} and M^{max} needed for each one of the detected sources, the estimated morphological characteristics of the objects (flux and ellipticity parameters), the scale size values L, and the centroid (x_c, y_c) are stored in a simple ASCII catalogue. Another file is created to save the coefficients of each one of these models, easily accessible by the running number associated to them. Note that these models are noise-free as well as they faithfully reproduce the fine features in the galaxies, thanks to CHEF functions high reliability.

3. *Selection of the models.* A certain number of CHEF models are randomly selected from the mock catalogue, according to the galaxy density of the output field where these galaxies are desired to be inserted.

4. *Evaluation of the models.* A grid with pixel size equals to the one displayed in the output field is built, and the chosen models are evaluated on it (by means of the CHEF coefficients previously stored, as it was aforementioned). In this way, resulting models are pixellated to the correct resolution.

5. *Zero-point correction.* Zero-point correction is applied to the CHEF models, in order to make magnitudes be coherent with the ones of the real sources of the output field:

$$f^{zp} = f^{orig} \cdot (10^{(zp_{out} - zp_{UDF})}/2{,}5)) \tag{5.20}$$

6. *PSF convolution.* The pixellated, corrected model is convolved with the PSF of the output image, to make it be blurred in same level that the other sources present in the field. This discrete convolution is performed in the frequency space by means of the Fast Fourier Transform, which is much more reliable and fast than the usual in the time domain:

$$f^{zp} * PSF = IFFT(FFT(f^{zp}) \cdot FFT(PSF)) \tag{5.21}$$

   where FFT and $IFFT$ denotes the direct and inverse Fast Fourier transforms, respectively.

7. *Selection of the location.* Centers of the models in the output image are randomly selected all over the field, just avoiding location too near the edges to completely set the models inside the frame (otherwise, morphological parameters as flux or ellipticity would have no sense and these mock objects would be useless to calibrate any method).

8. *Noise adding.* Pixellated, corrected and convolved models are inserted into their chosen locations in the image. This guarantees the resulting sources will display the same type and level than the

output field, without having to simulate artificial noise for them.

This method was applied to ALHAMBRA (Benítez et al., 2009) observations as a way of calibrating the effects of the ground-based observation effects into the estimation of the morphological and photometric parameters of the galaxies. By way of illustration, some artificial galaxies has been added to an ALHAMBRA field and are shown in figure 5.4, totally adapted to the physical e instrumental characteristics of this survey.

5.5. Large surveys

One of the major advantages of CHEFs is the implementation of the whole pipeline and their ability to work with a minimum of interactivity from the user. As it was explained in detail in section 3.1, the only inputs for the code are the image to be processed and the maximum number of Chebyshev and Fourier coefficients allowed to compute, that is, N^{max} and M^{max}. Taking into account that these two parameters can be easily determined in an automatic way using a criterium related to the size (the bigger the image is, the larger N^{max} and M^{max} must be chosen, under the same level of noise), the whole process can be automatized, so it is ideal for large survey processing. In fact, the full pipeline has already been applied to some fields from ALHAMBRA survey. ALHAMBRA is characterized by the use of 23 different filters, in such a way that CHEFs can find the best combination of the number of coefficients N and M just for the first filter and then apply this choice to the other 22, without having to optimize these parameters again. That results in an even faster velocity and efficiency of the computations, which can be reduced by a factor of 4. This was the strategy followed to process the object displayed in figure 5.5, which is repeated in the 20 optical filters available for ALHAMBRA. The one in the upper left corner was the one fully analyzed, and the optimal combination of N and M resulting for it was later applied to the other 19. Results can be observed in figures 5.6 as well as the obtained residuals in figure 5.7. We determine this method is accurate enough and there is no difference between the fully processed object and the others. A comparison between the radial flux profiles of both the original sources and the CHEF models is displayed in figure 5.8, in order to show the accuracy of the method fitting the wings of the galaxy and, therefore, measuring the photometry of the objects in the survey.

5.6. Galaxy cluster modeling

The study of dark energy and dark matter distribution in the Universe and their nature is one of the main goals of Astrophysics and, particularly, Cosmology, in the last years. Several indirect methods have been developed to study them, with gravitational lensing as one of the most successful ones. The distortion and bending of the light produced by huge concentrations of mass allows the researchers to invert the mass distribution models and determining the topology of dark matter in those areas. In particular, the analysis and measurement of lensing arcs appearing in clusters is a great source of information for this models. For this purpose, is absolutely necessary to subtract the main galaxies in the clusters, not only to uncover the arcs behind them, but also to properly estimate the photometry of them, eliminating the influence of these huge sources. However, the fact that galaxies in a cluster are

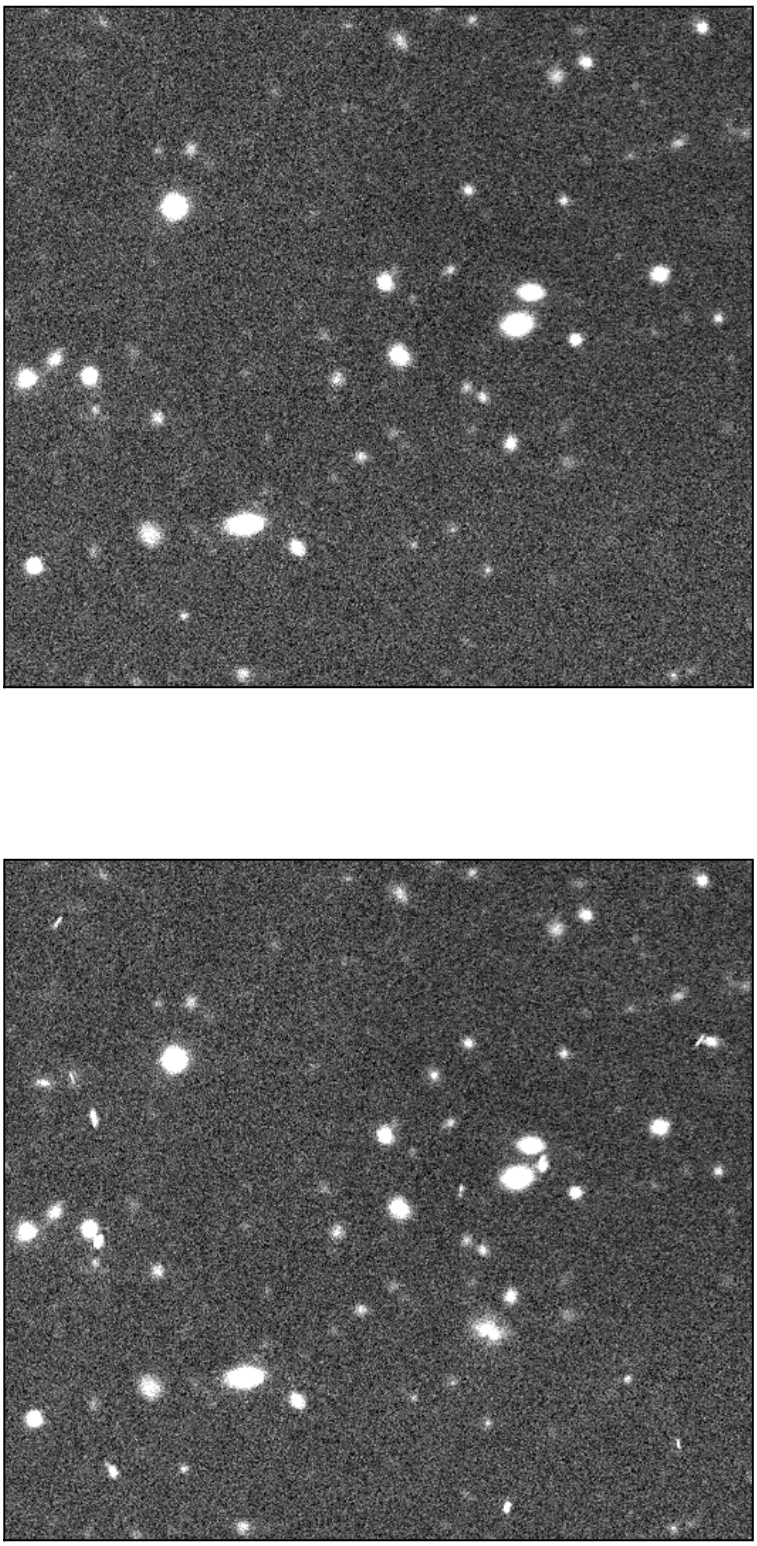

Figure 5.4 Frame extracted from a field observed by ALHAMBRA, where 15 different sources, randomly selected from UDF and artificially modeled to display the ALHAMBRA observational characteristics, have been inserted.

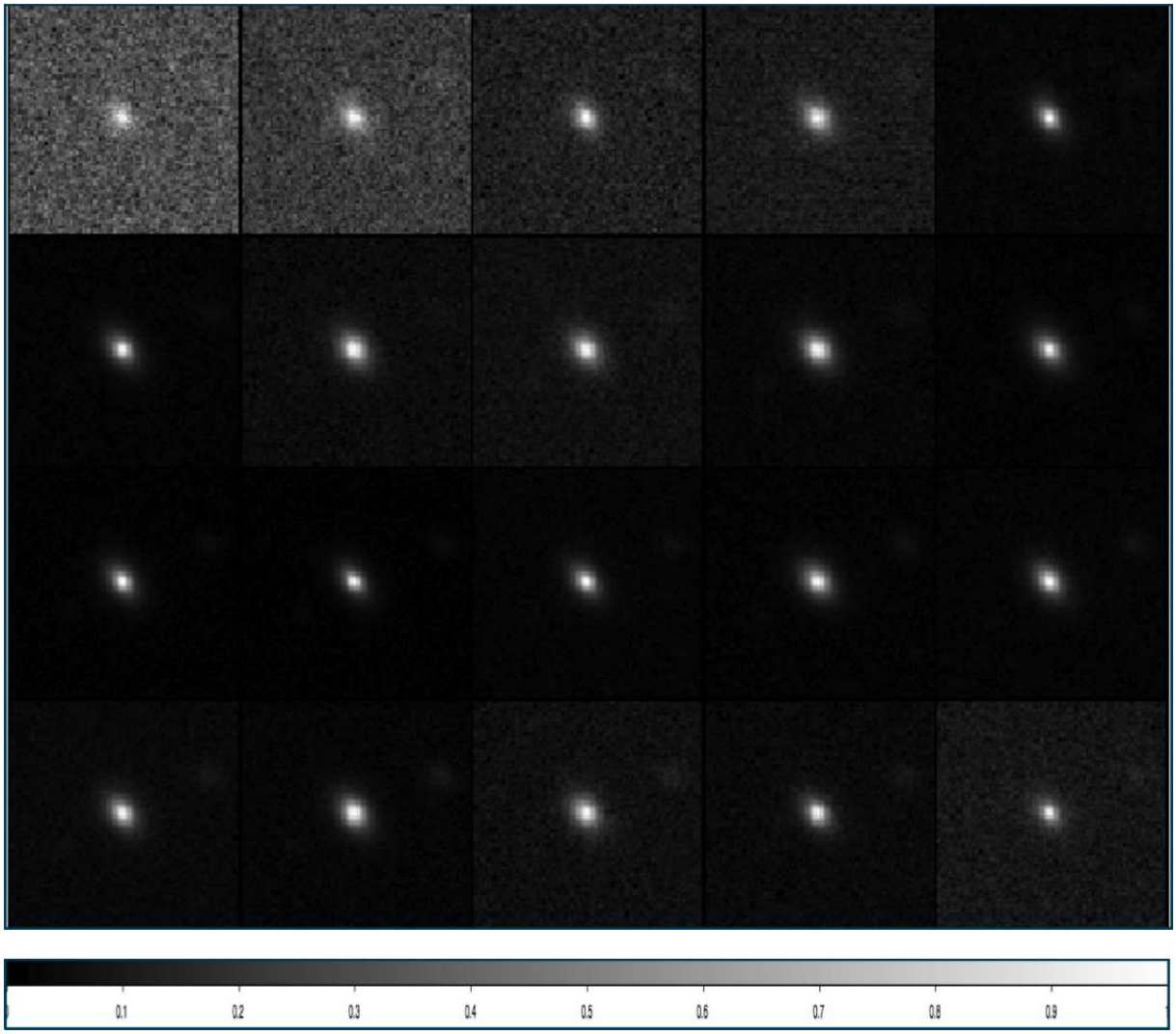

Figure 5.5 Galaxy extracted from ALHAMBRA survey in the 20 optical bands.

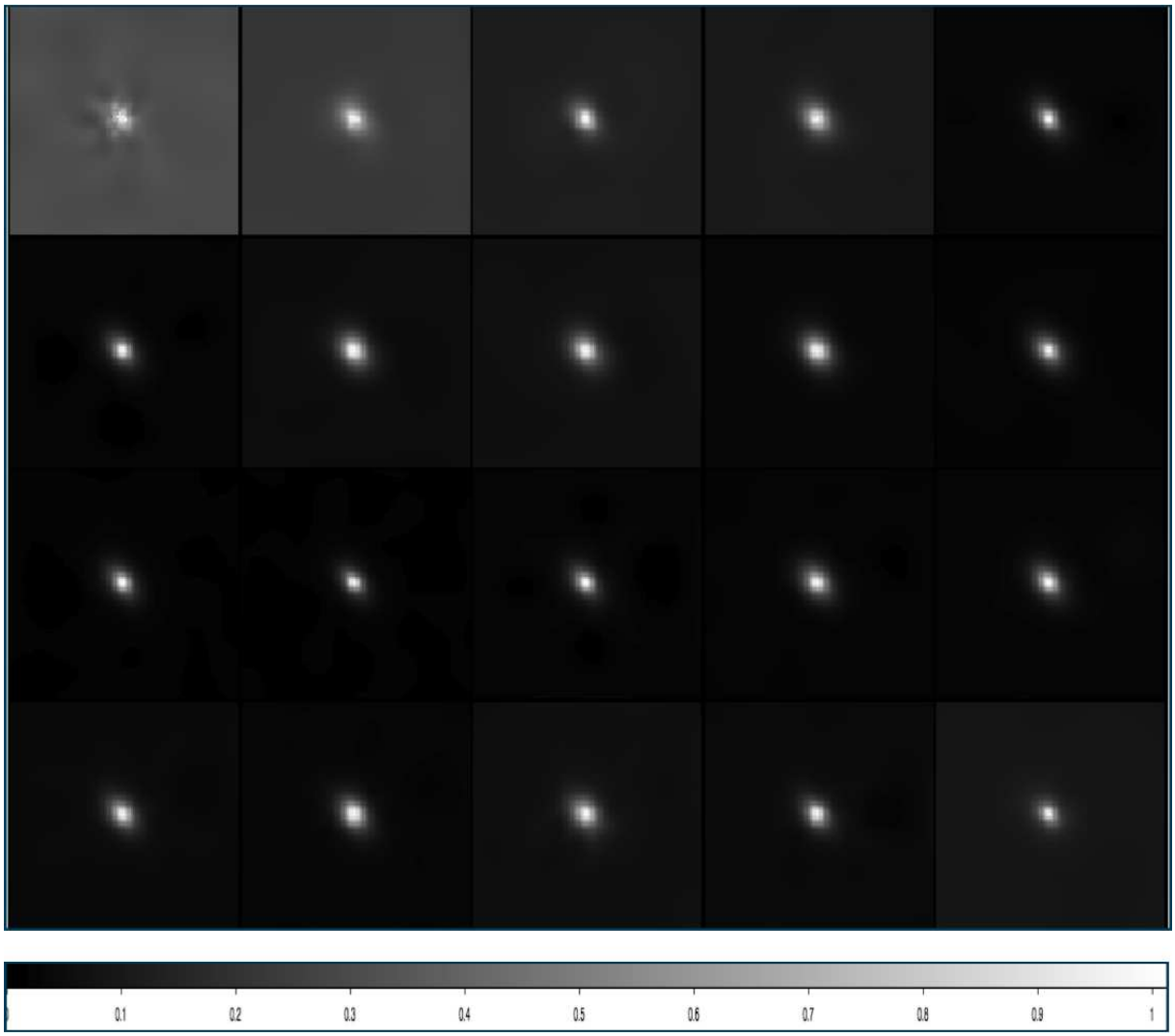

Figure 5.6 Results of the CHEF processing of the objects in figure 5.5. The object in the upper left corner is the one which the fully CHEF pipeline was applied to, whereas the other 19 used the optimizations found for the former.

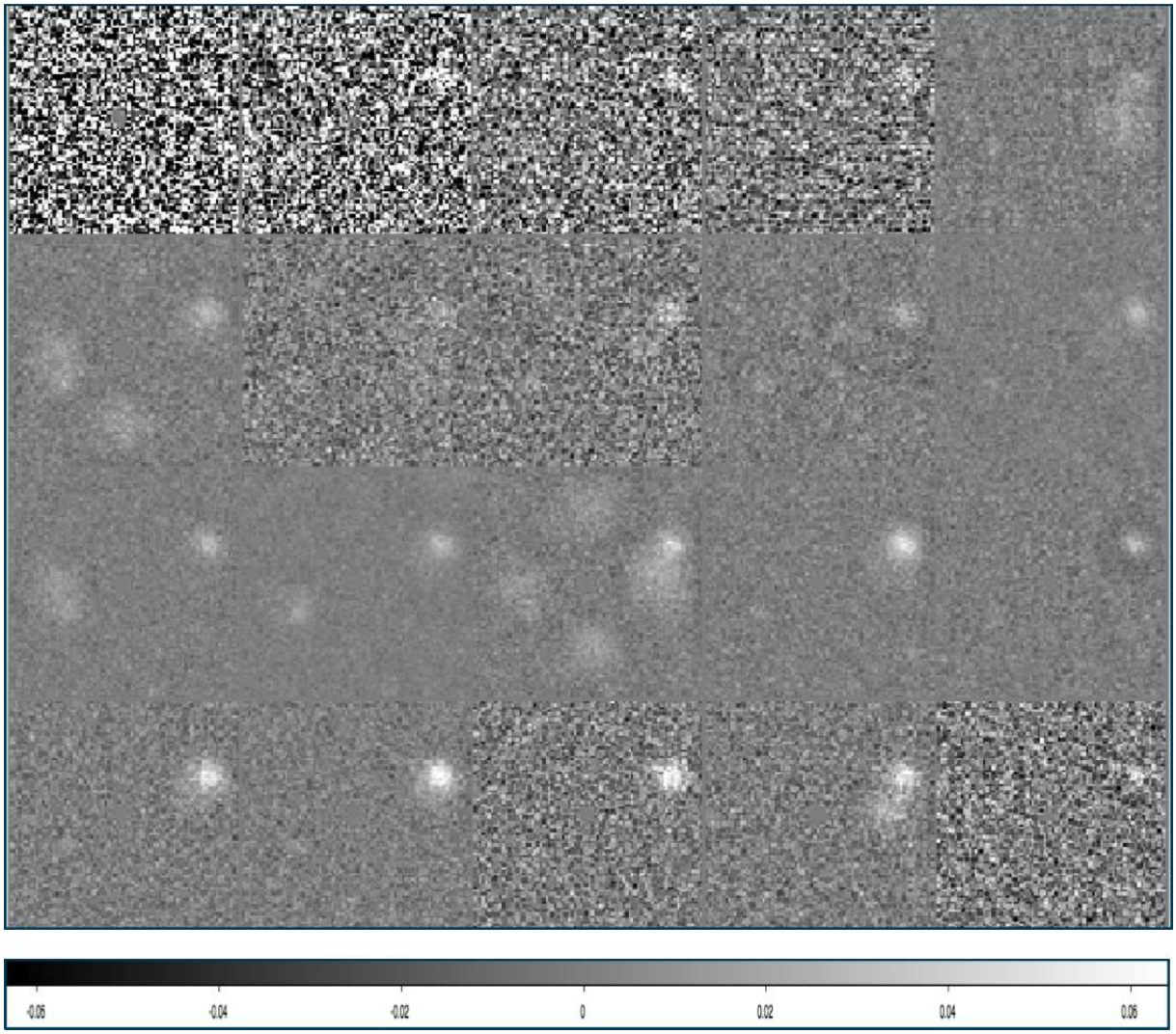

Figure 5.7 Obtained residuals for CHEF processing of galaxy in figure 5.5.

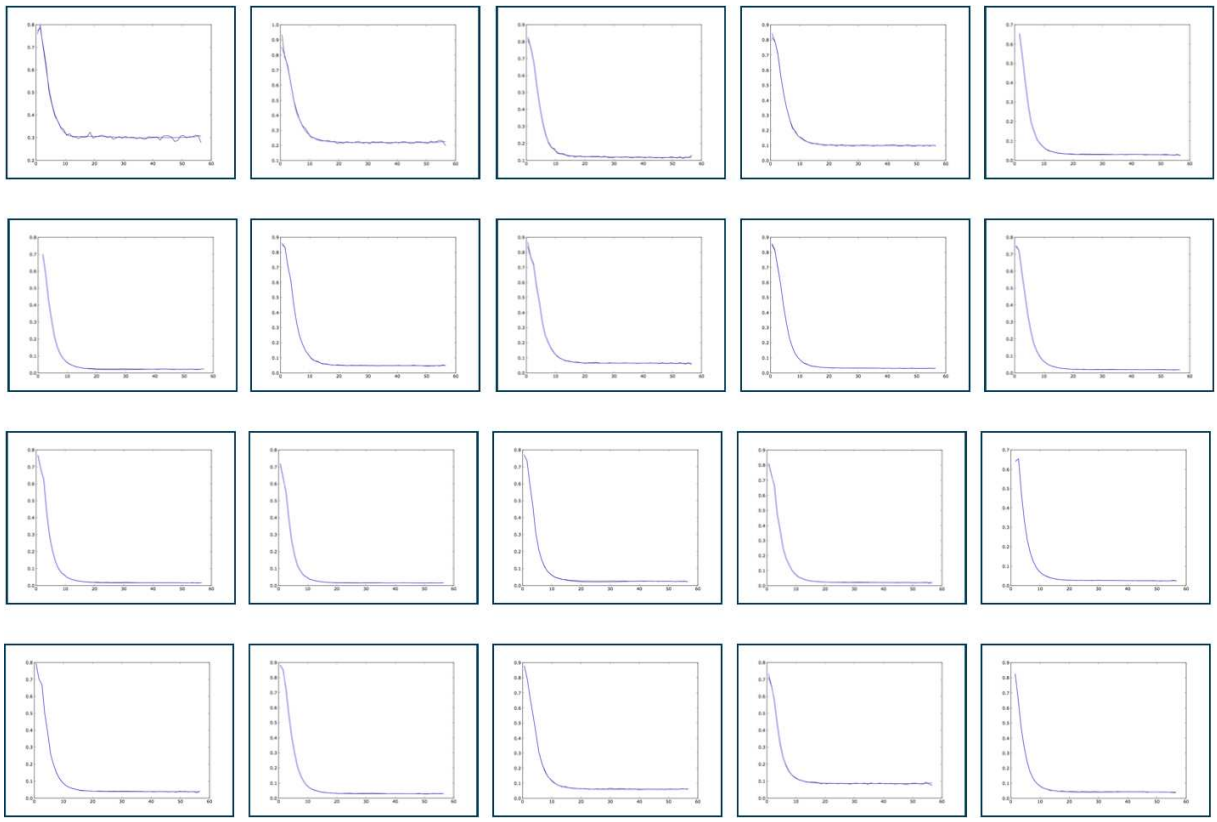

Figure 5.8 Radial flux profiles of both the original object in figure 5.5, and the corresponding CHEF models in figure 5.6.

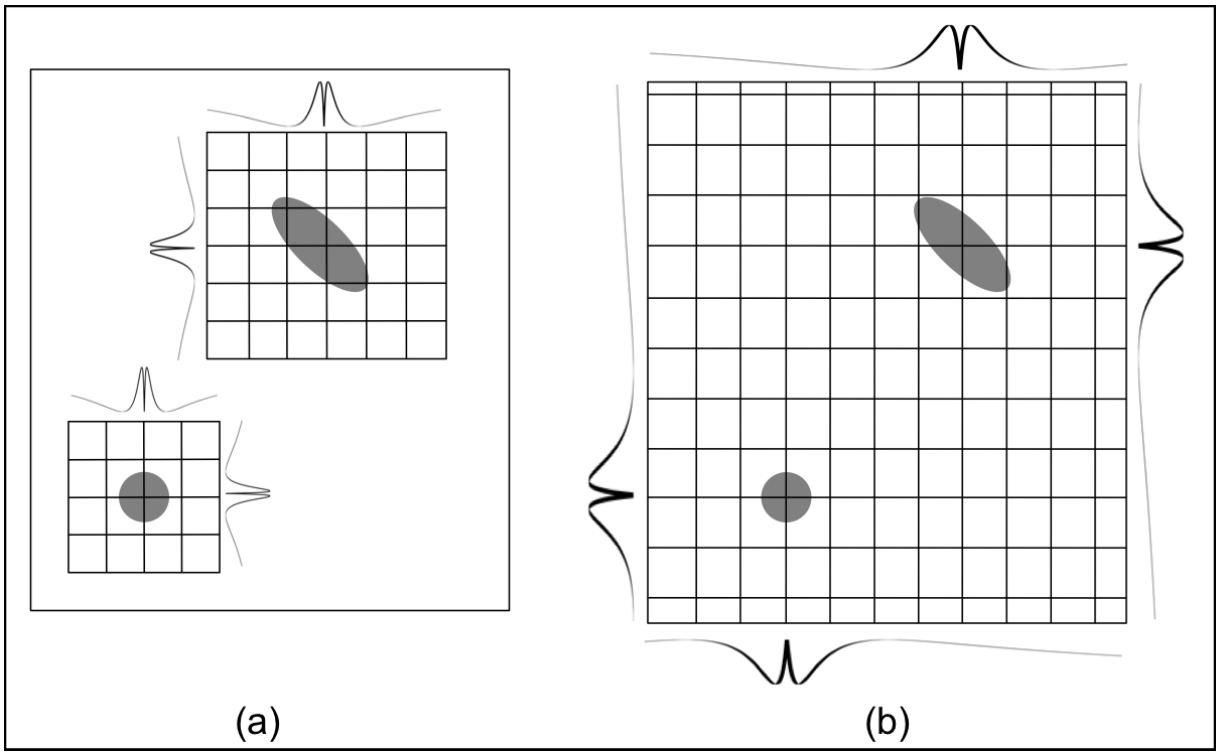

Figure 5.9 Different CHEF processing approaches: a) for single and far enough sources that can be isolated, and b) for cluster galaxies with overlapping wings. In the second case, two different sets of CHEF bases are evaluated with origin at different points of the grid, and the resulting CHEF basis is the composition if these two.

overlapping makes this task really hard, since it is not able to isolate them within individual frames and, in addition, the must be processed simultaneously, since light from the extended wings of each one of them is affecting to the neighbours.

Because of that, a totally different strategy has been developed for cluster processing. Instead of creating a simple grid with origin on the center of each galaxy and the later simple evaluation of the CHEF basis on it, we have proposed to create a composed large grid containing all the objects to be analyzed simultaneously, and matching each one of the centers with some node on the grid. A composed CHEF basis, joining the different simple CHEF basis centered on each galaxy, is built, and the orthonormalization process described in section 3.2.3 is applied to the whole set. We thus obtain a "multi-objectÇHEF basis (see figure 5.9 to observe a visual explanation of the process).

This method has been successfully applied to different real clusters. That is the case of Abell 1703, (see figure 5.10), where several galaxies from the central area of the cluster were subtracted to later analyze the lensing arcs surrounding them (Zitrin et al., 2010).

In addition, this subtraction technique has been also applied to both simulated to real data from Cluster Lensing and Supernova Survey with Hubble (CLASH) (Postman et al, 2011). The main goal

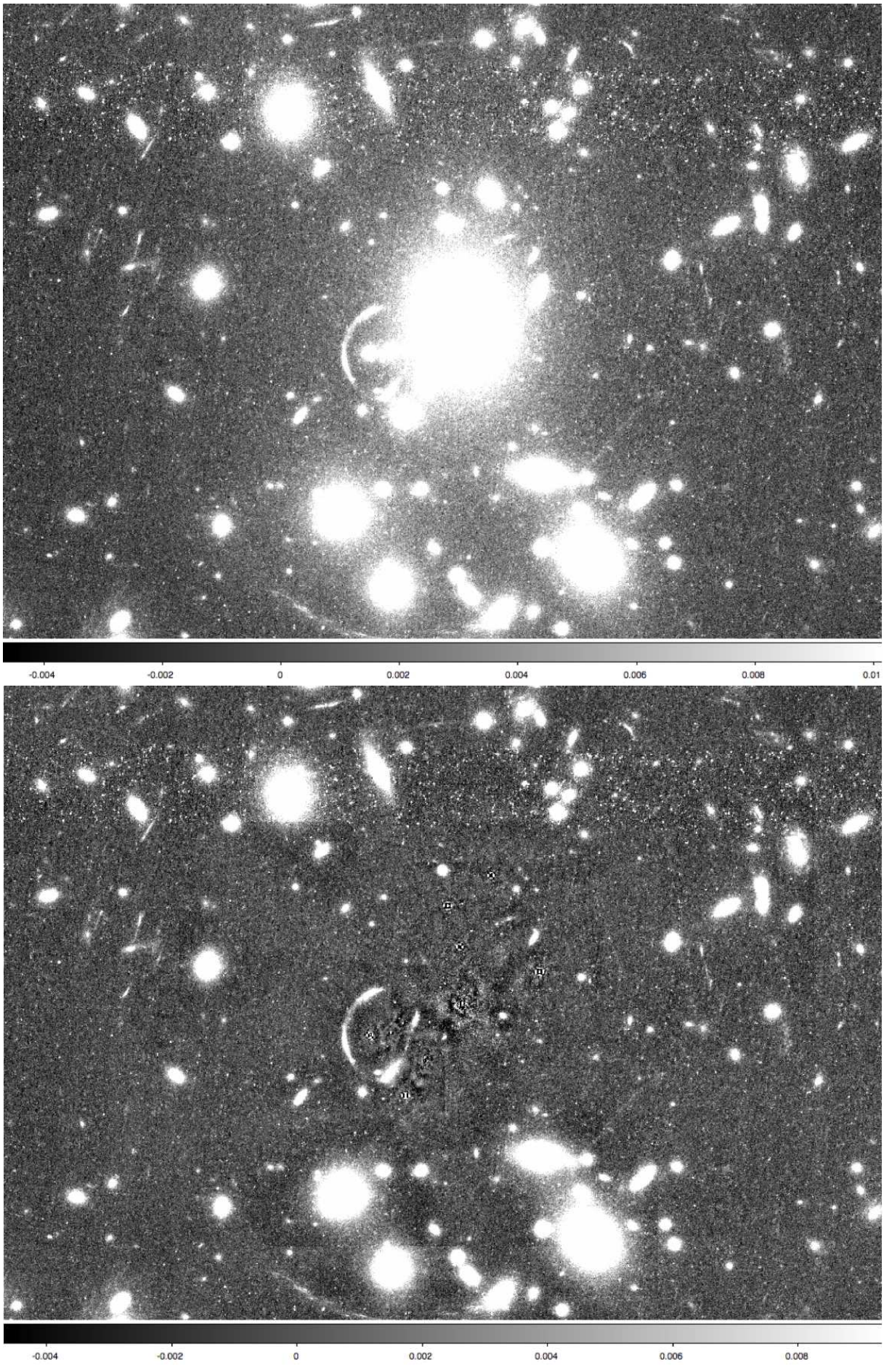

Figure 5.10 Abell 1703 cluster frame (top panel) and residuals after extracting the main galaxies of the cluster (bottom panel). Please note that the lensing arcs can be easily measured after the subtraction of these overlapping sources.

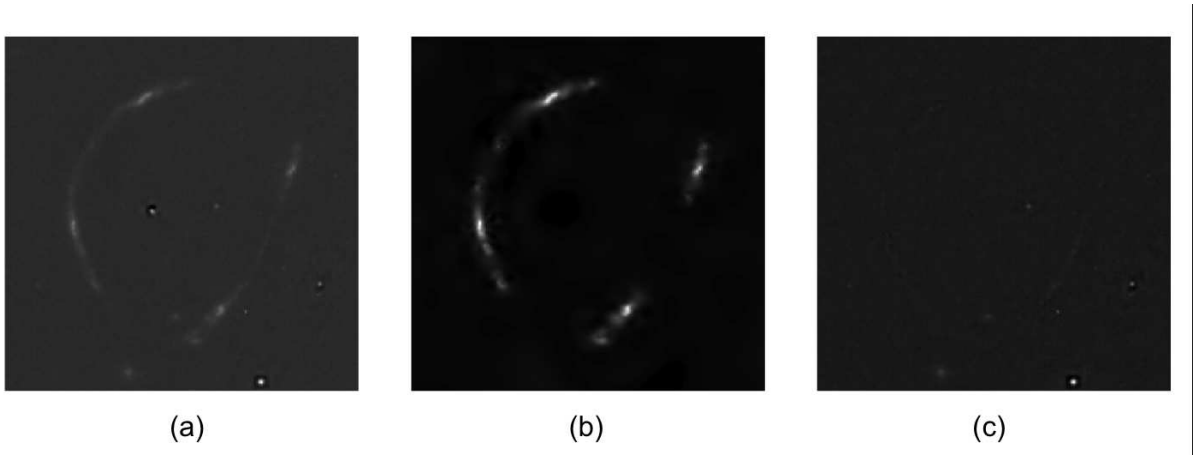

Figure 5.11 CHEF processing of two real lensing arcs from Abell 1703: a) original arcs, b) CHEF model of the arcs, c) obtained residuals in linear scale.

of this project is unveiling the dark matter mass distribution in the Universe by observing 25 massive intermediate redshift galaxy clusters. A total number of 524 orbits from Hubble Space Telescope will be devoted to this purpose, which will also be used to detect type-Ia supernovae (SNe Ia) in the redshift range $1 < z < 2$. The first images were available on November, 2010 and CHEF subtraction algorithm has begun to be applied to them.

Finally, it must be remarked that CHEF bases are so flexible due to their orthogonality and the efficiency of Chebyshev rational functions in modeling profiles, that they have been tried not only on galaxies but also on lensing arcs. The aim would be measuring the photometry of the arcs using just CHEF coefficients, by means of the expression (3.7), what would yields a much accurate estimation of flux in this arc objects. A quick test was performed using the uncovered central arcs in cluster Abell 1703, and the obtained results, which can be observed in figure 5.11 although not definitive, look really promising.

5.7. Conclusions

In this chapter, we have shown the reliability of CHEF bases for many other applications apart from the creation of morphological models or the image denoising. The PSF deconvolution is the first one we have dealt with, proving that it can be easily performed in theory due to the linearity of both the convolution operation and the CHEF bases. However, all the hurdles the deconvolution task present are taken into account and the final solution we have found to overtake them is to deconvolve not the original PSF but another intermediate one which makes the final result to fulfill the sampling theorem, Thus it is not possible to recover the original image but one convolved with a narrow PSF of 2 pixel width. In this way spikes and ringing effects so common to traditional deconvolution methods are also avoided.

Although the measurement of morphological and photometric parameters as the flux and the ellipticity was previously undertook in other chapters by means of analytical formulae, a new approach has also been tried to estimate them. In the case of flux, a new expression for it, the so called GaaP aperture flux, is developed in CHEF coefficients. The results show that CHEF functions behave better than the shapelets in measuring this quantity. As for shear, an estimation by least square minimization is implemented, calculating both the ellipticity parameters and the CHEF coefficients applying the Levenberg-Marquardt minimization algorithm. Results are also much more accurate than the ones provided by shapelets with the same method. However, it can be concluded that analytical formulae are more precise than these two approaches, so they are the ones finally used by the CHEF pipeline.

Image simulation has also been tried using CHEF bases. The method, consisting in modeling real sources (from UDF, for instance) and later adjusting them to the special physical characteristics of the observations we want to reproduce (pixel size, PSF convolution, or noise level), has shown to be highly useful to calibrate the observational effects of the instrumentation and test the reliability of some photometric methods.

The fully automated CHEF pipeline is being applied to huge datasets coming from large surveys. By way of illustration, the real application of the algorithm on observations from ALHAMBRA survey is displayed, where data from 20 different optical filters must be processed.

Finally, the CHEFs are also efficient to subtract main objects from galaxy clusters, letting the information under these sources to remain if desired. As galaxies are overlapping in these cases, a new strategy has been implemented, creating a complex large CHEF basis composed by simple ones evaluated on a big grid covering the whole cluster and with different origins, matching each galaxy center. This application has revealed to be crucial for strong lensing studies, since it allows the proper measurement of the lensing arcs under the cD galaxies, avoiding the contamination by the flux from the extended wings of these huge sources. A final example to prove that the CHEFs are not only able of modeling standard galaxies but also lensing arcs has been displayed, in order to show that they can be a very promising tool for measuring the photometry of these objects more accurately.

Bibliography

Abramowitz, M; Stegun, A. (1970). Handbook of mathematical functions: with formulas, graphs, and mathematical tables. Dover publications, 1046pp. New York.

Beckwith, S.V.W. 2004, STScI

Benítez, N. et al. 2009, ApJ, 692, 1, L5

Bennia, A; Riad, S.M. (1990). An optimization technique for iterative frequency-domain deconvolution. IEEE Transactions on Instrumentation and Measurement, 39, 2, 358-362.

Bernstein, G.M; Bebek, C; Rhodes, J; Stoughton, C; Vanderveld, R.A; and Yeh, P. (2009). Noise and bias in square-root compression schemes. The Publications of the Astronomical Society of the Pacific,122, 889, 336-346, arXiv:0910.4571v2.

Bertin, E. (2009). SkyMaker: astronomical image simulations made easy. Memorie della Società Astronomica Italiana, 80, 422.

Bridle, S. et al. (2009). Handbook for the GREAT08 challenge: an image analysis competition for cosmological lensing. Annals of Applied Statistics, 3, 6-37.

Bouwens, R; Broadhurst, T; Silk, J. (1998). Cloning Hubble Deep Fields. I. A model-independent measurement of galaxy evolution. ApJ, 506, 557-578.

Bouwens, R; Broadhurst, T; Silk, J. (1998). Cloning Hubble Deep Fields. II. Models for evolution by bright galaxy image transformation. ApJ, 506, 579-589.

Dobke, B.M; Johnston, D:E; Massey, R; High, F.W; Ferry, M; Rhodes, J; Vanderveld, R.A. (2010). Astronomical image simulation for telescope and survey development. ArXiv:1008.4112v2.

Erben, T; Van Waerbeke, L; Bertin, E; Mellier, Y; Schneider, P. (2001). How accurately can we measure weak gravitational shear?. A&A, 366, 717-735.

Ferry, M; Rhodes, J; Massey, R; White, M; Coe, D; Mobasher, B. (2008). Color, 3D simulated images with shapelets. ArXiv:0807.0475.

Heymans, C. et al. (2006). The Shear Testing Programme - I. Weak lensing analysis of simulated ground-based observations, MNRAS, 368, 1323-1339.

High, F.W; Rhodes, J; Massey, R; and Ellis, R. (2007). Pixelation effects in weak lensing. The Publications of the Astronomical Society of the Pacific, 119, 861, 1295-1307. ArXiv:astro-ph/0703471.

Jelinsky, P. and SNAP Collaboration (2006). The SNAP mission overview. Bulletin of the American Astronomical Society, 38, 1039.

Kuijken, K. (2006). Shears from shapelets. A & A, 456, 827-838.

Kuijken, K. (2008). GaaP: PSF- and aperture-matched photometry using shapelets. A & A, 482, 1053-1067.

Levenberg, K. (1944). A method for the solution of certain non-linear problems in least squares. The quarterly of applied mathematics, 2, 164-168.

Magain, P; Courbin, F; Sohy, S. (1998). Deconvolution with correct sampling. The Astrophysical Journal, 494, 472-477.

Massey, R; Refregier, A; Conselice, C.J; Bacon, D.J. (2004). Image simulation with shapelets, MNRAS, 348, 214-226.

Meneghetti, M; Melchior, P; Grazian, A; De Lucia, G; Dolag, K; Bartelmann, M; Heymans, C; Moscardini, L; Radovich, M. (2008). Realistic simulations of gravitational lensing by galaxy clusters: extracting arc parameters from Mock DUNE images, A&A, 482, 403-418.

Nahman, N.S; Guillaume, M.E. (1981). Deconvolution of time domain waveforms in the presence of noise. NBS Tech. Note 1047, NBS, Boulder, USA.

Postman, M; Coe, D; Ford, H; Riess, A; Zheng, W; Donahue, M; Moustakas, L; and CLASH team. CLASH: Cluster lensing and supernova survey with Hubble. In AAS Meeting #217, #227.06. Bulletin of the American Astronomical Society, 43.

Refregier, A; Amara, A; Kitching, T; Rassat, A; Scaramella, R; and Weller, J. (2010). EIC science book. ArXiv:1001.0061.

Riad, S.M; Stafford, R.B. (1980). Impulse response evaluation using frequency-domain optimal compensation deconvolution. Proc. 23rd Midwest Symposium on Circuits and Systems, Toledo, USA, pp. 521-525.

Riad, S.M. (1986). The deconvolution problem: an overview. Proceedings of he IEEE, 74, 1, 82-85.

Schrabback, T. et al. (2009). Evidence for the accelerated expansion of the Universe from weak lensing tomography with COSMOS. ArXiv:0911.0053.s

Shannon, C.E. (1949). Communication in the presence of noise. Proc. of the IRE, 37, 1, 10-21.

Zitrin, A; Broadhurst, Tom; Umetsu, K; Medezinski, E; Rephaeli, Y; Jiménez-Teja, Y; Benítez, N; Ford, H; Liesenborgs, J; De Rijcke, S; Dejonghe, H; Beckaert, P. (2010). Full Lensing Analysis of Abell 1703: Comparison of Independent Lens-Modelling Techniques. MNRAS, 408, 1916-1927.

6

Conclusions

Motivated by the need to perform accurate galaxy photometry and shape measurements in large surveys like ALHAMBRA or the upcoming JPAS, we have developed a new orthonormal basis in polar coordinates formed by a combination of rational Chebyshev and trigonometric functions for, respectively, the radial and angular components, and that we called CHEF functions, or CHEFs.

The new basis displays remarkable flexibility, being able to accurately fit all kinds of galaxy shapes, including irregulars, spirals, ellipticals, highly compact and highly sheared galaxies. This flexibility is due to its orthogonal character, which makes them able to model any kind of feature, its scale parameter L, which is easily adapted to the resolution of the images, and the wings of CHEFs, which tend to 1 and do not constrain the flux coming from the sources. In this way, the same level of precision is reach for both the central bulge of the galaxies and the extended wings, which is not the case of methods as shapelets, for instance.

In addition, this accurate modeling is performed while using fewer components that similar methods, as shapelets, due to the compactness of the CHEF basis and the great efficiency of Chebyshev rational functions in modeling decaying profiles, specailly those ones displaying a high steepness. Moreover, this efficiency is also responsible for the smoothness of the obtained models, not producing any kind of artifacts, while other standard approaches as shapelets are affected by ringing effects when decomposing too steep or highly elliptical sources.

The method is also lineal, what makes some operations easier in CHEF domain, such as the PSF deconvolution or the calculation of both morphological and photometric parameters just using the CHEF coefficients (for example, the flux, the centroid, the rms radius, and the ellipticity). In the case of the flux and the shear, two different approaches were developed to try to reach the maximum level of accuracy, one of them by means of analytical formulae and another one by least square minimization. Due to the high quality of the fits in the central parts of the galaxies, and the ability of the CHEF basis to compactly model galaxy profiles up to very large distances, the method based on analytical

formulae provides highly accurate estimates of total galaxy fluxes and ellipticities.

CHEF functions have been revealed to be very stable and robust, and, therefore, able to work very fast and to automatically process large numbers of galaxies. For this reason, they have been successfully applied on large datasets from surveys such as ALHAMBRA or the UDF, reaching excellent results without requiring interactivity from the user. In addition, some tasks of the CHEF pipeline have been improved to get an even faster computation time, without decreasing the precision of the final products.

Finally, CHEFs have been shown to be highly useful for gravitational lensing purposes too, and not only for estimating the shear. They have been applied to both simulated to real clusters, such as Abell 1703 or the data provided by CLASH project, to subtract the main galaxies in clusters, then allowing to measuring and analyzing the lensing arcs covered by them or affected by the flux of the extended wings. The CHEF pipeline was slightly modified to adapt it to the overlapping sources in clusters, permitting the modeling of several sources simultaneously by means of a complex CHEF basis composed by simple CHEF functions centered on each one of the overlapping galaxies. Further work will explore the use of CHEF bases to model the projected dark matter distribution.

In addition, arcs from lensing images can be also processed using CHEFs, although they do not display the preferred morphology for this technique, and results look very promising. So applying this method the photometry of lensing arcs will be further developed in a near future.

Future work will explore in more detail many other applications of the method to problems such as the development of a parallel pipeline substituting the orthonormalization method (the slowest step in the algorithm) by the SVD decomposition smartly implemented to be optimal, the search for an analytical and general relation between the optimal scale parameter L and the half light radius r_h to get even better results, or performing a principal component analysis to create a morphological classification scheme for galaxies, just based on the CHEF coefficients.

To finish, we would like to include a list of the papers that have already been or are about to be published, as well as a brief summary of each one:

- Jiménez-Teja, Y., and Benítez, N. CHEF bases: mathematical background, in press. The aim of this paper is exposing the whole mathematical theory where CHEFs rely on, to be published in an applied mathematics journal.

- Jiménez-Teja, Y., and Benítez, N. The CHEF basis: a new tool for image analysis, in press. This paper is focused on describing the practical implementation of CHEFs and the applications developed for Astrophysics.

- Zitrin, A; Broadhurst, Tom; Umetsu, K; Medezinski, E; Rephaeli, Y; Jiménez-Teja, Y; Benítez, N; Ford, H; Liesenborgs, J; De Rijcke, S; Dejonghe, H; Beckaert, P. (2010). Full Lensing Analysis of Abell 1703: Comparison of Independent Lens-Modelling Techniques. MNRAS, 408, 1916-1927.

In this work, CHEFs were applied to real images of Abell 1703 cluster, subtracting the main galaxies to determine the mass distribution in the cluster.

- Coe et al., in press. A new paper applying CHEFs subtraction algorithm on cluster Abell 2744 is currently being prepared.
- CLASH Team, in press. First results from CLASH project will be soon released with the results of the lensing processing of the cluster Abell 383.